Measuring correlated electron dynamics on few femtoseconds time scale

Dissertation
zur Erlangung des Doktorgrades
des Department Physik
der Universität Hamburg

vorgelegt von

Rashmi Singla

aus Haryana, India

Hamburg

July 22, 2015

Gutachter der Dissertation :	Prof. Dr. Andrea Cavalleri
	Prof. Dr. Wilfried Wurth
Gutachter der Disputation :	Prof. Dr. Andrea Cavalleri
	Prof. Dr. Franz X. Kaertner
Datum der Disputation :	July 16th, 2015
Vorsitzender des Promotionsausschusses:	Prof. Dr. Daniela Pfannkuche
Dekan der MIN Fakultät :	Prof. Dr. Heinrich Graener
Leiter des Fachbereich Physik :	Prof. Dr. Peter Hauschildt

काक चेष्टा, बको ध्यानं,
स्वान निद्रा तथैव च
स्वल्पहारी, गृहत्यागी
विद्यार्थी पंच लक्षणं।

I dedicate this work
to my parents

Abstract

The ultrafast on demand control of functional materials is fundamental for high-speed new generation storage and switching devices. Strongly correlated compounds hold an important position along this direction because of the coexistence of various degrees of freedom, which make them delicate towards even minute external perturbations. Femtosecond optical pulses represent an ideal tool to induce ultrafast changes in their macroscopic electronic properties.

In this thesis, we resolved the temporal pathway of the photo-induced phase transitions on time scales comparable or shorter than the characteristic perturbation time, in two prototypical correlated electron materials. Knowledge of the ultimate timescale, on which a transition occurs, is of fundamental interest to understand the mechanisms stabilizing the ground states of these systems. Furthermore, the coherent response of effective interactions on few femtosecond time scales can allow identifying the nonlinear coupling behind vibrational excitations and the electronic correlations.

We investigated the photo-induced melting of orbital ordering in half-filled manganite $La_{0.5}Sr_{1.5}MnO_4$ with ~ 4 fs time resolution and found a temporal bottleneck, corresponding to one-quarter period of the in-plane Jahn-Teller mode (B_{1g} at 14.7 THz). This observation established that the Jahn-Teller effect is the driving force to the stable orbital order, rather than the electronic interactions. We also found coherent oscillations of the structural distortion mode with a threshold to its amplitude in the fluence dependence. These oscillations are triggered by a cooperative lattice-orbital response underscoring the structural pathway taken by photoinduced rearrangement of the orbital order.

In a second experiment, we coherently control many-body interactions in strongly correlated quantum materials. Specifically, we dynamically modulate the electronic on-site correlations in the organic 1D Mott insulator ET-F_2TCNQ. Within the picture of a Hubbard model that represents controlling the onsite repulsion U, along the lines of what is achieved so far only in cold gases through the Feshbach resonance. The phase stable optical excitation of a charge-coupled molecular vibrational mode of the constituting ET-molecule of the organic salt modulates the local charge densities on each site, thus changing the effective Coulomb screening and hence the effective correlation U/t. Probing the frequency resolved charge transfer spectrum on a sub-10 fs timescale allows us to investigate the correlation dynamics during the vibrational excitation with sub-cycle time resolution. We found that exclusively U/t is modulated at a frequency twice the driving field of the coherently driven molecular displacement. This experiment opens a new pathway to dynamically control the correlations in many-body systems, a task so far only possible in cold atoms experiments.

Zusammenfassung

Die gezielte Kontrolle funktionaler Materialien auf ultrakurzen Zeitskalen ist für die Entwicklung zukünftiger Hochgeschwindigkeitsrechner und -speicher unerlässlich. Materialien mit starken elektronischen Korrelationen halten eine wichtige Position in diesem Feld, bedingt durch die Koexistenz verschiedener Freiheitsgrade, welche sie besonders empfindlich gegenüber äußeren Einflüssen machen. In diesem Zusammenhang haben sich Femtosekunden-Laserpulse als ideales Werkzeug für die ultraschnelle Veränderung ihrer makroskopischen elektronischen Eigenschaften herausgestellt.

In der vorliegenden Arbeit wird der Ablauf lichtinduzierter Phasenübergänge in zwei prototypischen korrelierten Elektronensystemen auf Zeitskalen, die vergleichbar oder kürzer als die charakteristische Anregungsdauer sind, untersucht. Die Kenntnis der ultimativen Dauer, die ein Phasenübergang benötigt, wäre von fundamentaler Bedeutung für das Verständnis der Prozesse und Mechanismen, welche den Grundzustand dieser Materialen stabilisieren. Ferner würde die Untersuchung kohärenter Dynamik auf der Zeitskala nur weniger Femtosekunden die Identifikation nichtlinearer Kopplungen zwischen direkt angeregten Schwingungsmoden und elektronischen Wechselwirkungen in korrelierten Systemen ermöglichen.

Wir untersuchten das lichtinduzierte Abschmelzen der orbitalen Ordnung im halb-dotierten Manganit $La_{0.5}Sr_{1.5}MnO_4$ mit einer Zeitauflösung von ca. 4 fs und fanden eine zeitliche Limitierung dieser Dynamik, die einer Viertelperiode des planaren Jahn-Teller Phonons (B_{1g} bei 14.7 THz) entspricht. Diese Beobachtung impliziert, dass der Jahn-Teller Effekt, und nicht die elektronischen Interaktionen, die treibende Kraft zur Stabilisierung der orbitalen Ordnung ist. Wir beobachteten ebenfalls kohärente Schwingungen dieser strukturellen Mode, allerdings nur oberhalb einer Schwelle in der optischen Anregungsdichte. Wir schließen, dass diese Schwingungen durch eine kooperative Antwort der involvierten elektronischen Orbitale und des Kristallgitters auf den Laserpuls getrieben werden und unterstreichen damit die Bedeutung der strukturellen Komponente während der lichtinduzierten Neuordnung der orbitalen Ordnung.

In einem zweiten Experiment studierten wir die Möglichkeit der voll kohärenten Kontrolle von Vielteilchen-Interaktionen in einem stark korrelierten Quantensystem. Dazu modulierten wir im organischen ein-dimensionalen Mott-Isolator ET-F_2TCNQ (einem Molekularkristall) die lokalen elektronischen Korrelationen. Im Bild des Hubbard-Modells entspricht dies einer gezielten Kontrolle der Abstoßung U, was experimentell bisher nur in tiefkalten Gasen durch die Feshbach-Resonanz erreicht werden konnte. Die phasenstabile optische Anregung einer lokalen ladungsträger-gekoppelten Schwingungsmode der ET-Moleküle moduliert

die lokale Elektronendichte, und damit einhergehend die effektive Coulomb Abstoßung sowie die effektive Korrelation U/t. Die spektral aufgelöste optische Abfrage des Ladungstransfer-Bandes auf einer Zeitskala unterhalb von 10 fs ermöglicht die Analyse der Korrelationsdynamik während der Schwingungs-Anregung mit einer Zeitauflösung oberhalb einer Schwingungsperiode. Wir fanden, dass die effektive Korrelation U/t bei der doppelten Frequenz der resonant getriebenen Molekularschwingung moduliert wird. Dieses Experiment ebnet einen neuen Weg zur dynamischen Kontrolle von Korrelationen in kondensierten Vielteilchen-Systemen.

Hiermit erkläre ich an Eides statt, dass ich die vorliegende Dissertationsschrift selbst verfasst und keine anderen als die angegebenen Quellen und Hilfsmittel benutzt habe. Diese Arbeit lag noch keiner anderen Person oder Prüfungsbehörde im Rahmen einer Prüfung vor.

I hereby declare, on oath, that I have written the present dissertation on my own and have not used other than the mentioned resources and aids. This work has never been presented to other persons or evaluation panels in the context of an examination.

Rashmi Singla
Hamburg, 2015

Signed:

Date:

Role of Author

The optical birefringence measurements reported in chapter 4 were performed by the author together with A. Simoncig. The characterization of the ultrashort laser pulses was provided by Ivanka Grguras. The analysis of the data was done by the author under the guidance of M. Foerst, A.L. Cavalieri and A. Cavalleri.

The measurements and analysis of the experimental data reported in chapter 6 were performed exclusively by the author. The broadband NIR setup used was built by C. Manzoni and slightly modified by the author. The mid-infrared setup was build by M. Foerst and was used for the experiment by the author. The phase stablization technique in time domain was set up by L. Piovani and the author. The many body simulations were performed by G. Cotugno together with S. Clark and D. Jaksch at Oxford University.

The pressure dependent time resolved pump-probe measurements reported in section 5.5 were performed by the author together with M. Mitrano.

The author thanks the University of Hamburg, Max-Planck Institute for the Structure and Dynamics of Matter and Center for Free Electron Laser, Hamburg for funding the the work presented in this thesis.

List of Publications

- Correlation-gap oscillations in an organic Mott-insulator induced by phase locked excitation of local molecular vibrations
  R. Singla, S. Kaiser, G. Cotugno, S.R. Clark, C. Manzoni, A. Cartella, H. Liu, M. Foerst, T.Hasegawa, H. Okamoto, D. Jaksch and A. Cavalleri
  http://arxiv.org/abs/1409.1088

- Pressure-Dependent Relaxation in the Photoexcited Mott Insulator ET–F_2TCNQ: Influence of Hopping and Correlations on Quasiparticle Recombination Rates
  M. Mitrano, G. Cotugno, S. R. Clark, R. Singla, S. Kaiser, J. Stähler, R. Beyer, M. Dressel, L. Baldassarre, D. Nicoletti, A. Perucchi, T. Hasegawa, H. Okamoto, D. Jaksch and A. Cavalleri
  Phys. Rev. Lett. 112, 117801 (2014)

- Photoinduced melting of the orbital order in $La_{0.5}Sr_{1.5}MnO_4$ measured with 4-fs laser pulses
  R. Singla, A. Simoncig, M. Foerst, D. Prabhakaran, A. L. Cavalieri and A. Cavalleri
  Phys. Rev. B 88, 075107 (2013)

- Photoinduced melting of magnetic order in the correlated electron insulator $NdNiO_3$.
  A. D. Caviglia, M. Foerst, R. Scherwitzl, V. Khanna, H. Bromberger, R. Mankowsky, R. Singla, Y.-D. Chuang, W. S. Lee, O. Krupin, W. F. Schlotter, J. J. Turner, G. L. Dakovski, M. P. Minitti, J. Robinson, V. Scagnoli, S. B.Wilkins, S. A. Cavill, M. Gibert, S. Gariglio, P. Zubko, J.-M. Triscone, J. P. Hill, S. S. Dhesi, and A. Cavalleri
  Phys. Rev. B 88, 220401(R) (2013)

- Ultrafast strain engineering in complex oxide heterostructures.
  A. D. Caviglia, R. Scherwitzl, P. Popovich, W. Hu, H. Bromberger, R. Singla, M. Mitrano, M.C. Hoffmann, S. Kaiser, P. Zubko, S. Gariglio, J.-M. Triscone, M. Foerst, and A. Cavalleri
  Phys. Rev. Lett. 108, 136801 (2012)

Contents

1 Introduction 1

2 Dynamics of effective electronic interactions 5
- 2.1 Non-correlated systems 5
- 2.2 Dynamics of non-correlated systems 7
- 2.3 Correlated systems 8
  - 2.3.1 Hubbard model 10
  - 2.3.2 Dynamical Hubbard Model 14
- 2.4 Dynamics of correlated electronic systems 16
  - 2.4.1 Dynamics on fundamental time scales 20

3 Manganites and their physical properties 25
- 3.1 Structural and electronic properties 25
- 3.2 Magnetic properties 30
  - 3.2.1 Superexchange interaction: 31
  - 3.2.2 Double exchange interaction 31
  - 3.2.3 Goodenough-Kanamori-Anderson rules 33
- 3.3 Orbital physics of manganites 33

4 Ultrafast melting of orbital ordering in $La_{0.5}Sr_{1.5}MnO_4$ 35
- 4.1 Manganite $La_{0.5}Sr_{1.5}MnO_4$ 35
  - 4.1.1 Charge and orbital ordering in $La_{0.5}Sr_{1.5}MnO_4$ 35
  - 4.1.2 Factors responsible for orbital ordering 36
  - 4.1.3 Optical birefringence of orbital ordering 38
- 4.2 Ultrafast observation for melting of orbital order 38
- 4.3 Generation of 4 fs laser pulses in the visible/NIR 41
- 4.4 Pump-probe setup 44
- 4.5 Structural bottleneck for melting of orbital order 45
- 4.6 Summary 51

5 One dimensional correlated systems 53
5.1 The physics of 1D Mott insulators 53
5.2 ET-F_2TCNQ, a prototypical 1D system 55
  5.2.1 Crystal structure 55
  5.2.2 Optical properties 57
  5.2.3 Fit to the steady state optical conductivity 59
5.3 Optical excitonic states in a 1D Mott insulator 61
5.4 Photo-excitation of the Mott gap 63
5.5 Control of interaction parameters in ET-F_2TCNQ 66
  5.5.1 Role of pressure dependent V and t in quasiparticle dynamics . . 69
  5.5.2 Control of effective correlation U/t by selective mode excitation . 73
5.6 Summary 78

6 Dynamic control of electronic correlations in a solid state Mott insulator 81
6.1 Dynamic control of Hubbard U 81
6.2 Nearly transform limited NIR pulse generation 83
6.3 Phase stable MIR pulse generation 89
  6.3.1 Carrier envelope phase stablization 91
6.4 Non-degenerate pump-probe setup 92
6.5 Photo-vibrated changes in the charge transfer band 94
6.6 Spectrally resolved photo-excited dynamics 98
  6.6.1 Fitting of Mott gap 101
6.7 Simulations 106
6.8 Summary 111

7 Conclusions and outlook 113
7.1 Conclusions 113
  7.1.1 Orbital dynamics in Manganites 113
  7.1.2 Dynamics of 1D Mott insulator 114
7.2 Outlook 114

Appendix A: Ultrashort laser pulses generation 117
A.1 Optical parametric amplification 118
  A.1.1 Second order optical non-linearity 118
  A.1.2 Parametric Amplification 119
  A.1.3 Condition for broadband parametric amplification 123
A.2 Self-phase modulation and white light generation 123
A.3 Pump-probe spectroscopy 127

Appendix B: Alternate pathway to modulation of Mott gap in a 1D half-filled Mott insulator 129

Appendix C: Perturbed free induction decay 131

Acknowledgement 151

1 Introduction

Strongly correlated electron systems are solids in which our common understanding of weakly-coupled charge carriers fail. Unlike, semiconductors and metals, these systems exhibit electron-electron Coulomb repulsion energies on the scale of a few eV, orders of magnitude higher than the thermal energy scale, and a dominant contribution to the internal energy of the system. This Coulomb repulsion 'U' induces the localization of charges that is in competition with their itinerancy, often described by the hopping constant 't'. Generally, it is the ratio 'U/t' that determines the insulating or the conducting electronic ground state in correlated systems [1].

In combination with structural degrees of freedom, the electronic correlations lead to a wealth of quasi-degenerate ground states that are weakly separated from each other by rather flat barriers in the free energy landscape. The collective behavior of the electronic ensemble, for example, force the existence of a variety of emergent phenomena [2, 3] like high-T_c superconductivity, colossal magnetoresistivity and antiferromagnetism [3–5]. Most importantly, the different phases of the correlated systems transform into another under even subtle external perturbations of temperature, pressure and doping. As a result, understanding the behaviour of these materials on the brink of transitioning is crucial for controlling and engineering their responses.

Out-of-equilibrium studies of phase transitions with femtosecond light pulses are of special interest, in the view of achieving ultrafast manipulation of electronic properties and on demand. One of the technical applications is to find a bidirectional switch which can be controlled on ultrafast time scale by lasers. This could speed up the computational speed by several orders of magnitude than the present electronics, where the later relies on the gating of the current controlled by electric voltage.

Typically, the phase transitions involve a persistent change in symmetry induced impulsively by a laser pulse that lasts only for a few femtoseconds [6]. As shown in figure 1.1, optical pumping can initiate the dynamics from the ground state A to a final state D, going through various transient metastable states B and C [7]. These kinds of photoinduced phase transitions can be approached through two different mechanisms. The first process involves direct photo-excitation of the electronic degrees of freedom at few eV energies using visible and near-infrared light described as 'photodoping'. It increases the electronic temperatures such that at a certain critical temperature T_c, the system makes a crossover from a broken symmetry state present at low temperature to a different symmetry state [8–11]. The second is the excitation of low-energy collective modes like phonons, requiring meV photon energies in the mid-infrared spectral range and transiently change the structural arrangement of the atoms. It does not involve any direct heating presumably because it lies below the energy of electronic excited states, resonant to vibrational excitations [12–15]. In the special case of correlated molecular solids, comprised of periodically spaced molecules weakly bound by weak van-der-Walls forces, an additional degree of freedom of the local molecular vibrations can be resonantly excited. This allows to access and control local properties like the on-site molecular orbital wavefunction which defines the local effective correlation interactions [16–20].

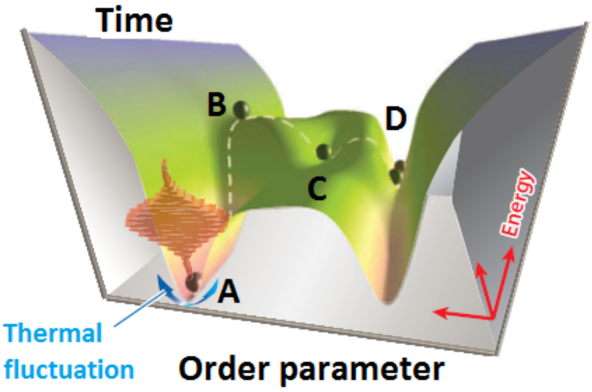

Figure 1.1: Photoinduced pathway of order parameter across energy landscape as a function of time after stimuli [Adapted from [7].]

Time-resolved optical spectroscopy allows us to identify transient characteristics of the phases, thereby helping to understand and control the ultrafast phase transitions. Here, a strong pulse with high electric field drives the system into the non-linear regime and a time delayed weak pulse interrogates the dynamically modulated state. The prime questions to be addressed are on the speed of these phase transitions and on the temporal evolution of the involved phase state.

The time-resolved optical spectroscopy is particularly powerful if the probe photon energy is resonant with the electronic interaction energy (say 'E') of the system investigated. Additionally, to be able to observe the changes in the interactions on their inherent time scale, the electric field of these pulses should have as few as possible number of cycles corresponding to the emergent time scale of interactions ($t \geq \frac{\hbar}{2E}$, Heisenberg uncertainty principle). For example, fast time scales of the order of attoseconds are now-a-days routinely achieved in extreme ultraviolet (XUV) regime. But this part of spectrum is very high in energy and usually is used to study the charge transfer processes inside the atom or molecule. In our case, we are interested in extreme time scales in the infrared region to probe the electronic interactions in complex solids.

The present thesis deals with revealing the ultrafast dynamics of two correlated systems at the fundamental time scale of the relevant energy investigated:

The first system is the half-filled charge-transfer insulating manganite $La_{0.5}Sr_{1.5}MnO_4$, well known for its charge/orbital ordering (CO/OO) [21, 22]. We determine the ultimate time scale for photo-induced melting of orbital order in this compound by measuring the time-dependent optical birefringence with near-visible 4-femtosecond pulses. Such high time resolution is required to distinguish the role of atomic motions that stabilize the orbital ordering via the Jahn-Teller distortion from even faster electronic rearrangements.

The second experiment investigates the modulation of electronic correlations induced by the excitation of vibrational molecular modes in the one-dimensional molecular solid ET-F_2TCNQ, a room temperature Mott insulator with high U/t. The local mode of the ET molecule is coherently driven using with carrier envelope phase stable pulses, thus deforming the local orbital wave functions and modulating the local charge densities at each site. The resultant change in electronic screening is expected to modulate the effective on-site correlation U/t. We interrogate this issue by probing the optical gap using 10-femtosecond near-infrared pulses resonant with the charge transfer resonance. As such, the quadratic coupling between the electronic correlations and the coherently driven molecular mode is captured with unprecedented sub-cycle temporal resolution.

2 Dynamics of effective electronic interactions

2.1 Non-correlated systems

A very successful way of describing the properties of many solid-state systems arose with the introduction of "band picture" that explains the properties of metals, semiconductors and insulators. This quantum picture is based on 'free electron theory', where an electron is treated free of interaction with other electrons and with atomic ions inside the lattice owing to large screening. Their energy distribution is a continuous function of the wave vector k given by $E{=}(\hbar k)^2/2m$ as shown in figure 2.1(a). This naive picture however could not explain insulating or semiconducting behaviour. Soon after, 'Nearly free electron theory' followed. Here electrons are not treated as free particles but indeed interaction of the plane wave of the electron with the ionic crystals is taken into account. The reflection of electron waves with periodic ionic potential wells give rise to few forbidden energy states in the energy dispersion relation. These

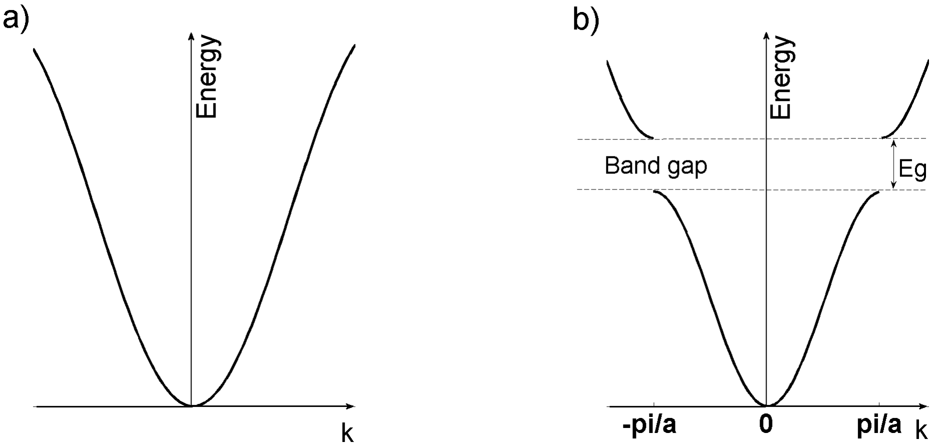

Figure 2.1: Energy vs. wavevector k of an electron in (a) free electron theory (b) nearly free electron theory. E_g is the band gap energy and a is the lattice periodicity

Bragg reflections consequently open a band gap in the band structure of the crystal at zone boundaries as shown in figure 2.1(b) [23].

The energy bands are formed when atoms are very close in a crystal. One way to formulate the band structure of the non-correlated systems is the so-called tight-binding approximation [24]. In the ground state, electrons occupy the lower lying energy band called valence band (and conduction band is the unoccupied higher lying band). At zero temperature, the highest energy level upto which electrons are filled is defined as Fermi energy E_F (see figure 2.2). For metals, the Fermi energy lies within the bands as shown in figure 2.2. On applying electric field, the free electrons in the partially filled conduction band can be accelerated into higher unoccupied quasi-momentum states constituting the electric current. On the other hand, when the Fermi energy lies between the bands separated by E_g, there are no free electrons in the conduction band to mediate current. These materials are termed band insulators. If the band gap energy is of the order of few eV, it is possible to thermally excite some electrons from the valence to the conduction band, where they can respond to the external electric field. Such materials are termed as semiconductors. The conductivity of semiconductors can also be engineered by adding impurities, thereby creating new energy levels in the band gap [23, 25]. The junction created out of a hole doped and electron doped semiconductors have revolutionized the field of electronics and very recently, has lead to a Nobel prize winning discovery of efficient blue diodes [26]. Also, artificially created interfaces in a transistor are intensively used in the electronic circuits like in smartphones or laptops.

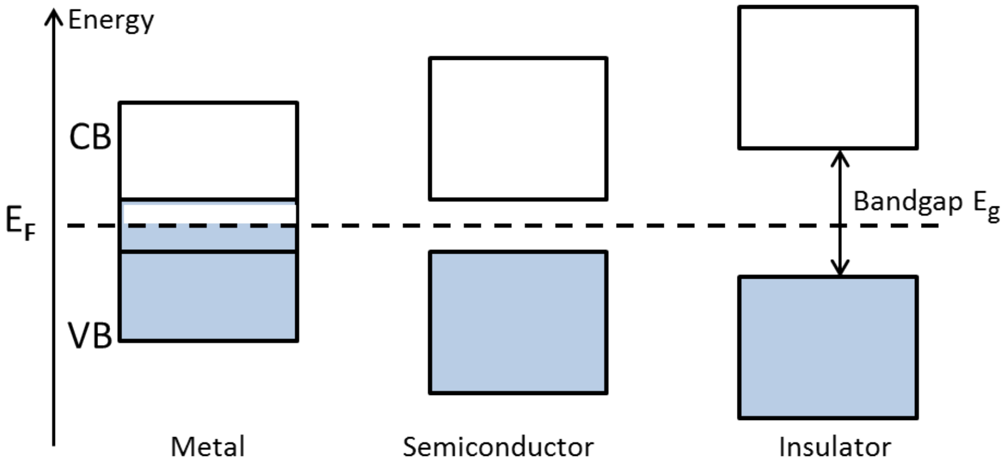

Figure 2.2: Band structure for metal, semiconductor and insulator. Shaded blue box represents the occupied valence band (VB) and upper white box as unoccupied conduction band (CB)

2.2 Dynamics of non-correlated systems

To understand the properties of the materials, the study of their interaction with light is a great tool. Out-of-equilibrium optical excitation and their subsequent relaxation phenomena provides information on the formation of various phases. Unlike perturbations from pressure, temperature, dc-electric fields, magnetic fields or chemical doping, photoexcitation put the system non-adiabatically into the non-equilibrium state comprised of exciton (electron and hole) formation.

The dynamical studies of the materials are made using two laser pulses. The first intense laser pulse initiates the non-equilibrium dynamics. The second weak laser pulse captures the subsequent changes in the system at various times relative to the first pulse. Primarly, three time-resolved spectroscopic techniques are being applied to study the evolution of light induced changes in the structural and electronic degree of freedoms. (1) Time-resolved X-ray spectroscopy, brings direct insight into the structural advancement [27, 28]. (2) The time and angle resolved photoemission spectroscopy (Time-resolved ARPES) provides information on electronic band structure at several values of k. (3) Time-resoved optical spectroscopy focuses on the response of the system at the electronic wave vector $k = 0$.

Optical excitation above a band gap heats the electronic system which then relaxes into a ground state or new state protected by an energy barrier. The pathway taken by the excited carriers while relaxing back to the ground state is of great interest. The photo-excitation of the electrons across the bands (from valence to conduction) cause changes in the occupation density of the bands and shift the E_F as shown in figure 2.3.

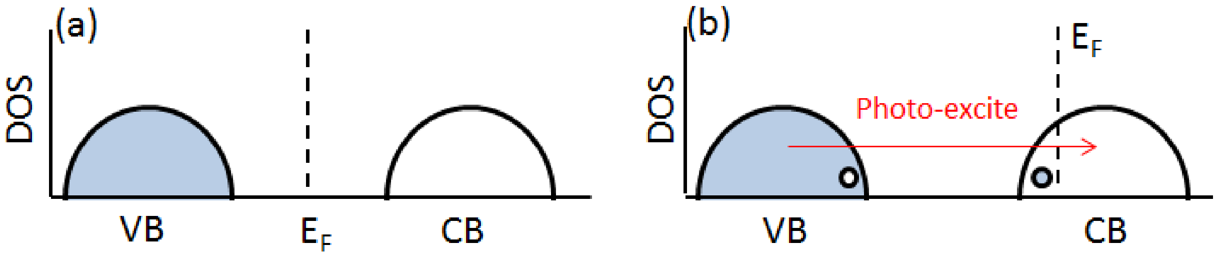

Figure 2.3: Density of state for a band insulator in (a) equilibrium (b) under photo-excitation, creating a hole (hollow circle) and an electron (filled circle) in valence band (VB) and conduction band (CB) respectively. The shaded region represents occupied states and E_F is Fermi energy.

The non-equilibrium dynamics in non-correlated systems have been under study for over four decades. The optical excitation studies in band metals are focused on the modification of electronic and lattice temperatures, efficiently captured by the so-called two-temperature model [29, 30]. The central idea of this model is that under the external perturbation, the electronic and lattice subsystems are connected to each other only by the electron-phonon coupling in line with Born-Oppenheimer approximation [31]. The electrons at an initial temperature of T_e ($= T_{initial}= T_{lattice}$) are driven to an elevated temperature T'_e ($> T_{initial}$) by the absorption of the pump pulse. These 'hot electrons' then relax to quasi-equilibrium states via the exchange of energy with lattice thereby increasing the lattice temperature to $T'_{lattice}$ such that $T''_e = T'_{lattice} > T_{initial}$. The relaxation time of the hot carriers depends inversely on the hopping amplitude of the electron *i.e.* $\tau \propto t$ [25, 29].

Unlike the case of metals, in semiconductors, optical excitation creates a hole in the valence band and an electron in the conduction band, thereby changing the carrier densities in the individual bands. The recombination of the optically created electron-hole pair can occur either through emission of a photon (radiative recombination) or through energy transfer to the lattice bath or to the electrons/hole (nonradiative recombination) [32, 33]. For the case of one-dimensional semiconductor, it can be shown that radiative relaxation time is directly proportional to hopping amplitude *i.e.* $\tau_{rad} \propto t$ [34, 35] and nonradiative relaxation time $\tau_{non-rad} \propto t^2$ [35]. Time-resolved optical experiments focus on the details about these relaxation processes and other coherence effect [33, 36]. Another point to note here is that the rigid band structure (ignoring the case involving spin-orbit coupling) dictates not only the static but also the dynamical properties of these non-correlated systems. The change in carrier densities on photo-excitation do not distort the band structure as it is a function of the atomic arrangement of the crystal.

We will see in next sections that in the case of correlated system, the band picture is insufficient to explain the static properties and also the changes in density of state observed after photo-excitation. Their relaxation dynamics is very different and rich owing to the fact that electrons interact strongly with each other and with the lattice in contrast to that of the non-correlated systems. Despite all these facts, studies on the dynamics of the correlated systems have tremendously benefited from a deep understanding of the non-correlated materials.

2.3 Correlated systems

Wigner was among the first ones to point out the significance of the repulsive Coulomb interactions between the electrons [37]. In 1937, J.H. de Boer and E. J. W. Verwey found that some transition metal oxides (TMO) like NiO, FeO etc. are insulators, while according to the band theory of solids, they were expected to be conductors [38]. NiO with partially filled *d*-orbital shows large energy gap of 4.3 eV. Soon after, N. F. Mott and R. Peierls proposed that the cause for this unconventional gap behavior is the electron-electron Coulomb interaction, which is not considered in conventional band theory [1].

N. F. Mott, in 1949 proposed a model on NiO explaining the observed gapped state [39]. In this view, the on-site repulsive Coulomb interaction energy (U) between electrons in 3*d* orbital of Ni competes with hopping integral (t). An energy of U - t is required to have double electron occupancy in the otherwise half-filled system (see figure 2.4). This puts a limitation on electrons for their movement and hence for conduction too. Materials for which U $\gg$ t are insulators and are termed as 'Mott insulators'. The mathematical description of corresponding Mott physics is given by Hubbard as described in the next section.

Such a Mott state is realized when the nearest neighbor atomic spacing is increased to an extend that the hopping integral 't' is reduced such that the on-site interaction becomes greater to the hopping *i.e.* U $\gg$ t; electrons hence do not have enough energy to hop to the next site and are localized. An energy gap opens in the band structure owing to correlations and electrons are consequently localized.

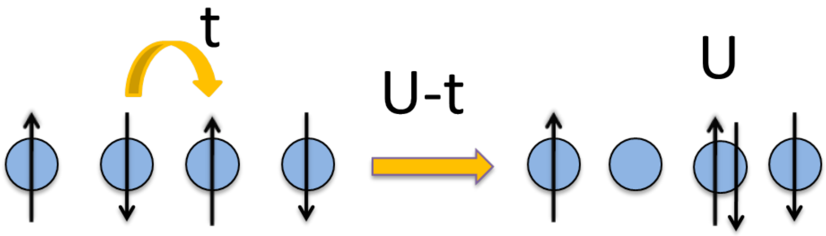

Figure 2.4: A schematic diagram illustrating the transfer of electron from one site to neighbouring site correlated materials, costing energy of U-t. t is the hoping term and U is the on-site electronic coulomb interaction energy.

Correlation effects are believed to be the origin of many exotic electronic properties of transition metal oxides and other organic compounds [40–43]. The correlated electrons also interact with the lattice. These together give rise to more ground states possessing long range orderings of orbitals, charges, lattice and spins. If these degrees of freedom lie close to each other in energy scale, their interplay determines the macroscopic functional properties. Some of the interesting emergent phenomena are for example high-T_c superconductivity, magnetic ordering and insulator-metal (I-M) transition [44].

These emergent phenomena occur on their characteristic energy, length and time

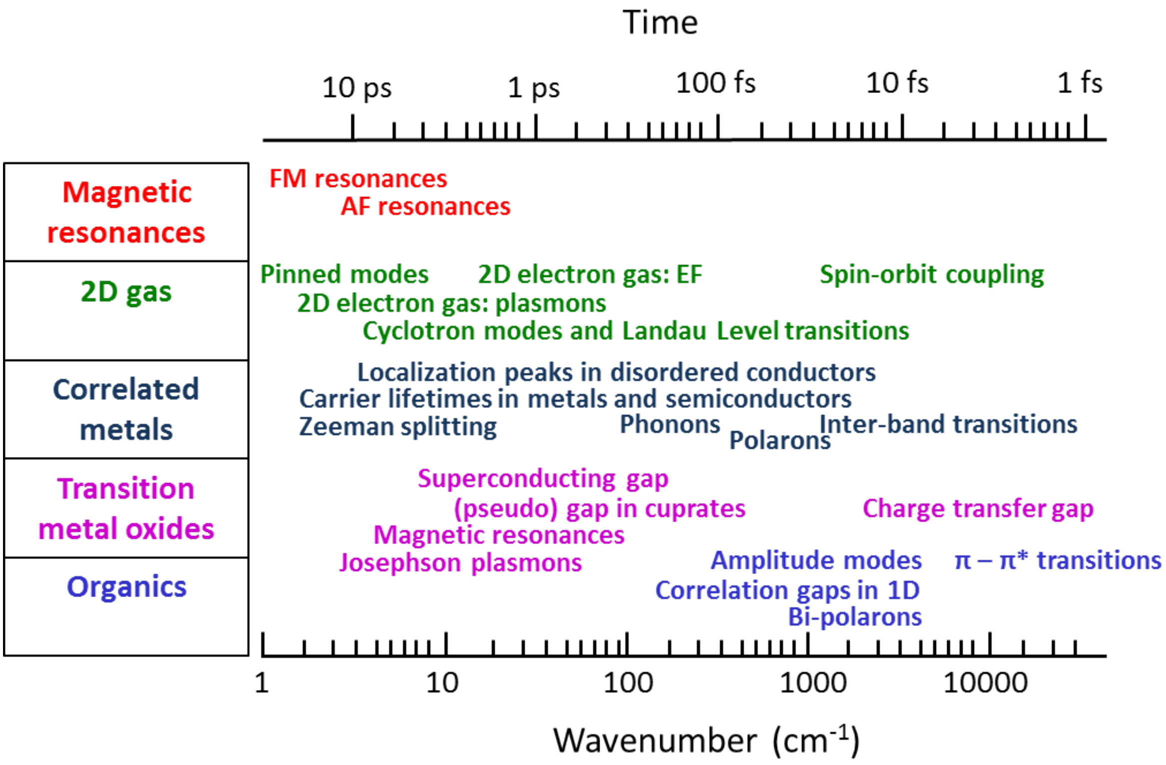

Figure 2.5: A schematic diagram illustrating the energy and time scale of the phenomena happening in correlated electronic systems [Adapted from [45]].

scales. Few of them are listed in figure 2.5 together with their emergent time and energy scale. More recently, strong electronic interaction is revealed not just by transition metal oxides but by a variety of d and f electron compounds as well as π electron organics. Furthmore, progress in the synthesis method of complex oxides and organic materials have made possible the study of their properties in film and also their interfacial physics. Low-dimensional solids are another topic of interest as the dimensionality constrain the motion of electrons and introduce more correlations. By reducing the dimensionality from 3D to 2D to 1D, the correlations get more and more dominant. Low dimensional solids are known to be more prone to collective behavior like that found in spin and charge ordering and even in unconventional superconductors [46].

2.3.1 Hubbard model

Most of the essential features of correlated electronic materials can be described by the Hubbard model. Hubbard gave a mathematical formulation to the conceptual understanding of correlated systems put forward by Mott. The Hubbard-Mott Hamiltonian given below quantitatively explains the physics of the correlated systems considering the electron-electron interaction [47].

$$H = -t \sum_{<ij>,\sigma} \hat{c}^{\dagger}_{i,\sigma}\hat{c}_{j,\sigma} + U\sum_{j} \hat{n}_{j,\uparrow}\hat{n}_{j,\downarrow} \tag{2.1}$$

Here t is the hopping integral, U is the on-site repulsive Coulomb energy, $\hat{c}^{\dagger}_{i,\sigma}$ ($\hat{c}_{i,\sigma}$) is the creation (annihilation) operator for an electron at site i with spin σ and $\hat{n}_{j,\sigma}$ is the electron number operator.

The first term of equation (2.1) determines the hopping probability of an electron to hop from a site i to the nearest neighbor lattice site j.'t' is the transfer integral and depends on the distance between the sites and on the orbital occupancy of the electron. The second term is the Coulomb repulsion between the electrons of ↑ spin and ↓ spin at a single lattice site i. Whereas the first term favors the delocalization of electrons, the second term favors the localization and competes with the first. U/t is a straightforward estimate of the strength of the electronic correlations.

To understand the effect of correlations on the density of states (DOS) and optical conductivity, both are shown in figure 2.6 as a function of energy for the Hubbard model in infinite dimension. When U/W = 0, there is single band half-filled up to the Fermi energy (E_F). W is defined as the bandwidth of a non-interacting electronic system, and $W=2zt$, where z is the number of nearest neighbours and 't' is hopping term. The optical response allows to examine the associated elementary/collective mode and the excitation in condensed matter [43, 49]. In the present case of U/W $\sim$ 0, the carriers in the half-filled band near E_F require negligible energy to move in the half-empty band. In optical spectroscopic measurements, this appears as an absorption band at zero frequency termed as Drude peak (right panel of figure 2.6). With increase in correlations (U/W = 0.5 and 1), the DOS starts to reshape, forming new bands away from the Fermi point. The corresponding optical conductivity shows a shift in spectral weight away from Drude. In the limit of strong correlation (U/W = 2) in infinite dimension, the DOS splits completely into two bands: the filled lower Hubbard band (LHB) and empty upper Hubbard band (UHB). A gap $\Delta \simeq$ U -W opens at E_F. In the optical conductivity, this appears as a band at U with bandwidth 2W, owing to excitation from the LHB to the UHB. The conductivity spectrum for correlated compounds can include other features too, like that of superconductivity, charge density waves (CDW) etc. not discussed here. The DOS can be directly measured experimentally by photoemission spectroscopy [50]. Importantly, this Hubbard band picture is different from the earlier band picture introduced for non-correlated systems because the bands are not 'rigid' *i.e.* the structure of the band renormalizes on filling.

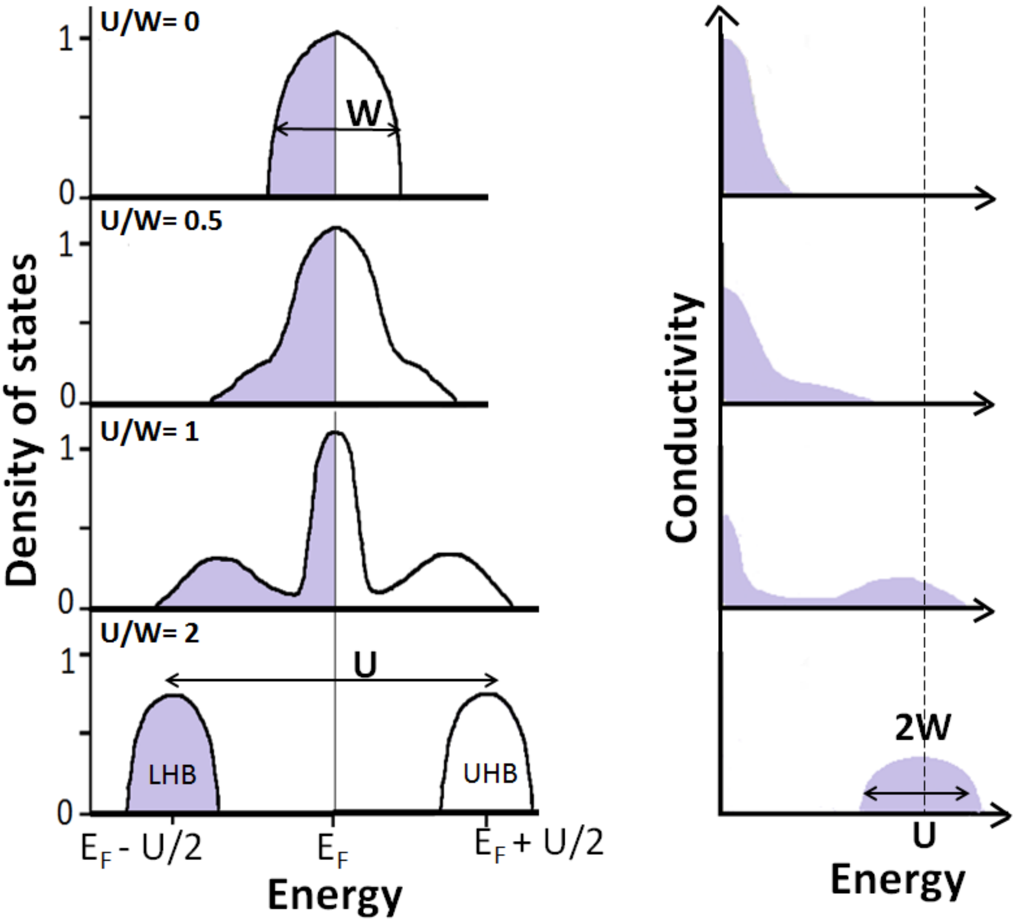

Figure 2.6: (Left panel) Schematic diagram illustrating density of states of electron at half filling and zero temperature for various values of effective coulomb interaction (U/W) as proposed by Hubbard model [Adapted from [48]]. (Right panel) The corresponding optical conductivity response as function of energy. U is the on-site coulomb interaction energy and W is the bandwidth of non-interacting electronic system. LHB and UHB stands for Lower Hubbard Band and Upper Hubbard Band.

However, in some correlated materials, the absorption band in the conductivity spectrum occurs at much lower energy than U. Like in the case of some transition metal oxides where the 2p orbital of oxygen anion is above the LHB of the transition metal (see figure 2.7 (b)). The electron transfers from the anion to the neighbouring cation requires energy $\Delta < U$ [51]. These systems are referred to as charge transfer insulator. Figure 2.7 shows the band structure comparing Mott insulator ($U > \Delta$) and charge transfer insulator ($U < \Delta$) [51]. Both the transitions are possible as in the case of an organic Mott insulator ET-F_2TCNQ. The charge transfer occurs between ET and F_2TCNQ and the Mott transition occurs between neighbouring ET molecules, though here the

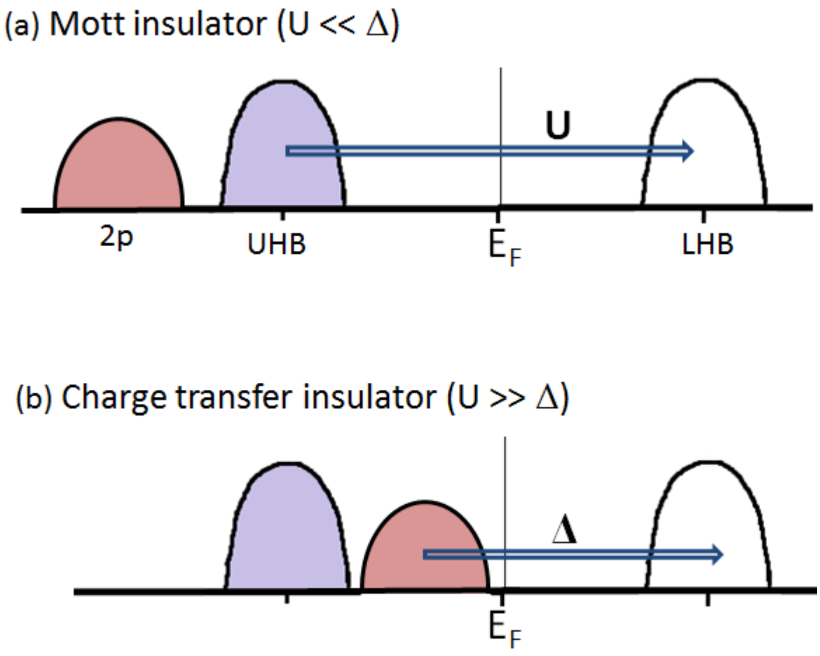

Figure 2.7: Band diagram of a transition metal oxide, consisting of split d-orbital of transition metal into LHB and UHB and filled 2p orbital of oxygen anion. If U $<$ Δ, the compound is Mott insulator. If U $>$ Δ, the transfer of charge occurs from 2p oxygen site to UHB of neighbouring transition metal side and compound is termed as charge transfer insulator.

later is often referred as charge transfer resonance by the scientific community.

Extended Hubbard Model

In the case where the effective screening between neighboring lattice sites is small, the inter-site Coulomb interaction energy (V) starts to play a crucial role [52, 53]. The 'Extended Hubbard Model' incorporates the contribution coming from the nearest neighbour Coulomb repulsion interaction (V) and is given as:

$$H = -t \sum_{<ij>,\sigma} \hat{c}^{\dagger}_{i,\sigma}\hat{c}_{j,\sigma} + U\sum_{j} \hat{n}_{j,\uparrow}\hat{n}_{j,\downarrow} + V\sum_{i,j} \hat{n}_i\hat{n}_j \tag{2.2}$$

where $\hat{n}_j = \hat{n}_{j\uparrow} + \hat{n}_{j\downarrow}$. The model is essential to capture the many-body physics of half-filled and quater-filled systems [54]. We will see in the later sections how this model can be applied to the prototypical organic salt ET-F_2TCNQ where V is necessary to understand the quantum interference between optically induced bound and ionized holon-doublon pairs.

2.3.2 Dynamical Hubbard Model

The Hubbard model does not consider the influence of electronic density on the orbital wavefunction. To understand the importance of this consideration, the on-site repulsion U between electrons of opposite spin on the atomic orbital is calculated and is shown to be very different from the experiment. This is due to expansion of atomic orbital to reduce the repulsive Coulomb interaction between electrons.

For the case of two electrons in 1s orbital of hydrogen, U can be written by:

$$U(z) = \int |\phi_{1s}(r)|^2 \frac{e^2}{|r - r'|} |\phi_{1s}(r')|^2 d^3r d^3r' = \frac{5}{4} z * 13.6eV \tag{2.3}$$

where

$$\phi_{1s}(r) = (\frac{z^3}{\pi a_0^3})^{1/2} e^{-zr/a_0}$$

z is the charge of nucleus, a_0 is the Bohr radius.

However, experimentally obtained effective U is less than bare U [55]. Approximately, for 1s atomic orbitals, for large range of z,

$$U_{eff}(z) = U(z) - 4.1eV \tag{2.4}$$

Similar is the case for other atomic orbitals. The reduction is due to expansion of the orbital thereby expelling the electrons outward to reduce the Coulomb repulsion between electrons. This is a well known effect in atomic physics. It is expected that electrons will angularly correlate themselves on the atom to minimise their Coulomb repulsion and represented by Slater's rules [56]. While the conventional Hubbard model ignores this fact, the dynamical Hubbard model (DHM) accounts for the change in atomic orbital wavefunction under electronic double occupancy [57, 58]. DHM incorporates the asymmetry between the electrons and the holes [59], which quantitatively increases with a decrease in the charge of nucleus.

As shown in figure 2.8 (b), when two electrons with opposite spins are added at a single site, the atomic orbital radius 'r' increases, considered by DHM (in contrast to HM in figure 2.8 (a)). The associated kinetic energy of the electrons given by $\hbar^2/(2m_e r^2)$ is decreased, where m_e is the electron mass. Also the states here are driven by kinetic energy instead of potential energy and electronic correlations considered in HM. Another consequence of the increase in 'r' is that the repulsive Coulomb interaction between electrons are shielded and reduced as depicted by a Slater determinant

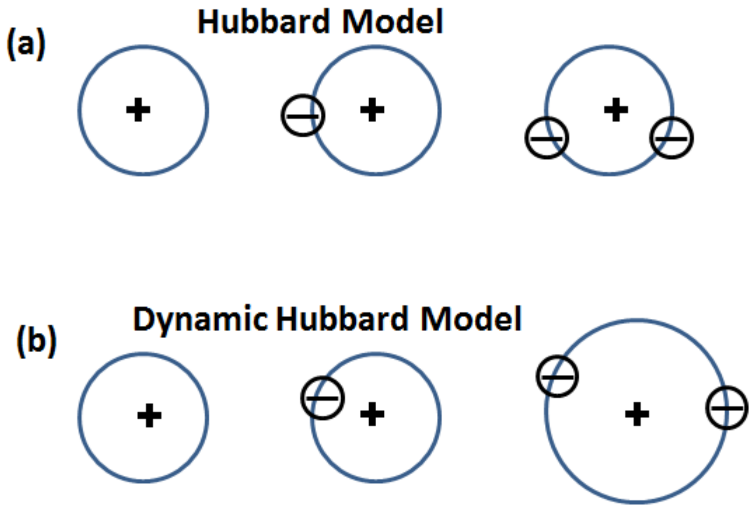

Figure 2.8: Schematic diagram comparing usual 'Hubbard Model' with 'Dynamical Hubbard Model', where the later considers the reshaping (enlargement) of electronic orbital for the case of double occupancy of electron at a lattice site [Adapted from [58]].

for singly occupied orbital. The renormalized Hubbard U considering this physics can be modelled by

$$U(q_i) = U + \alpha q_i \tag{2.5}$$

where q_i is the pseudo-displacement coordinate for atom i and α is the coupling constant. For empty or singly occupied orbital, q_i = 0 and turns to some negative value for double occupancy to account for the resultant reduction in U.
The microscopic Hamiltonian describing the physics of atom i is given by

$$H_i = \frac{{p_i}^2}{2M} + \frac{1}{2}K{q_i}^2 + (U + \alpha q_i)n_{i\uparrow}n_{i\downarrow} \tag{2.6}$$

Here, K = M ω_0^2 (ω_0 is the frequency of the oscillator) and U is reduced to U_{eff} = U - α^2 / (2K).

The effects on Hubbard U corresponding to wavefunction modification were recently observed in the charge transfer band by broadband optical spectroscopy [18]. The DHM is of interest for this thesis and can be particularly appreciated in the experiment reported in chapter 6. A molecular mode of an organic Mott insulator ET-F_2TCNQ is excited and the dynamics of CT resonance (same as the Mott gap) is measured. The experimental finding show appearance of some additional bands in the Mott gap. The pump-induced modulation of molecular mode involves oscillations of the on-site molecular orbital. To consider this effect, one need a model which considers the influence of orbital wavefunction on the on-site interaction U and the experimental finding could be well simulated using a form of DHM (*i.e.* vibrational DHM).

Notably, the dynamical Hubbard model is different from the ordinary Holstein model given by [60]

$$H_i = \frac{p_i{}^2}{2M} + \frac{1}{2}Kq_i{}^2 + Un_{i\uparrow}n_{i\downarrow} + \alpha q_i(n_{i\uparrow} + n_{i\downarrow}) \tag{2.7}$$

The Holstein model dresses single particle occupancy *i.e.* it dresses both the single and double occupied electronic orbital states. Whereas, the DHM considers only the dressing of the later.

Hirsch et al. claim that the undressing mechanism to be an important ingredient towards superconducting transition in high-T_c superconductors [61]. DHM is also suitable to explain charge inhomogeneities found in many transition metal oxides commonly at nanometer scale [62].

2.4 Dynamics of correlated electronic systems

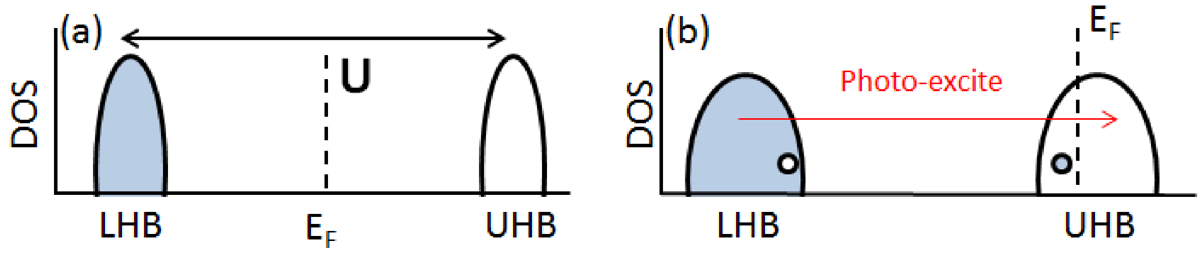

Figure 2.9: DOS for a correlated system of Mott insulator of correlation energy U in (a) equilibrium (b) under photo-excitation, creating a hole and a electron in LHB and UHB respectively

The steady state and dynamical properties of the class of materials introduced above cannot be simply explained by their band structure but instead needs consideration of the 'correlation effects'. Photo-excitation above the gap from the LHB to the UHB in correlated systems leads to renormalization of the DOS as shown in figure 2.9. In equilibrium, the Hubbard bands are formed because of the electronic interactions (see figure 2.9 (a)). Photo-excitation above the band gap creates a hole and an electron in the LHB and the UHB respectively. Simultaneously, as mentioned earlier, the bands are modified as dictated by electronic density, in comparison to non-correlated systems where the bands are rigid as they are dictated by structural arrangement of the atoms and do not renormalize upon change in the carrier density of individual bands. The photoexcitation in correlated systems can initiate a number of dynamical processes in contrast to the systems with rigid bands.

Ultrafast optical spectroscopy (UOS) is sensitive to various degrees of freedom important in correlated systems and can unveil information on the numerous interactions happening in them. Materials with valence *d* and *f* electronic orbitals and correlated organic salts belong to this category and have demonstrated to have unique dynamical properties [9, 13, 63–65].

Preferential perturbations and probing targets

In general, photo-excitations investigated in condensed matter is aimed to perform one of the following actions:
(1) Transfer of charge fron one lattice site to next lattice site (changing filling per site)[66].
(2) Excitation of a lattice vibrational mode, either globally (changing the lattice structure) [14] or locally (in molecular solids) [18] (changing effective on-site and inter-site interactions).

The first kind of pertubation acts on the electronic degree of freedom (mostly lying in the near-infrared or visible frequency range) while the second kind does not involve any direct electronic transitions (lying in mid-infrared range) and acts on the structural degree of freedom. They aim to modify the ground state properties of the correlated systems through the following parameters:
(1) Number of electrons per lattice site via photo-doping.
(2) Effective interactions *i.e.* U/t and V/t via vibrational excitations.

After perturbing the solid, the optical properties give direct information on the pump-induced changes. The main goals of such measurements are the following.
(1) Control the phase transitions on femtosecond timescale.
(2) Understanding the role of entangled degrees of freedom towards a certain emergent phenomena.
(3) Search for hidden phases which are thermally inaccessible.

Photo-induced phase transitions by photodoping

Among the first studies in UOS are the photo-excitation of the correlated systems where the number of carriers are tailored with light and termed as 'photodoping'. However, photo-doping is different from chemical substitution. Chemical doping is mostly accompanied by changes in the atomic structure and composition and additionally dopes either electrons or holes whereas in photo-excitation, electron-hole pairs

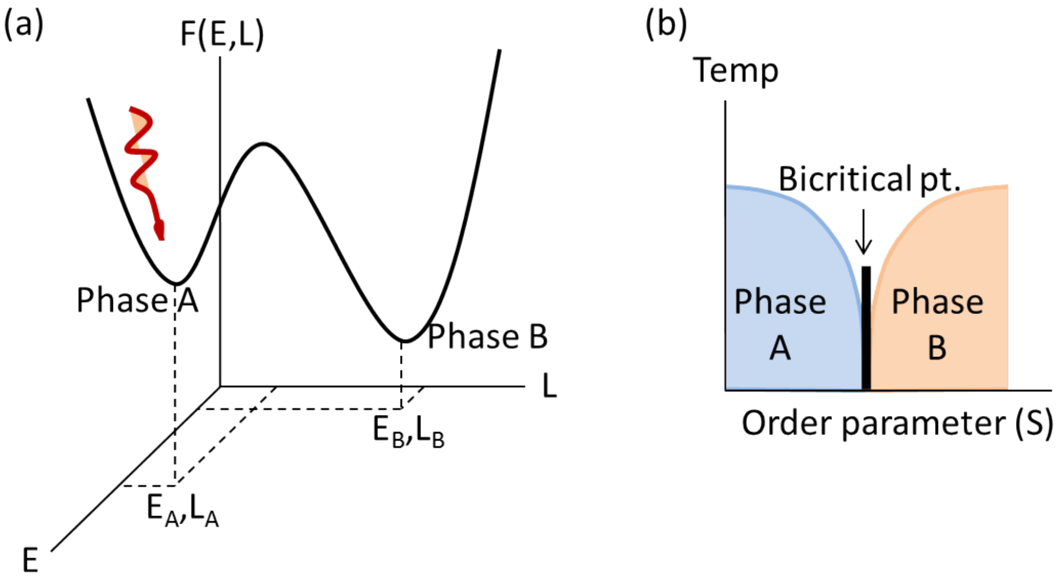

Figure 2.10: (a) Energy landscape with coupled order parameters E and L, going pump induced phase transition from phase A to Phase B (b) Competing two phase A and B around critical value of order parameter. Adapted from [67].

are transiently created without direct interaction with the lattice. By photo-doping, one drives the system in a higher energy non-equilibrium electronic distribution and probes the subsequent relaxation to equilibrium. Usually, photo-doping leads to the following two scenarios:

- Transition to a state which can be accessed thermally too. As is the case with $Pr_{0.7}Ca_{0.3}MnO_3$, carrier excitations in the near-infrared in this perovskite heats the electronic system. Consequently, the existing charge ordering melts and induces insulator-metal transition on ultrafast time scale [8, 9]. However, the ultrafast pathway taken to reach the final state by photo-doping is not due to laser heating but caused by photocarriers mediated collapse of the charge order and hence clearly such transition is different from the thermally induced ones. This scenario represents a very straightfoward consequence of excitation with light.

- The second scenario is photo-doped transition into a state, which is hidden in the equilibrium phase diagrams [6, 67]. A first order phase transition where two order parameters are coupled is atleast required to produce such a new state.

As an example for the second case, it is possible in strong electron-lattice coupled systems. Photo-doping act on the electronic structure (E). If E is now coupled to lattice structure (L), photo-excitation, would act on a joint set of order parameters (E,L) (see figure 2.10 (a)). Optical excitation of phase A (E_A,L_A) can emerge to the new phase B (E_B,L_B), almost energetically degenerate to equilibrium state but with different order parameters. Such a new metastable state was reported for photo excited charge and orbitally ordered manganite $Nd_{0.5}Sr_{0.5}MnO_3$ [10]. Thermodynamically inaccessible, charge and orbitally ordered, with new crystallographic parameters, what was observed by X-ray diffraction. The electronic changes induced with photodoping can translate into structural phase transitions. Photo-doping acts initially only on the electronic subsystem, with no direct interaction with lattice subsystem unlike thermal perturbations and later via electron-lattice coupling, acts on the lattice subsystem, driving the complete system into a new state [10, 11].

Another approach for photo-induced phase transitions (PIPT) are the one using the competing phases occuring in correlated systems (see figure 2.10 (b)). Thanks to the interplay of multiple degrees of freedom like charge, spin and orbital which form various electronic and structural ground phases in competition. Small tuning in the order parameter around the bicritical point can bring dramatic phase transition either on the microscopic scale or the macroscopic properties. Photo-exciting favors a phase with respect to the other and can lead to colossal changes in the properties of the material. As an example, manganite around half-filling typically show an antiferromagnetic charge and orbitally ordered insulating state competing with the ferromagnetic metallic phase [68, 69]. $Gd_{0.55}Sr_{0.45}MnO_3$ is a good candidate to understand this approach. It has an order parameter of average ionic radius $< Gd_{0.55}Sr_{0.45} >$ lying in the vicinity of bicritical point, separating above mentioned insulator and metallic phase. Photo-excition leads to an ultrafast change in the electronic state from the insulating to the metallic phase [69].

Vibrational perturbations

Vibrational excitations have direct access to the lattice degrees of freedom. As seen above for photo-doping, though acting on the electronic degree of freedom, indirectly can perturbe the lattice structure, exploiting electron-lattice coupling. The converse can very well be expected from vibrational excitations. Laser light directly couple to vibrational modes which are infrared active. Owing to symmetry, the lattice vibrations show a change in the electric dipole moment with the normal displacement coordinate and hence can be coupled to the electric field of the light. These mode selective excitations are less heat dissipative in contrast to the case of photo-doping, owing to their low photon energy as well as less number of accessible relaxation pathways. In general, these perturbations lie in mid-infrared region of the spectrum and to see the time averaged changes in the lattice structure, the driving field should be strong to access the non-linear couplings of the system. The mode selective vibrational perturbations have shown to open new pathways in the control of quantum material. A small change in the crystallographic constants can promote huge changes in the electronic [12–14] as well as magnetic properties [70].

Rini et al. observed a five order of magnitude decrease in the resistivity of perovskite manganite $Pr_{0.7}Ca_{0.3}MnO_3$ upon resonant vibrational excitation of an infrared active lattice mode at 17 THz [12]. This is explained on the lines of ionic Raman scattering (IRS) mechanism [71]. Under this process, optical rectification of the IR active mode into Raman modes happen via non-linear phonon coupling. The IRS considers the nonlinear coupling of the infrared active mode to the Raman mode and thereby allowing light to interact with the Raman mode of the system. The excited infrared mode result in the displacement of the lattice along the normal coordinate of the Raman mode. This mechanism has provided a distinct ultrafast route for lattice control [15, 70].

In $Pr_{0.7}Ca_{0.3}MnO_3$, the I-M transtion is understood in terms of substantial cubic harmonic coupling between its infrared active mode $B_{1u}(54)$ and Raman mode $A_g(9)$ [72]. On the line of IRS, the magnetic and orbital order parameter are shown to be controlled in $La_{0.5}Sr_{1.5}MnO_4$ by low-dissipative ultrafast lattice excitation [70]. The slow relaxation of both order parameters is understood as follows. The IRS drives the Jahn-Teller Raman active distortion leading to quenching of the parameters to a different value. The ultrafast control over magnetism with light certainly opens new avenues for their use in high-speed devices.

Another fascinating consequence of vibrational excitations is the recent observation of transient superconducing states [73–75]. D. Fausti et al. first showed the enhanced tunneling among the CuO_2 planes leading to transient superconductivity in vibrationally excited state which otherwise is a nonsuperconducting underdoped cuprate $La_{1.675}Eu_{0.2}Sr_{0.125}CuO_4$ [74].

2.4.1 Dynamics on fundamental time scales

Correlated systems show various emergent phenomena like superconductivity, antiferromagnetism and magnetic resonances (see figure 2.5). The microscopic mechanism behind many of the emergent phases is not very well understood. The clear understanding of microscopic physics behind ultrafast optical driven I-M transitions of TMOs, orbital or charge or spin ordered states is still lacking. The ultrafast pump-probe spectroscopy can provide a great deal of information on these emergent phenomena if their dynamics are probed on their fundamental time scale. It can tease apart the roles of individual degree of freedom in a certain broken-symmetry phase. The fundamental time scale associated to each degree of freedom is related to the relative energy scale.

If 'E' is the energy scale, then the time 'T' required to probe the corresponding process is given by Heisenberg relation:

$$T \geq \frac{\hbar}{2E} \tag{2.8}$$

Broadband, ultrafast spectroscopy is a tool to segregate the various degrees of freedom by mapping the time evolution of coherent excitations. Non-linear optical techniques enabled the generation of ultrashort laser pulses in visible and near infrared regions of the electromagnetic spectrum. As shown in figure 2.11, the fundamental time to measure the dynamics of electronic interactions are as fast as tens of femtoseconds.

However, to measure the electronic effect due to a phonon, a temporal resolution on the order of hundreds of femtoseconds (fs) is required corresponding to the oscillation period of the phonon (see figure 2.11).

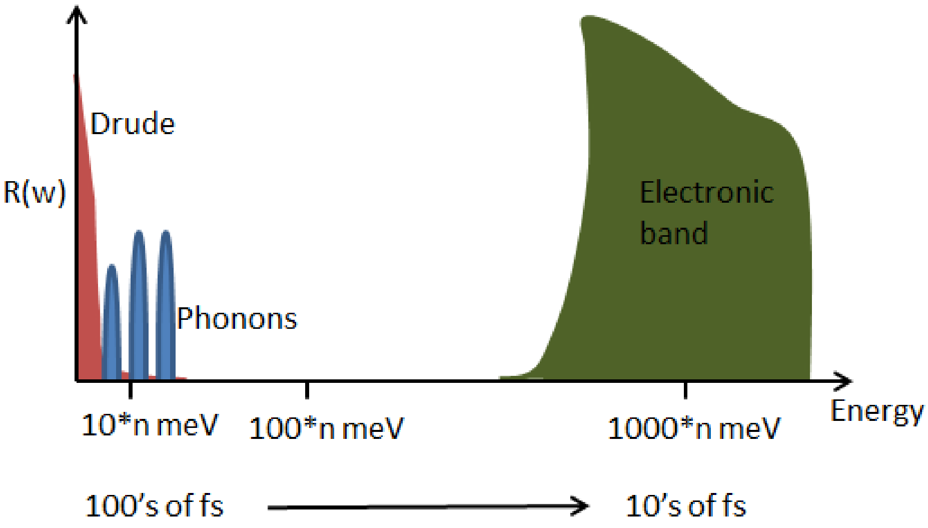

Figure 2.11: Electronic exctiations in condensed materials at various energy ranges with corresponding time to study them, $0 < n < 1$ [Adapted from [76]]

Here are a few examples where the dynamics were measured on the intrinsic time scale of the energy process, disentangling order parameters and understanding the ultrafast dynamics. As an example, photo-induced I-M transition is well known to occur in VO_2 after optical excitation [77, 78]. It accompains both symmetry changes in the unit cell and due to prompt creation of charges (thereby closing the Mott gap) as disclosed by optical and x-ray diffraction measurements [77, 78]. However the intriguing nature of this process was unclear whether the I-M transition occurs due to structural or electronic changes. In order to capture the nonequilibrium physics caused by optical hole doping, a temporal resolution on the time scale of movement of holes is required.

Cavalleri et al. measured the Mott gap with 15 fs resolution *i.e.* on the fundamental time scale of hole doping of the system [79] to evidence a time-domain hierarchy between various effects. Despite the fast hole doping, the I-M transition are as slow as 75 fs. The bottleneck time is approximately half period of the two coherent modes (consistent with Raman spectroscopy) observed during relaxation of the driven state. Clearly, the lattice and charge degree of freedom could be disentangled in VO_2 based on their different dynamical responses, implying that the transition is not a simple case of melting of the electronic order but is due to structural motion caused by optical phonons.

On similar lines, the microscopic pathway for charge-density waves (CDW) ordering establishes the electronic correlations to be the major factor behind the stabilized order. In the two-dimensional Mott insulator 1T-TaS_2, this was investigated using sub-30 fs angle-resolved ultraviolet photoemission spectroscopy [80]. The CDW is formed through Peierls distortion leading to redistribution of changes via electron-phonon coupling. The measurements shows that photoexitation leads to prompt melting of the Mott gap at the Fermi level (faster than 30 fs) but slow melting of CDW gap on sub-vibrational time scales (nearly 200 fs). This suggests the closing of CDW gap happens due to charge disordering rather than atomic repositioning, underlining the central role of electron-electron interactions in CDW formation.

The roles of electronic and lattice degrees of freedom was also decoupled in a frustrated superconductor $La_{1.875}Ba_{0.125}CuO_4$ using femtosecond soft X-ray diffraction. By resonantly exciting the Cu-O stretching mode at 14.5 μm it was revealed that the low temperature tetragonal (LTT) distortion peak still persists on time scale of few picoseconds when the charge stripe order peak has disappeared [81], demonstrating that charge order alone is likely the reason for the quenching of three dimensional superconductivity in this compound.

The interaction energies *i.e.* on-site and inter-site interaction energy U and V and hopping integral t defines the electronic properties as shown in section 2.3. For the case of Mott insulator, $U, V > t$. Correspondingly, the dynamics associated to U and V having hundreds of meV energy scale, would happen on the fast time scale of few femtoseconds. Consequently, in order to probe and access the role of say 'U' towards a certain emergent phase, temporal resolution tens of fs would be required for strongly correlated systems. 't' with much lower energy scale has longer time of hopping of electron associated. As an example, S. Wall et al. showed the coherent dynamics in the strongly correlated organic salt ET-F_2TCNQ during the melting of the Mott order. It happens as superposition between the bound holon-doublon and unbound holon-doublon pairs. To probe that coherence, a fast response was needed on the timescale of hopping to see the delocalization dynamics of electrons. The time resolution corresponding to hopping integral energy 't' (h/ (t=40 meV) = 40 fs) was employed [53].

3 Manganites and their physical properties

The term "Manganite" is widely referred to the manganese oxides containing trivalent and/or tetravalent manganese ions [82]. They are one of the most extensively studied materials in the condensed matter community. Prototypical of systems with strong electronic correlations, they exhibit complex interplay between charge, spin, orbital and lattice degree of freedoms. Depending on the doping with rare-earth and alkali compounds, different ratio of Mn^{3+} and Mn^{4+} ions can be acheived in the manganites. The undoped compound has only Mn^{3+} ions and as the doping level increases, an equivalent number of manganese ion change their valency from 3+ to 4+. These doped compounds upon change of temperature, show a variety of emergent electronic, magnetic and structural phases, such as ferromagnetism, antiferromagnetism, charge and orbital ordered states. These phases further can undergo structural, electronic and magnetic transitions on application of other external forces like pressure, magnetic field etc.

The resistivity of manganites have huge dependence on the magnetic field. This phenomenon in physics is termed as colossal magnetoresistance (CMR). The resistivity changes up to nine orders of magnitude on applying external magnetic field [41]. The term colossal has been used for manganites to distinguish their effect from the giant magnetoresistance (GMR) reported in some multilayer metallic films [42]. Figure 3.1 shows this phenomenal feature of manganite which has also made it a potential candidate in spintronics industry in search of smallest-fastest devices. Though the physics of CMR is quite complex, in a simplest scenario, it can be understood from the double-exchange (DE) model, discussed later in this chapter.

3.1 Structural and electronic properties

Manganites with general chemical formula, $RE_{1-x}AE_xMnO_3$ have a perovskite-type crystal structure shown in figure 3.2. Here RE stands for trivalent rare earth elements

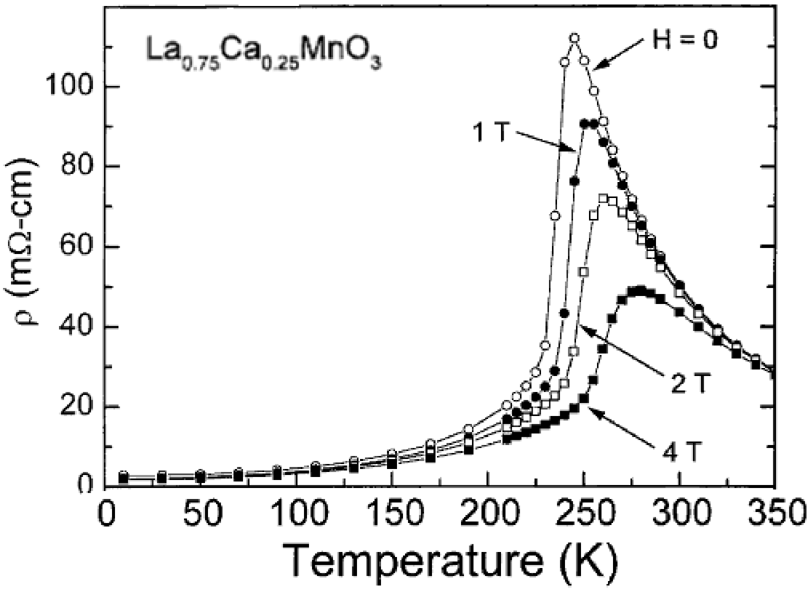

Figure 3.1: Resistivity of $La_{0.75}Ca_{0.25}MnO_3$ as function of temperature at various applied magnetic fields [Adapted from [83]].

like La, Pr, Y etc and AE stands for the divalent alkaline earth elements like Sr, Ca, Ba etc. They occupy the corners of the cubic unit cell with manganese at the center and six oxygen atoms at the center of six faces of the cube.

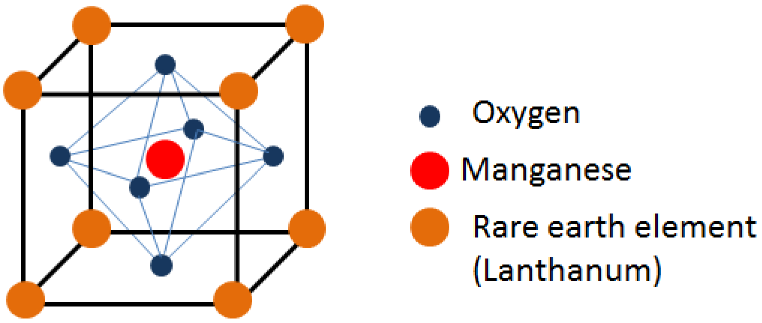

Figure 3.2: Cubic perovskite structure of $LaMnO_3$

These perovskite based structures occasionally show deviation from perfect cubic lattice. One of the two main reasons for this modification is the radii mismatch between the manganese ion and the average ionic size for $RE_{1-x}AE_x$ sites. Quantitatively, this effect is expressed in term of 'tolerance factor' (f), defined as :

$$f = \frac{r_{Mn} + r_O}{\sqrt{2}(r_A + r_O)}$$

Here, 'r_A' denote the average ionic size at the $RE_{1-x}AE_x$ sites. r_O and r_{Mn} stands for the ionic size of oxygen and manganese ions respectively. If f is close to one, cubic structure is likely to happen. As the value of f decreases or equivalently, r_A increases, the lattice structure reshapes to rhombohedral for $0.96 < f < 1$ and then to orthorhombic for $f < 0.96$. Any deviation of 'f' from value one, implies bending of the Mn-O-Mn bond angle and a decrease in the effective overlap between Mn 3d-orbitals and oxygen 2p-orbitals. This buckling of MnO_6 octahedra is a common feature of the manganites.

Also, the manganites are classified into three different branches based on the value of tolerance factor namely low, intermediate and high electronic bandwidth manganites.

1) High bandwidth manganites: These represent the class of manganites where the size of parent ion and dopant ion at A site are well matched. $La_{1-x}Sr_xMnO_3$ is one such example. They are characterized by high Curie temperature and are ferromagnetic metallic in large regions of the phase diagram. Metallicity is achieved via the easy hopping of electrons from one manganese lattice site to another.

2) Low bandwidth manganites: These represent poorly matched parent and dopant ionic sizes, where the overlapping electronic bandwidth is greatly reduced. They are characterized by huge anitferromagnetic insulating region in the phase diagram. Hopping across the lattice site is reduced. $Pr_{1-x}Ca_xMnO_3$ is a well known example.

3) Intermediate bandwidth manganites: These manganites have hopping amplitude in between the above two categories. The ferromagnetic metallic (FM) phase is in narrow region for this set of compounds, of which $La_{1-x}Ca_xMnO_3$ is an example.

These materials display rich structural, electronic and magnetic phase diagram obtained upon doping and as a function of temperature as shown for $Nd_{1-x}Sr_xMnO_3$ in figure 3.3. Upon changing the doping concentration(*i.e.* varying x from 0 to 1) at high temperature, the change in the tolerance factor modifies the structure of the lattice from an orthorhombic phase (i.e.) O' ($a \approx b > c$) to O ($a \approx b < c$).

The second reason for the deviation from cubic lattice structure among perovskites is attributed to Jahn-Teller distortions (JTD). These distortions in general are inherent to systems containing either one e_g electron as in Mn^{3+} or one e_g hole as in case of Cu^{2+}. Let us consider a Mn ion in a perovskite structure, which is surrounded by six oxygen ions O^{2-}. The octahedral geometry of the ligands affects differently the energy level of otherwise degenerate Mn 3d-orbitals. The orbitals which are closer to the ligand's electron cloud lift in energy, owing to Coulomb repulsion, forming a subset e_g (d_{x2-y2},

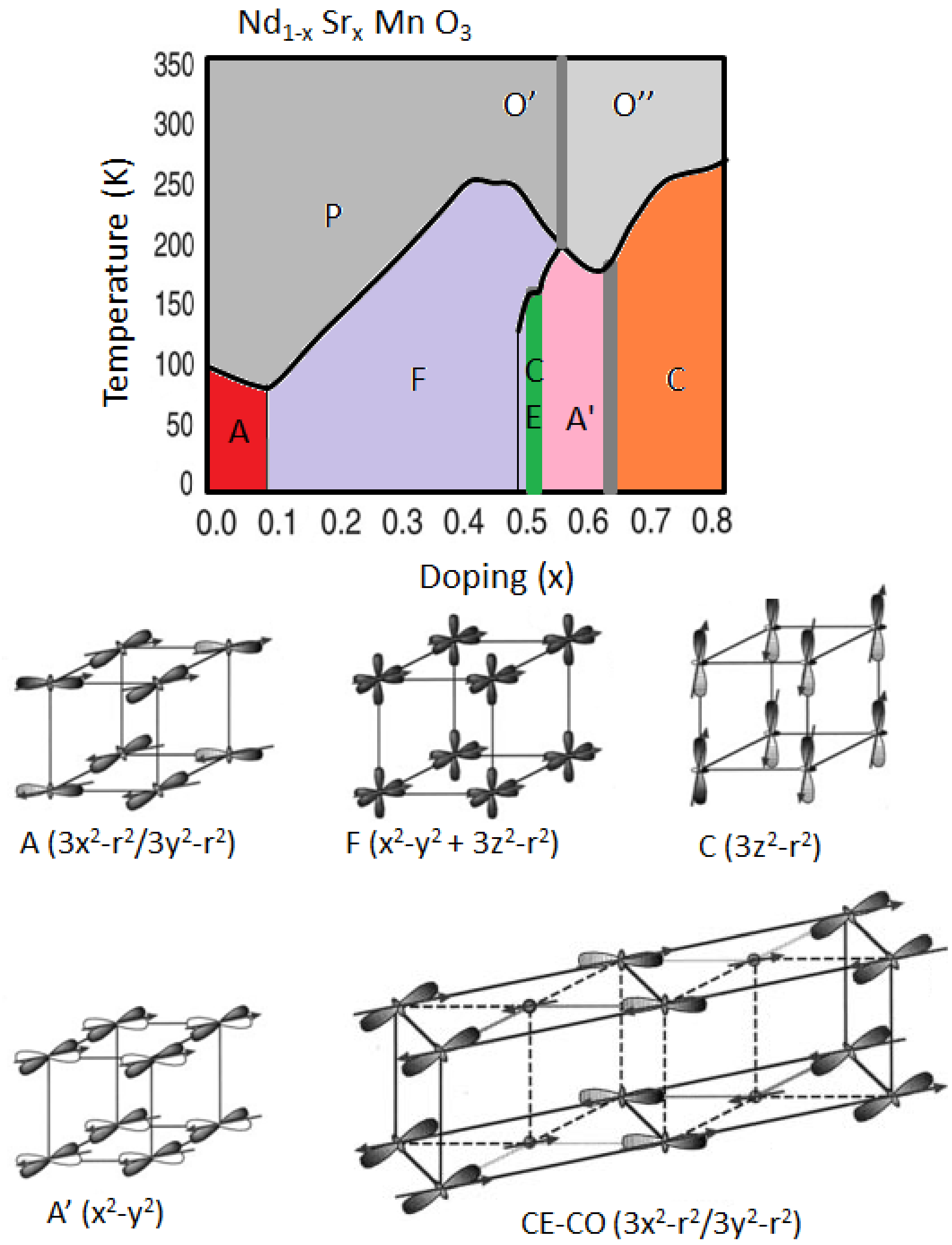

Figure 3.3: Structural, electronic, magnetic and orbital phases and transition in $Nd_{1-x}Sr_x$MnO$_3$ for different doping concentration x as function of temperature. The abbreviations used are paramagnetic (P), ferromagnetic (F), A-type antiferromagnetic (A), C-type antiferromagnetic (C), CE-type antiferromagnetic along with charge order (CE), orthorhomic lattice with a $\approx$ b $>$ c and a $\approx$ b $<$ c (O and O') [Adapted from [84]].

d_{3z2-r2}) of higher lying orbitals. The orbitals pointing towards the nodal planes of the ligand do not change much in energy, forming a lower lying energy orbital subset t_{2g} (d_{xy},d_{yz}, d_{zx}). This so-called crystal field splitting is estimated to be of the order of 1 eV. [23]. All the three 3d-electrons in Mn^{4+} occupy the t_{2g} ground state with parallel spin (S = 3/2) in accordance with Hund's rule. In Mn^{3+}, the fourth electron occupies the higher energy state e_g being the Hund's energy (JH) greater than the crystal field splitting energy. The spin of electron in e_g orbitals stays parallel to the background spin of t_{2g} orbitals subset, governed by same intra-atomic Hund's interaction thereby assigning a total spin of S = 2 for Mn^{3+} ion.

The energy and symmetry of the overall system is further reduced through a modification of the crystal structure. This happens via the elongation of the cubic lattice along the z-direction. The apical oxygen ions move away from Mn ion, resulting in decrease of energy level of $d_{3z^2-r^2}$ orbital, owing to less Coulomb repulsion between the two (see figure 3.4). This effect stabilizes the system energetically and is known as Jahn-Teller distortion. For the same reason, there is lifting of degeneracy of t_{2g} orbitals with d_{yz} and d_{zx} lying lower in energy compared to d_{xy} as shown in the figure 3.4. JTD can also occur through compression of the octahedra along the z-axis (not shown in the figure) where also the split of e_g and t_{2g} levels occurs such that the orbitals with z component go higher in energy.

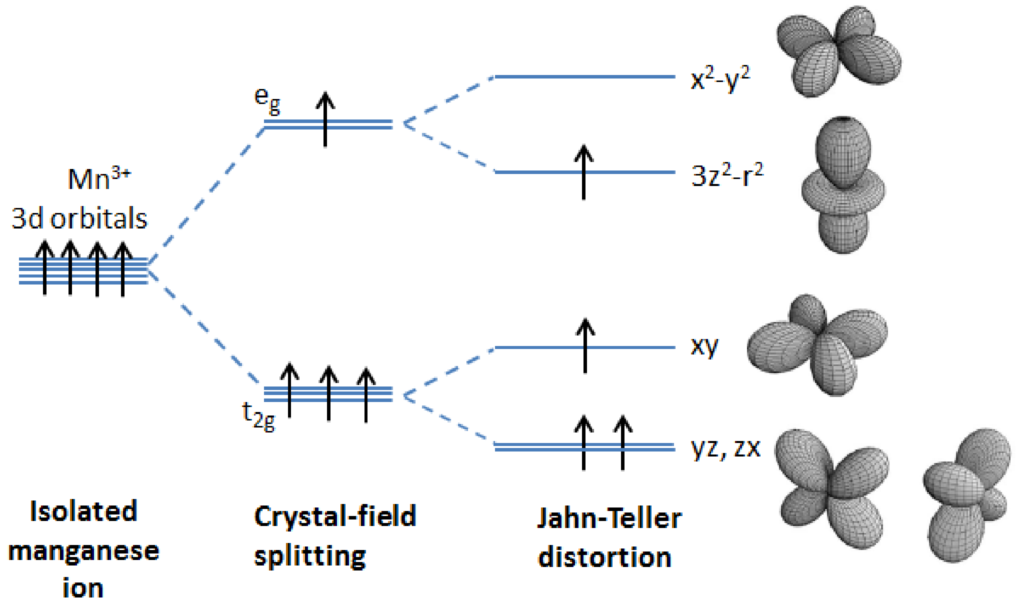

Figure 3.4: Energy diagram of 3d-orbitals of Mn^{3+} ion in an isolated state (left), in a crystal lattice (middle) and under Jahn-Teller distortion state(right)

Other significant structures have been derived from the perovskites known as Ruddlesden-

Popper series. These are layered perovskites with unit formula as (RE and/or AE)$_{n+1}$Mn$_n$O$_{3n+1}$ (see figure 3.5). Here n is the number of Mn-O sheets in a unit cell. As an example, (La,Sr)$_2$MnO$_4$, also known as (214) system has one sheet of Mn-O layer in its building block.

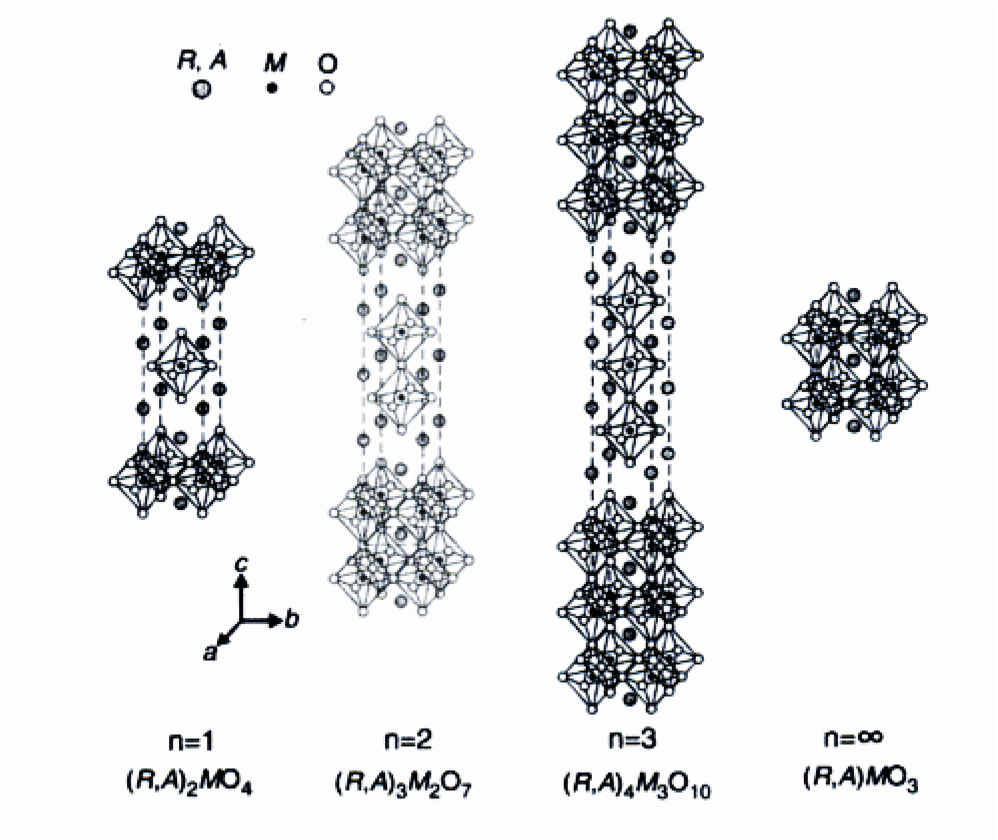

Figure 3.5: Ruddlesden-Popper series of manganites [Adapted from [85]].

3.2 Magnetic properties

As mentioned earlier, the manganites show different magnetic phases like antiferromagnetic, ferromagnetic and paramagnetic depending on doping and temperature (see figure 3.3). For low temperatures, the magnetic phases show sharp transitions as a function of doping. These magnetic phases play influential role on the macroscopic property of the material. One example is the existence of CMR in the ferromagnetic phase of doped manganites. There are two types of magnetic exchange interactions namely superexchange and double exchange, which convincingly explain most of the magnetic properties.

3.2.1 Superexchange interaction:

In manganites, magnetic cations (Mn^{3+}) are separated by non-magnetic anions (O^{2-}). Hence the direct exchange interaction between Mn^{3+} ions is negligible, but happens dominantly via the oxygen ions. The interaction is large for the highest overlapping orbitals; in this case, the e_g orbital of the manganese ion Mn^{3+} and the 2p orbital of bridging oxygen ion. The e_g and t_{2g} states are in high spin configuration owing to Hund's rules. The hopping of electrons from Mn^{3+} via O^{2-} to the neighbouring Mn^{3+} can reduce the energy of the system, provided both the cations are antiferromagnetically aligned with respect to each other. The ferromagnetic exchange would create two up (or down) spins in an orbital, prohibited by Pauli's exclusion principle. This type of indirect magnetic interaction, which favours antiferromagnetism, is called superexchange.

3.2.2 Double exchange interaction

Zener introduced the concept of Double Exchange (DE) in doped manganese oxides in 1951 [86]. This concept relies on the fact that the two configurations, Mn^{3+}-O^{2-}-Mn^{4+} and Mn^{4+}-O^{2-}-Mn^{3+} are degenerate. The electron from one of the Mn^{3+} site hops to the orbitally overlapping O^{2-} site with simultaneous hopping of its 2p electron to the neighboring Mn^{4+} site, as shown in figure 3.6.

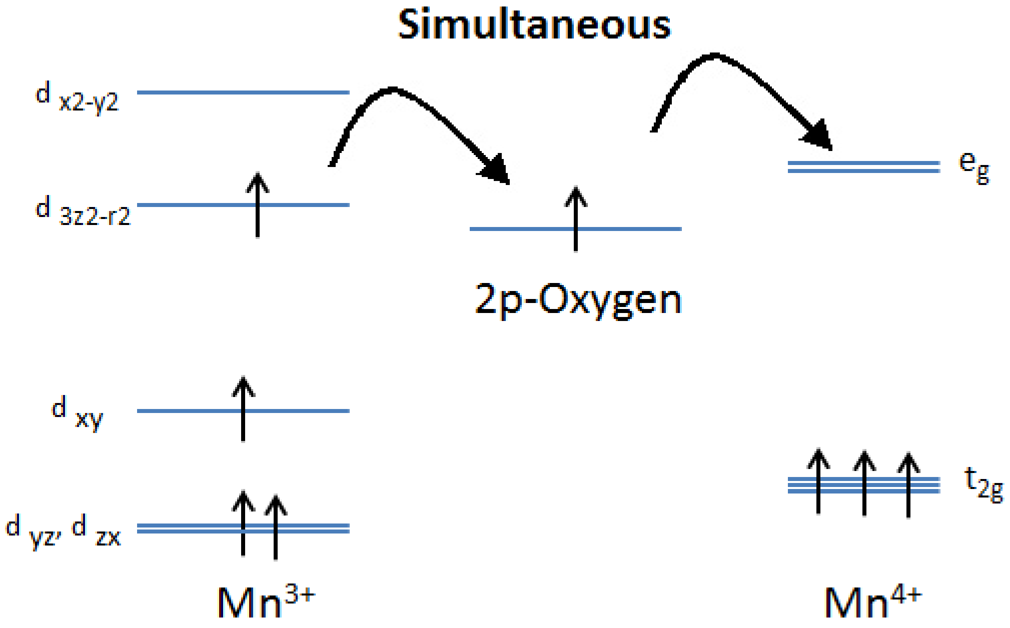

Figure 3.6: Schematic diagram of double exchange interaction

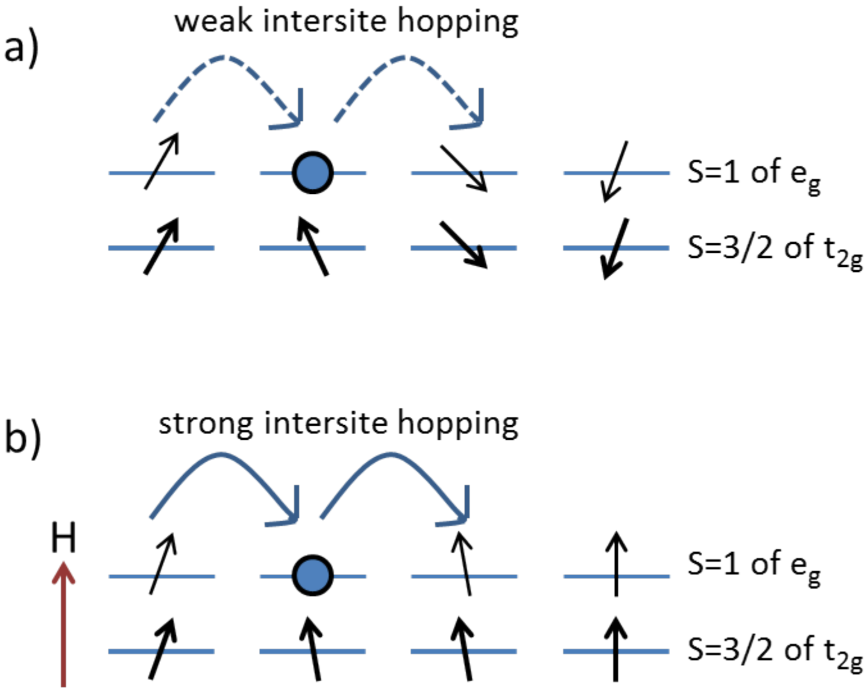

Figure 3.7: Schematic diagram showing (a) weak effective intersite hopping due to unordered spin near Tc (b) strong hopping on application of external magnetic field H

Such an exchange is possible only when localized t_{2g} spins at neighboring sites are ferromagnetically aligned, owing to strong on-site Hund's coupling between t_{2g} and e_g electrons. The effective intersite hopping amplitude between the adjacent sites i and j of Mn^{3+} and Mn^{4+} is quantitatively given by the Anderson-Hasegawa relation, $t_{ij} = t_{ij}(0) \cos(\theta_{ij}/2)$, where θ_{ij} is angle between neighboring core spins (*i.e.* t_{2g} spins) and $t_{ij}(0)$ is the intersite hopping interaction. Clearly, hopping is favored for parallel adjacent spins *i.e.*$\theta_{ij} = 0$. This ferromagnetic interaction leading to simultaneous double time exchange of electrons is termed as 'Double exchange interactions'.

At the Curie temperature, due to thermal entropy, the electron spins of e_g (parallel to t_{2g}) at each Mn^{3+} site are randomly aligned, allowing only weak intersite hopping interaction. By applying external magnetic field H, as shown in figure 3.7 each of these e_g spins are aligned in the direction of H, leading to decrease of angle θ_{ij} and thereby an increase of an effective hopping amplitude. The resultant increase in conductivity observed is the well-known CMR.

3.2.3 Goodenough-Kanamori-Anderson rules

A number of rules which determine the strength and sign of exchange interaction between two manganese ions bridged by an oxygen ion is given by Goodenough-Kanamori-Anderson rules (GKA) [87] (see figure 3.8).

1) The magnetic exchange interaction of two half-filled manganese orbital and two empty manganese orbital results in antiferromagnetism.

2) The magnetic exchange interaction of one half-filled and one empty/completely filled manganese orbital leads to ferromagnetic (FM) ordering.

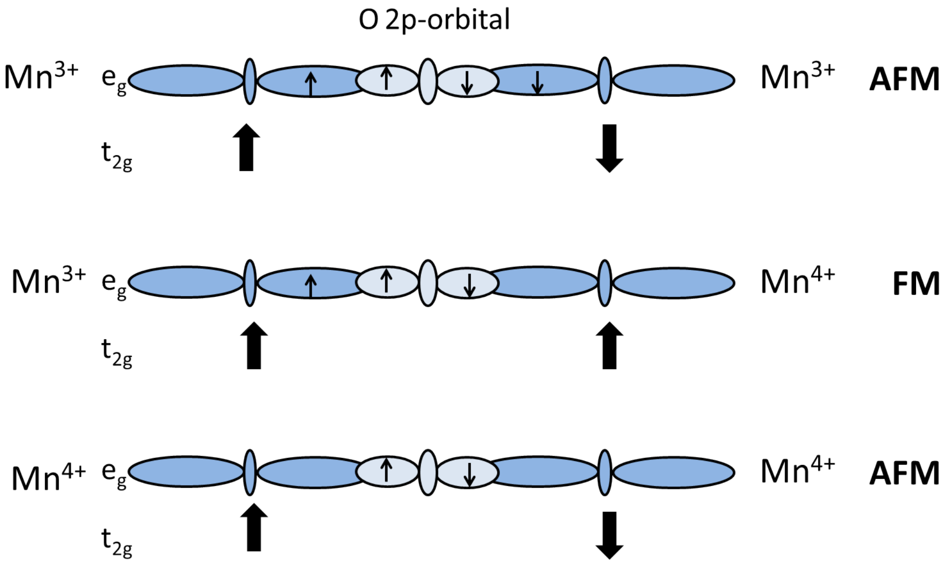

Figure 3.8: Schematic diagram of magnetic exchange interaction between neighbouring Mn ions following Goodenough-Kanamori-Anderson rules

3.3 Orbital physics of manganites

The orbital degree of freedom plays an important role in the electronic and magnetic properties in perovskites. The steep insulator-metal transition and CMR in manganites is argued to happen in response to ordering of orbitals [40]. The state for which e_g orbitals of Manganese ion attain directionality, giving overall a long range orbital pattern to the crystal is termed as orbital ordering. Orbital ordering has been reported in many manganites using X-ray diffraction techniques [88–90]. Figure 3.3 shows various kinds of orbital ordering in $Nd_{1-x}Sr_xMnO_3$ as function of doping. A-type and C-type orbital ordering implies the alignment of $3z^2$-r^2 orbital in xy plane and along z-axis respectively. The CE-type orbital ordering involves $3z^2$-r^2 and is accompained by charge ordering as well. This ordering is found near half-filling, where an equal number of Mn^{3+} and Mn^{4+} ions are present (shown in green).

The orbital ordering itself is stablized by simultaneous support of two factors:
(1) Cooperative Jahn-Teller distortion
(2) Electronic exchange interactions.

In the next chapter, we will study the orbital physics in a half doped prototypical manganite compound, aiming at unveiling the origin of orbital ordering present in it.

4 Ultrafast melting of orbital ordering in $La_{0.5}Sr_{1.5}MnO_4$

4.1 Manganite $La_{0.5}Sr_{1.5}MnO_4$

Manganites offer a wide field to investigate the interplay between charge, spin, orbital and structural degrees of freedom. The microscopic understanding of these is of huge importance to characterize the emergent macroscopic properties shown by manganites. Among these charge ordering, orbital ordering and the collective Jahn-Teller structural distortion are considered to play an important role in the colossal magnetoresistance state [4, 91]. This chapter brings forward the microscopic orgin behind the orbital ordered state present in these compounds at low temperatures. We have studied a half-filled perovskite manganite $La_{0.5}Sr_{1.5}MnO_4$ (LSMO), known to exhibit real space ordering of charges and concomitant orbitals. As was outlined in the previous chapter, the OO state is upheld by the cooperative JTD and electronic exchange interaction. We disentangle their role towards the ordered state on their inherent time scale using 4 fs laser pulses. Such an extreme time resolution is required to be able to separate fast electronic motion from the slow lattice response.

4.1.1 Charge and orbital ordering in $La_{0.5}Sr_{1.5}MnO_4$

$La_{0.5}Sr_{1.5}MnO_4$ is a single layered perovskite with n=1 in the Ruddlesden-Popper series. The half doped (214) system has K_2NiF_4 type crystal structure containing the same number of electrons and holes. All the manganese ions at room temperature are crystallographically equivalent with an average valency of 3.5. Below $T_{CO/OO}$ = 220K, LSMO undergoes transition in which the manganese ions at neighbouring sites undertake valences of 3+ and 4+ [21, 92]. Mn^{3+} and Mn^{4+} align in checkboard pattern in MnO_2 plane forming a charge ordered (CO) state as shown in figure 4.1. Electron diffraction studies on this compound revealed the occurrence of real space ordering of Mn^{3+} and Mn^{4+} ions [21, 93]. The picture of integer value of valency of manganese ions has been under debate implying that manganese ions have valencies 3.5 + δ and 3.5 - δ, where δ is less than 0.5 [94]. This assumption however did not consider the covalency and Hartree-Fock calculations on another manganese compound $La_{0.5}Ca_{0.5}MnO_3$ which shows the valencies closer to 3+ and 4+ [95]. For this thesis, we will be using integer valencies only. Elastic neutron scattering measurements further confirmed charge and magnetic order in the compound [92]. Orbital ordering is also established concomitantly to charge ordering. The half filled e_g orbitals of Mn^{3+} ions align along the yellow zig-zag chains shown in figure 4.1. X-ray diffraction studies near Mn K-absorption edge showed direct observation of charge and orbital ordering [22, 96]. Further cooling below T_N = 110K leads to magnetic phase transition. The magnetic spins align themselves in ferromagnetic fashion along the zig-zag chain (shown in yellow in figure 4.1), which is antiferromagnetically aligned to the neighbouring ferromagnetic zig-zag chain. Out of plane, the spins align in antiferromagnetic configuration, confirmed by X-ray diffraction measurements (not shown here).

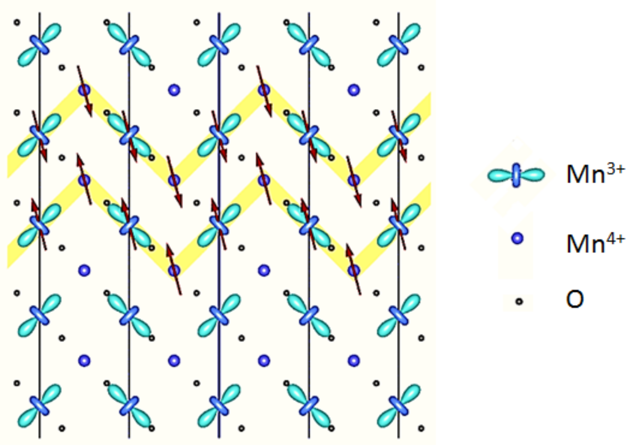

Figure 4.1: Schematic diagram of in-plane (wave vector (1/2,1/2,0)) charge and orbital ordering in $La_{0.5}Sr_{1.5}MnO_4$, together with ferromagnetic spin alignment of manganese ion along the zig-zag yellow chains.

4.1.2 Factors responsible for orbital ordering

Over the past few decades, there has been a lot of effort to gain the microscopic insight into the orbital physics. One of the biggest quest of the field is to unveil the reason behind this ordered state. As mentioned in the earlier chapter, the orbitally ordered state in the manganites is stabilized via two major phenomena: electronic exchange interaction and the cooperative Jahn-Teller distortion (JTD) [91]. Both factors are strongly tied to each other and are treated as single order parameter in any analysis. However, it is unknown which among the two is the absolute driving force initiating OO. It has been suggested to be either of electronic orgin [97] or in contrast is JTD driven [98]. Experimentally, static techniques like soft x-ray diffraction have been employed to understand the leading force. However, the allotment of various features in the spectra to a certain degree of freedom is unclear. Soft x-ray diffraction on Mn L edge, being more sensitive to OO, has also been applied but the results were not direct enough to give us a concrete answer [88]. The absolute driving force initiating OO is still an open question [99, 100].

Both driving factors can be very well appreciated from figure 4.2. As we learned in last chapter, JTH leads to the extension or compression of oxygen octahedra around the Mn^{3+} ion along z- direction. In LSMO, 'cooperative JTD' plays the role where the extension of an oxygen octahedra at a Mn^{3+} site is accompained by the compression of the oxygen octahedra at the neighbouring site. This cooperative behaviour of alternate extension and compression in the MnO_2 plane leads to stabilization of the observed orbital pattern, shown in figure 4.2. Apart from structural modifications, the electronic interactions, mainly double exchange interaction along zig-zag chain and super exchange between the adjoining chains, also contribute to a stable orbital ordering. According to the Goodenough-Kanamori-Anderson rule, such electronic interactions favors the above mentioned geometrical orbital arrangement (See section 3.2) [87]. It is difficult to say which one is more relevant to stabilized OO in the compound. Our experiment tries to solve this chicken and egg question.

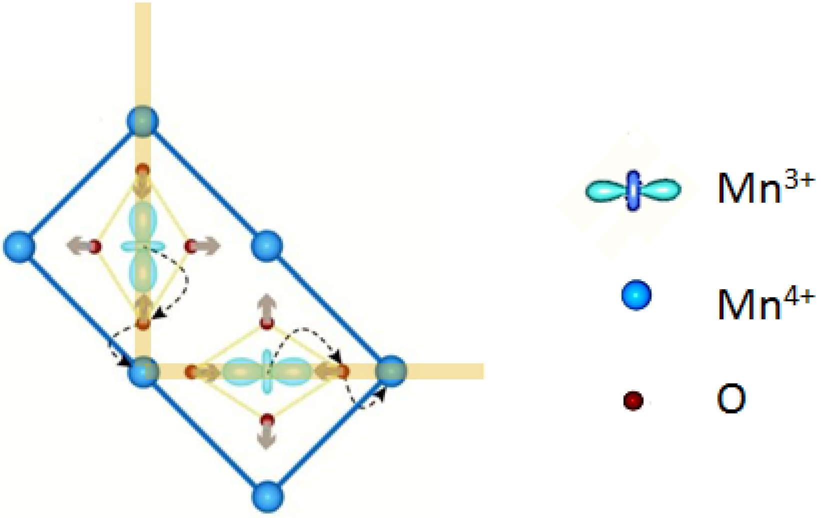

Figure 4.2: Zoom in on the zig-zag chain (yellow). Extension of one oxygen octahedra in one direction is accompained by compression of other octahedra along the chain. Dashed arrow shows the electronic exchange interaction among Mn^{3+}, O and Mn^{4+}.

4.1.3 Optical birefringence of orbital ordering

The reflectivity spectrum of $La_{0.5}Ca_{0.5}MnO_3$ at different temperatures has been measured by Ishikawa et al. [101]. The corresponding optical conductivity obtained by applying Kramers-Kronig transformations is shown in figure 4.3 (left panel). The in-plane conductivity spectrum at 290 K (above all ordering temperatures) shows a broad peak at nearly 1 eV. With decrease in temperature, the charge transfer peak blue shifts in energy and the gap increases corresponding in size, meaning increased insulating character at low temperature.

There is another important point of disparity. Unlike, the spectrum for 290 K, the spectrum at 10 K shows a different behavior for different polarizations of the electric field. This is understood as follows. At low temperatures, in presence of orbital ordering, LSMO exhibits optical anisotropy in the ab-plane. The chemical unit cell of LSMO gets doubled in case of a charge ordered state, as shown in red in figure 4.4. Further, orbital ordering creates an asymmetric orbitally ordered unit cell as shown in dark blue in figure 4.4. Because of this asymmetric OO unit cell, the system responds differently to electric fields along the a′ and b′ directions. Or, in other words, if the electric field is linearly polarized along a-axis, then the reflected beam will be elliptically polarized and will have unequal components along the optical axes. This difference is known as optical birefringence and is a direct measure of optical anisotropy induced by OO. In the optical spectra, this difference is reflected as the difference in their response along the optical axes (a′ & b′). The corresponding optical birefringence signal as a function of temperature in LSMO measured by Ishikawa et al. and is shown in the right panel of figure 4.3. Above $T_{CO/OO}$, the system is isotropic and hence there is no birefringence signal. Below the ordering temperature of 220 K, birefringence increases and saturates below T_N = 110 K. This suggests that the antiferromagnetic ordering below T_N quenches the CO/OO state. Probably in the spin ordered state the hopping integral is enhanced due to favoured electronic exchange interactions along the zig-zag chains [101].

4.2 Ultrafast observation for melting of orbital order

Our aim is to understand the microscopic mechanism behind the OO state and disentangle the contributions coming from JTD and electronic interactions. We have approached the problem with a novel, direct door of ultrafast spectroscopy. Our approach to solve this issue relies on the fact that the dynamical behaviour of the two stablizing forces will be different owing to the simple fact that one of electronic orgin should happen on a faster timescale than that of structural origin. Photo-doping at the

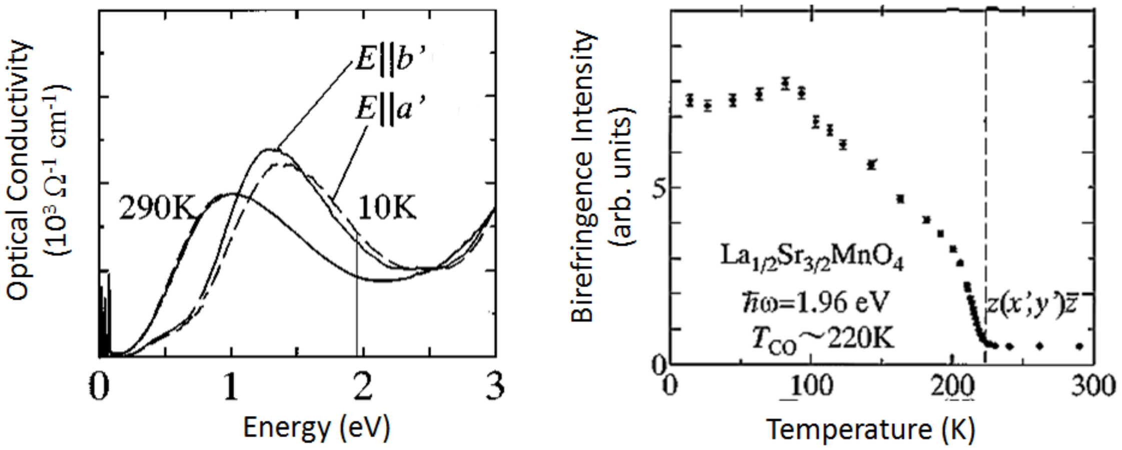

Figure 4.3: Left panel: Optical Conductivity along optical axis a′ and b′ at temperatures of 290 K and 10 K. Right panel: Variation of birefringence signal as a function of temperature for $La_{0.5}Sr_{1.5}MnO_4$ [Adapted from [101]]

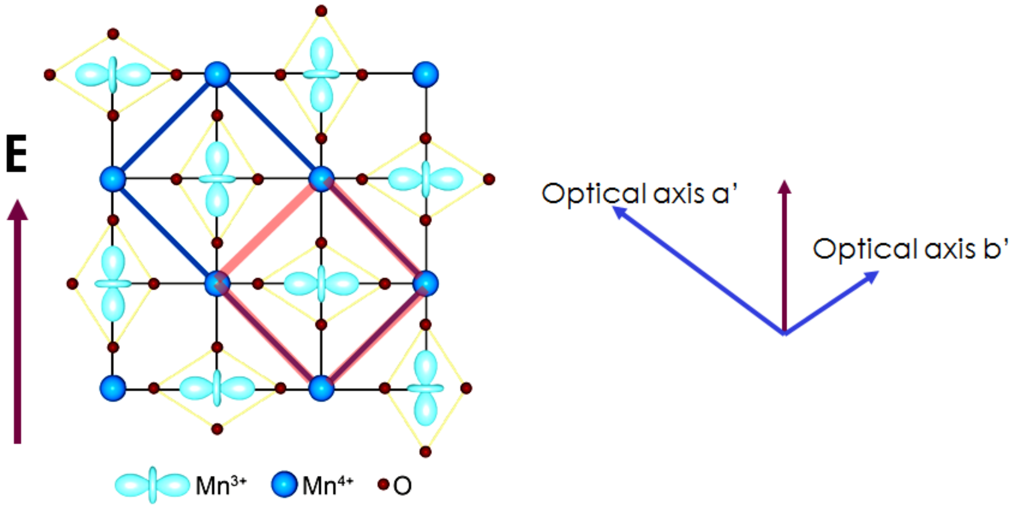

Figure 4.4: MnO_2 plane of LSMO crystal structure together with charge ordered unit cell (red square) and the orbital unit cell (blue rectangle)

charge transfer (CT) resonance results in excitation of e_g electrons from Mn^{3+} to Mn^{4+} site along the ferromagnetic chains. Owing to the strong on-site Hund's coupling, the Mn^{3+} e_g electron do not hop to Mn^{4+} ion in other antiferromagnetic chain [102]. The transfer of change along the chains results in destruction of the CO/OO state (as shown in figure 4.5). Ogasawara et al. were the first one to observe the photo-induced melting of the ordered state. Pumping the CT band with 800 nm laser light and probing the band with 200 femtosecond (fs) long pulses in the spectral range from 400 nm to 2500 nm, they show shift of the peak of the CT band and decrease of optical birefringence suggesting the destruction of the CO/OO state [66]. These photoinduced changes are different from the thermal excitation of ordered state. While the thermally disordered state shows a broadening of the CT peak, the optical excitation results in a narrowing of the peak [66, 101]. Ehrke et al. also showed partial melting of orbitally ordered state in $La_{0.5}Sr_{1.5}MnO_4$, using resonant soft x-ray diffraction (RSXD) [103]. But these experiments do not have the time resolution to see the early dynamics of the melting process.

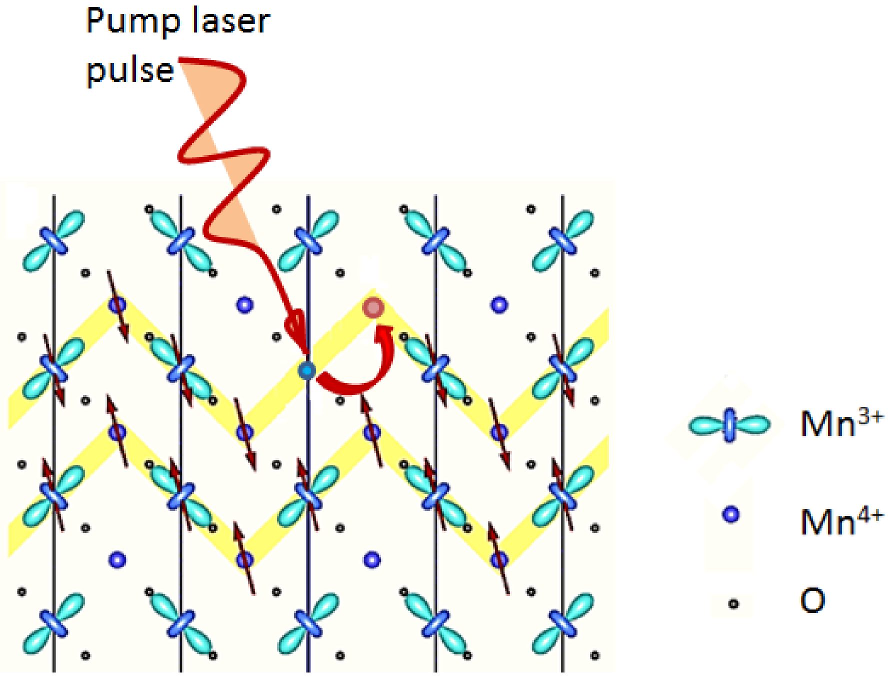

Figure 4.5: Pump laser pulse induces transfer of charge from Mn^{3+} site to neighbouring Mn^{3+} in ab-plane of LSMO.

A temporal resolution of few femtoseconds is required to reach to the typical time of motion of electrons [104]. An extreme time scale of ~ 4fs is used to exploit the separation of timescales between different processes. Based on both high temporal resolution (approaching the single-cycle limit) and the ultra broad band-width, we have been able to access the electronic dynamics on the time scale faster than the highest-frequency lattice dynamics.

4.3 Generation of 4 fs laser pulses in the visible/NIR

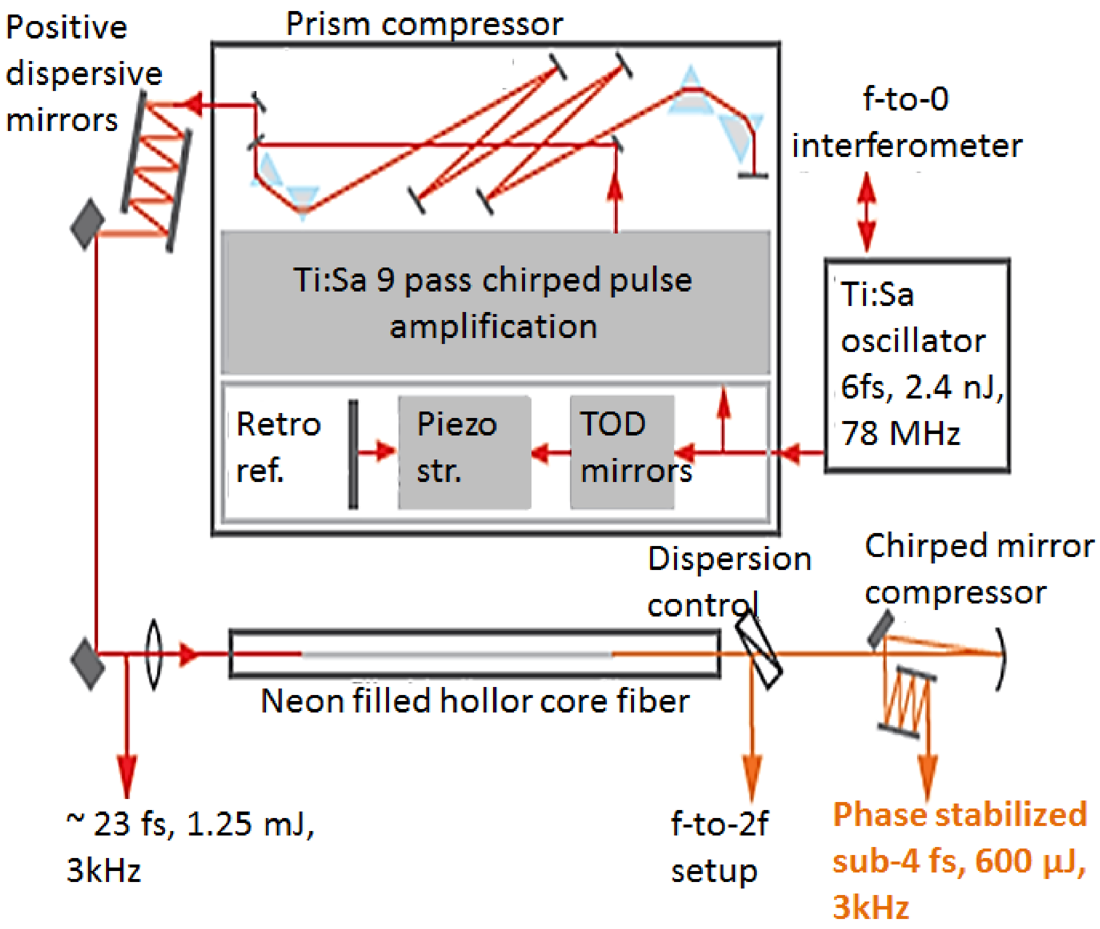

Figure 4.6: The setup for generation of sub-4 fs spectrum in visible/NIR region.

In this section the laser system for the generation of the few-cycle laser pulse will be briefly described. A more detailed description can be found in reference [105]. The laser system delivers sub-4-fs laser pulses in the visible to the NIR range, spanning from 450 nm to 1050 nm with pulse energies upto 500 μJ. In figure 4.6 a schematic of the laser system is shown. Starting from Ti:Sa oscillator, and going into Ti:Sa amplifier following positive dispersion compensation, we obtain the broad spectrum shown in figure 4.7(a). The laser system is equipped with a hybrid prism/positively chirped mirrors compressor, avoiding the spectral narrowing due to self phase modulation (SPM) in the prism material. Figure4.8(a) and (b) show reconstructed frequency resolved optical grating (FROG) trace and the intensity profile of the pulses (approx. 24 fs long) out of the amplifier [106].

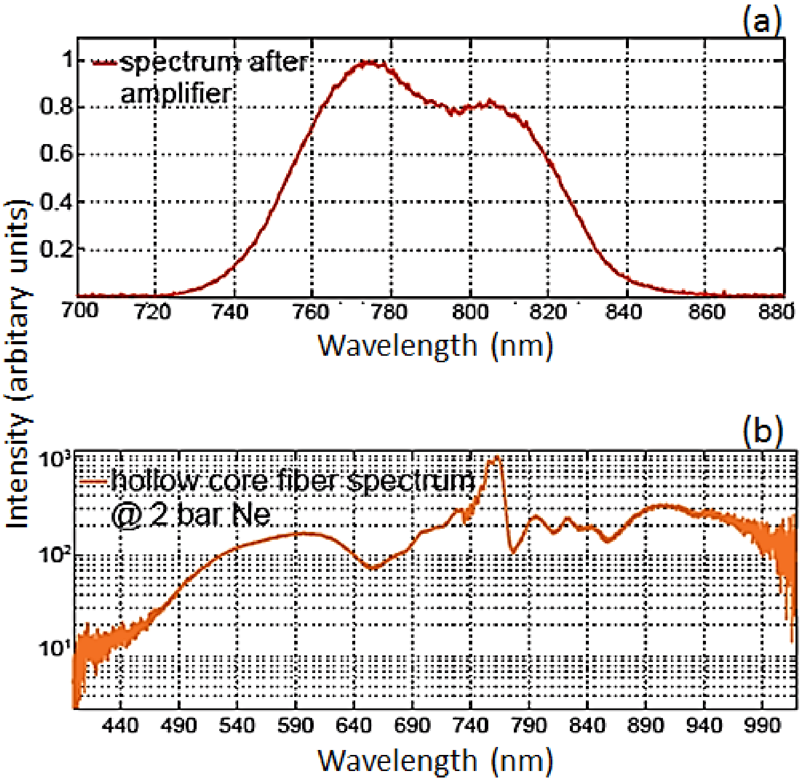

Figure 4.7: Spectrum of the laser beam (a) just after the amplifier (b) after passing through hollow core fiber filled with Neon gas at pressure of 2 bar

To increase the bandwidth, the amplified and compressed pulses are focused into a hollow core fused silica fiber (1 m long and 250 μm inner diameter) filled with Neon gas at $\sim$1.8 bar. Such an operation leads to the broadening of the spectrum due to self phase modulation [107–109]. The spectral range is almost doubled as shown in figure 4.7(b). See section A.2 for details on self phase modulation. On the output of the fiber, a thin pair of wedges at Brewster angle is placed to variably control the dispersion of the output pulse. This is followed by a set of chirped mirrors, where the laser beam makes multiple bounces to attain temporal compression of different frequency components in the beam. What one attains at the end is a phase-stable, broadband spectrum in visible/NIR range compressed to sub-4 fs time duration. The laser pulses were characterized with a dispersion-less transient grating FROG (TG-FROG) [110] as shown in figure 4.8 (c) - (d).

Most high field phenomena, like high harmonic generation (HHG) exhibit a strong CE phase dependence. To attain full control over the waveform of the electric field, in-

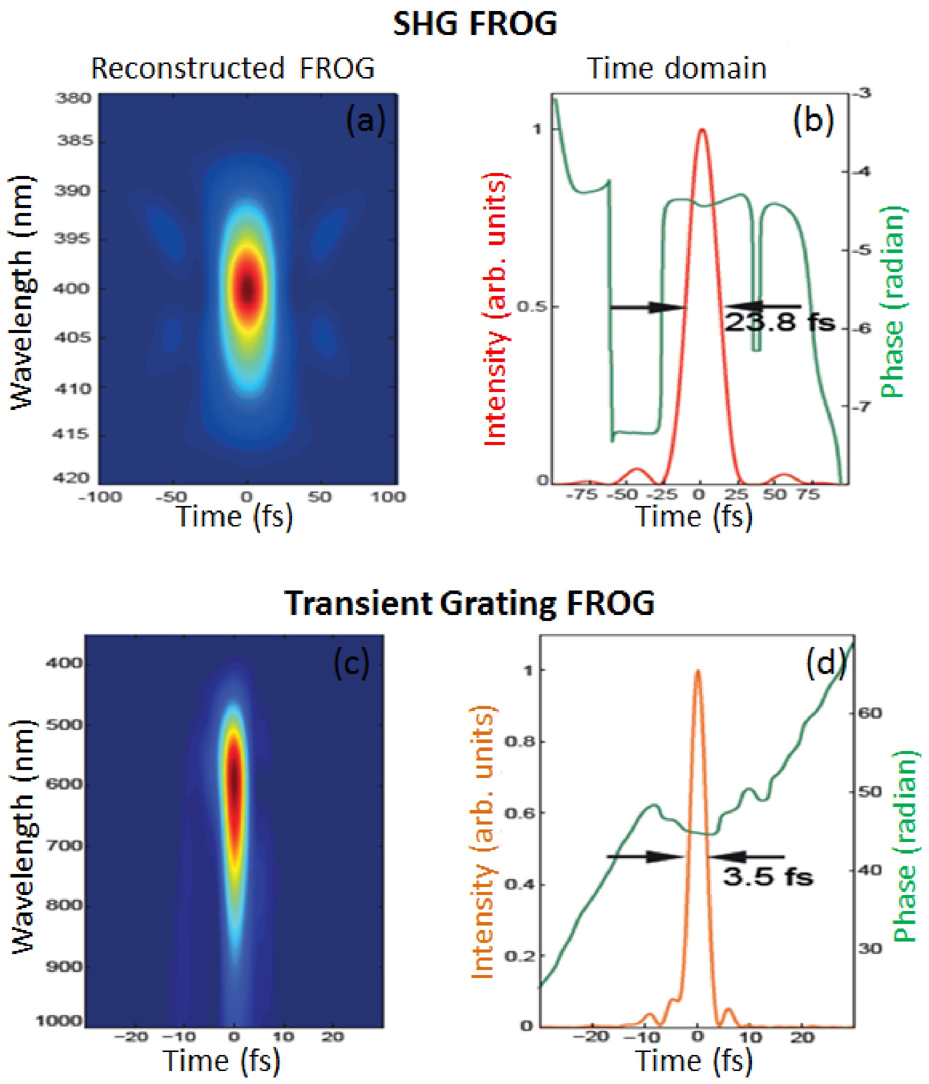

Figure 4.8: (a) The reconstructed FROG trace and equivalent autocorrelation time domain trace measured with Second harmonic FROG and Transient grating FROG

cluding the CE phase the oscillator is stabilized using nonlinear mixing techniques and a feedback loop. A second control loop corrects the phase drift due to the amplification process (f to 2f interferometer). A more detailed description of the phase stabilization can be found in reference [108]. This laser source represents a state of the art system for time-resolved spectroscopy with extreme time resolution, as presented in this chapter.

4.4 Pump-probe setup

The degenerate pump-probe setup used for the time resolved studies on manganite is shown in fig.4.9. The $\sim$ 4fs laser pulse beam generated from the amplifier laser system described above is split into two parts to be used as pump and probe beams. A half inch D-shaped mirror allows half of the beam to pass by as probe and the reflected half is used as pump. The optical spectroscopy setup has been designed to minimize dispersion. All the optical elements are used in reflection. A double periscope has been used for rotating the plane of polarization of the probe beam by an amount of 90 degrees. Such a choice is made to minimize interference between frequency-degenerate pump and probe pulses. The intensity in the probe beam is reduced using the reflection from a glass wedge. A concave mirror of focal length 200 mm is used for focusing both the beams on the sample inside a cryostat. The pump beam is incident normal to the surface of sample. The probe beam was spatially overlapped with the pump beam at an angle of about 1°. The non-collinear geometry is used to separate the probe beam from the pump beam but limit the temporal resolution of the experiment. For an angle of 1°, the decrease in the time resolution is less than the FWHM of the probe pulse and still in good range required for the experiment [1]. The pump beam has a spot size of 80 μm and the probe beam is 40 μm in diameter. On target, optimization of the signal has been done by adding or removing glass to the uncompressed pulses. We detect only a small section of the reflected spectrum since the integrated response over the complete CT band would lead to zero birefringence (see figure 4.3). And since the maximum change in the birefringence signal is around 2 eV, we cut the reflected probe in frequency range using low pass filter at 800 nm and a bandpass filter at 700 nm with bandwidth of 10 nm. Using a combination of a half wave plate and a wollaston prism, the probe beam components along each optical axis is channelized into two Silicon (Si) detectors. A balance detection scheme and lock-in detector (modulating the pump beam at half the laser repetition rate) has been used for acquiring the signal. For the experiment, $La_{0.5}Sr_{1.5}MnO_4$ sample was grown using floating zone technique and is cut along the ab plane.

---

[1] An angle of α (= 1°) between the pump and the probe beam limit the temporal resolution by t given as

$$tan(\alpha) = \frac{c * t}{D} \tag{4.1}$$

such that D is the spotsize of probe = 40 μm, c is velocity of light = 3 * 10^8 and α = angle of probe beam with the sample surface = 1°. The value of t comes out to be 2.3 fs.

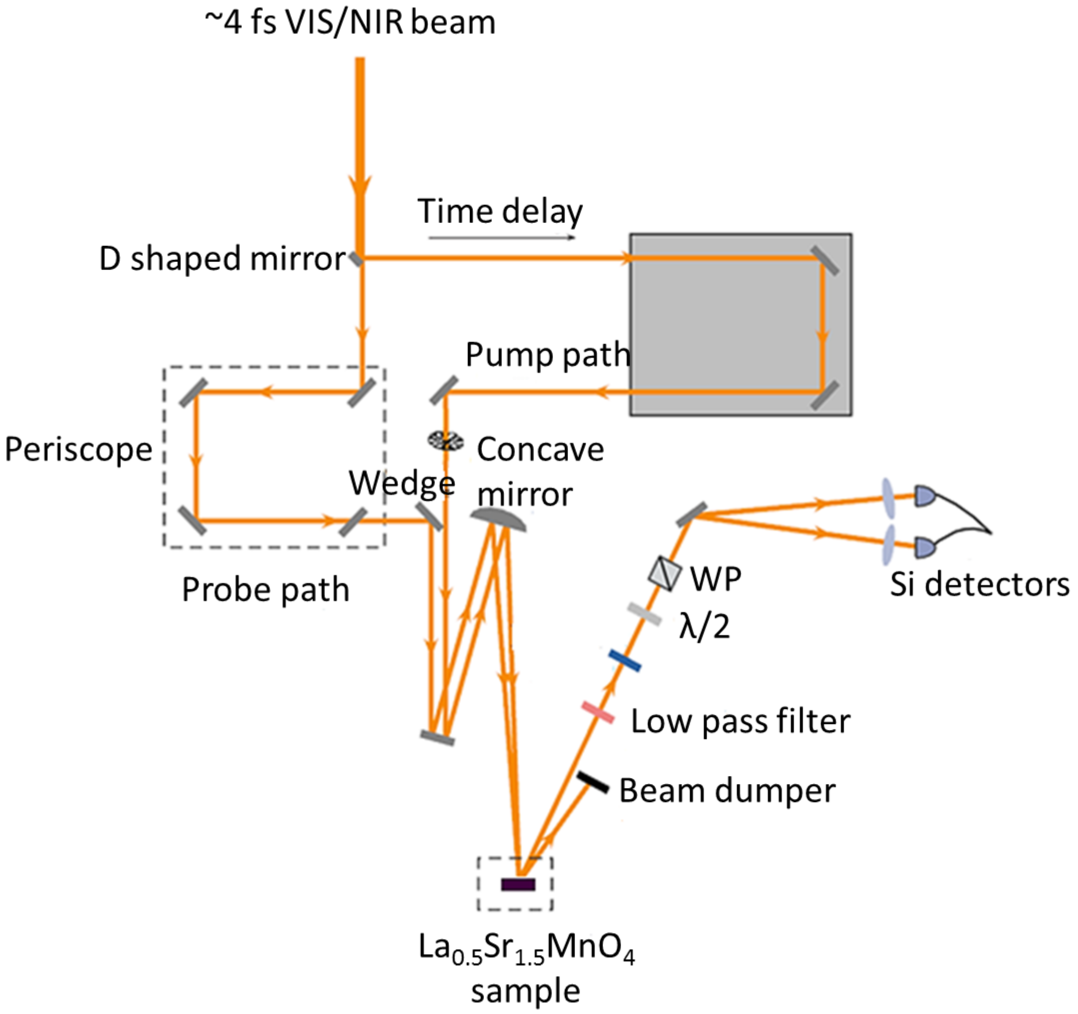

Figure 4.9: Degenerate pump-probe setup for $\sim$ 4fs VIS/NIR laser pulses. Abbreviations used are: Wollaston Prism (WP), Half wave plate ($\lambda/2$)

4.5 Structural bottleneck for melting of orbital order

We measure the change in birefringence (Δ B/B) which is nothing but the measure to the orbital ordering parameter. We resonantly excite the CT band of $La_{0.5}Sr_{1.5}MnO_4$ centered at 1.3 eV with our $\sim$ 4fs broadband pump laser pulses. The degenerated probe pulses measure the subsequent changes in birefringence across the complete CT band. But only a narrow spectral range of the reflected probe around 2 eV is collected into the detectors to have non-zero birefringence signal as explained earlier. The electron delocalization occurs at one of the Mn^{3+} site to the neighboring Mn^{4+} site occurs along the ferromagnetic chains in the MnO_2 plane (see figure 4.5). The response is probed at a small interval of two femtoseconds, to capture the fine details of the melting.

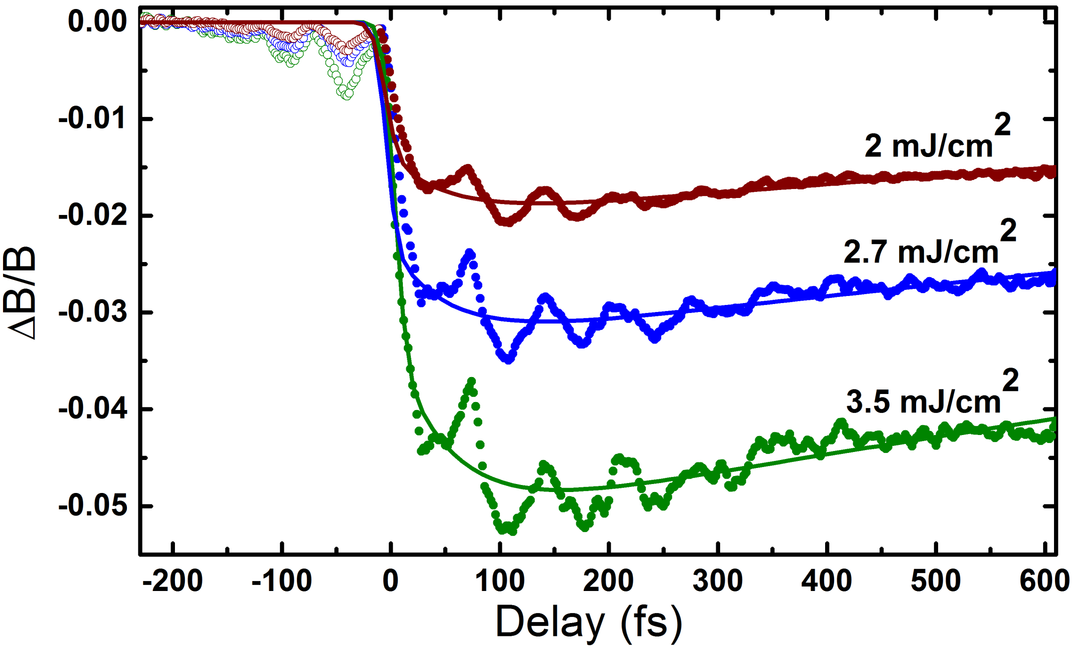

Figure 4.10: Change in birefringence in the MnO_2 plane of LSMO as a function of pump-probe time delay for three different pump fluence at a sample temperature of 20 K (filled and hollow circles). Solid lines are fit to the data as described in the text.

Figure 4.10 reports the photoinduced transient changes in birefringence in the ab plane of LSMO for different pump fluences at temperature of 20 K. For negative time delays (*i.e.* for the time when the pump beam comes after the probe beam), the flat baseline has low frequency oscillations at 17 THz on top. The zero background implies charge and orbitally ordered state persists when the system is yet not perturbed by the pump laser. These oscillations we observe are just an 'artifact' and results from perturbed free-induction decay (PFID) [2]. More importantly, optical birefringence drops down promptly at t= 0 followed by further decrease on the time scale of 100 fs. A change upto 5 % (for the maximum experimental pump fluence used) is observed. Ehrke et al. observe similar reduction, of the order less than 25 % for excitation fluence of 5 mJ/cm^2 in their measurements on the diffraction peak (1/4, 1/4, 0) associated to orbital ordered state [103]. In fact they observe a saturation behavior of the diffraction peak above 5 mJ/cm^2 [103].

---

[2] PFID occurs when the probe pulse precedes the pump pulse and the probe pulse duration is smaller than the dephasing time of the absorption band of the system. It does not tell anything about the time resolved dynamics of the system studied but reflects its spectral properties [111, 112]. PFID disappears as soon as pump and probe overlaps in time [111, 113] (see appendix A.3).

The excited system then partially relaxes to a long-lived state (4.10). An oscillatory response is also superimposed to the recoving state which exists for hundreds of femtosecond. The response of the system is well fitted using an error function for the falling edge and a double exponential function of the form (1-A*exp$^{-t/\tau_1}$) * exp$^{t/\tau_2}$ for the decay. The fit for each fluence curve is shown in thin colored lines in the figure 4.10. For the curve at fluence = 2.7 mJ/cm^2, the first decay time constant τ_1 = 53 fs is obtained and corresponds to the direct electronic relaxations. It is followed by a slow decay channel with time constant of τ_2 = 2-3 ps which occurs due to electron-phonon thermalisation. The birefringence curves for other fluence give similar decay constants.

To analyse the oscillatory behaviour, we extract the oscillations by substracting the fit function from the measured birefringence data. The same is plotted for fluence = 2.7 mJ/cm^2 data in figure 4.11 together with its Fourier transform which shows a sharp peak at 14.7 THz. This coherent oscillation corresponds to the in-plane B_{1g} Jahn-Teller mode of oxygen octahedral at 14.7 THz. The observed oscillating frequency is in close agreement to the continous -wave Raman scattering measurements (which is one of the most powerful technique to probe the structural changes) [114]. A convincing determination of this mode requires time resolutions well below T_{JT} /4 = 15-18 fs [77, 114]. Our optical pulses of approximately 4 fs duration makes it possible to clock the orbital melting transition down to a fraction of the Jahn Teller distortion time.

To have insight into the early time dynamics of the melting, we show a zoom-in of the birefringence signal ΔB/B at pump fluence of 2.7 mJ/cm^2 for the first 50 fs after photoexcitation (see figure 4.12). The circles show the experimental data (filled and hollow blue circles for positive and negative pump-probe delay time respectively) together with the fit in thin blue line. An intensity profile of the $\sim$4 fs obtained using a transient grating FROG is shown in dashed black line together with its temporal integral (red solid line). Clearly, the loss of optical birefringence occurs on a time scale significantly longer than the excitation pulse or its time integral. The error function fit (blue solid line) quantifies the drop time of 18 fs which is significantly higher compared to $\sim$ 4 fs electronic perturbation. Our experimental finding indicates that the melting is limited by structural bottleneck and not by the pulse duration.

Notably, this 18 fs bottleneck is approximately one-fourth of the time period (= 68 fs) of the JT mode observed at 14.7 THz. The prompt step of reduction is the first quarter of the oscillation cycle hinting towards the involment of lattice as the principle force towards early melting. Very recently, similar studies were made on the orbital ordering in manganite $Pr_{0.5}Ca_{0.5}MnO_4$ [115]. The CT band was optically excited with 800nm pulses and changes in the structural parameters are measured using 50 fs long high X-ray flux beam from a free-electron laser. They suggest that the transition of charges across the ferromagnetic chain release the forces that was stabilizing the JT

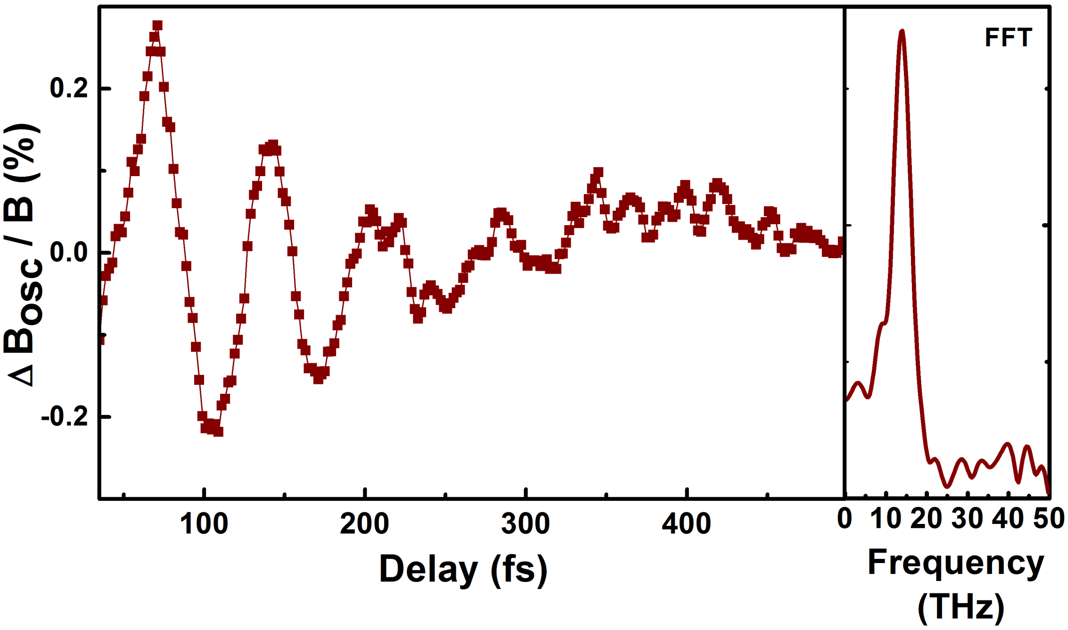

Figure 4.11: Oscillations extracted from the time profile of ΔB/B for positive time delays, shown in the inset, together with its Fourier transformation.

distortions. The unstabilized JTD via its coupling to other vibrational modes, triggers a chain reaction leading to reorganization of the atoms in the unit cell. They claim that the electronic excitations are responsible for the lattice dynamics [115]. However, the experiment does not carry any information on the early dynamics of the melting of CO/OO owing to its low temporal resolution of 50 fs. On the contrary, our optical birefringence experiment suggest that primary role of the lattice over the electronic interactions towards the melting of the CO/OO state.

To understand the role of pump fluence on the orbital dynamics, we plot both the peak amplitude of the photoinduced birefringence (see figure 4.13(a)) and the coherent B_{1g} phonon amplitude (see figure 4.13(b)) as a function of pump fluence. Their amplitudes shows similar linear scaling with the fluence and with similar threshold value of about 1 mJ / cm^2. Threshold behaviour is a general characteristic of light-induced phase transitions [116]. However, typically coherent phonons scale linearly with excitation light intensity without any threshold. They are generally excited by the conventional impulsive Raman mechanism [117, 118]. The impulsive Raman excitation occurs when the exciting pulse duration is shorter than the Raman active vibrational mode period. In the present case also, the exciting pulse duration of $\sim$ 4fs is only a

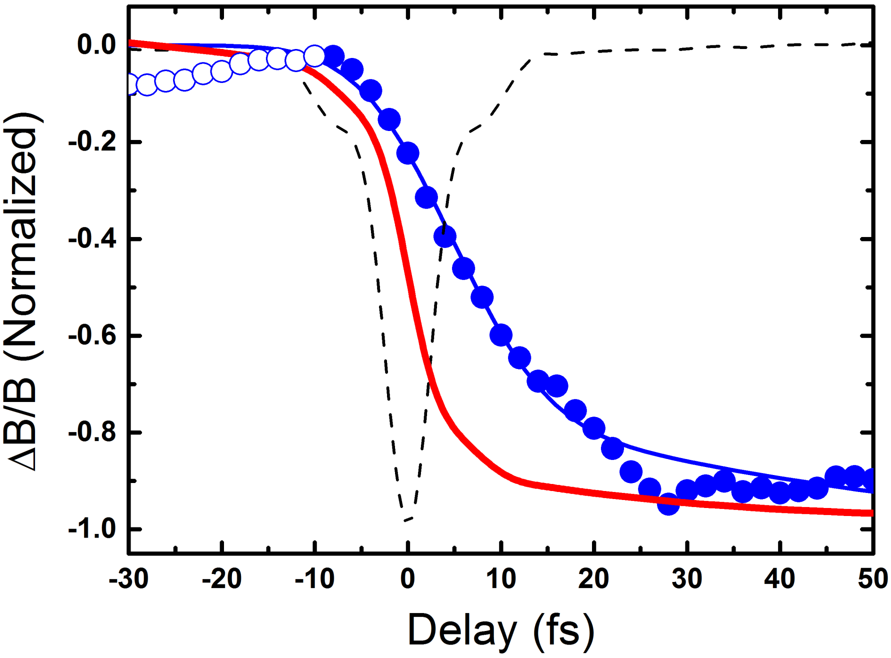

Figure 4.12: Zoom in of figure4.10 into the rising edge of the birefringence signal intensity at a pump fluence of 2.7 mJ/cm^2. The blue solid line shows an error function fit to the rising curve. The red line shows the intensity profile of ~4 fs laser pulse, together with its temporal integral in solid.

fraction of the JT mode time period (68 - 70 fs).

Still, we observe a threshold in the fluence-dependent coherent phonon amplitudes. Such a behaviour can be explained in the light of the assumption that the coherent motion at 14.7 THz is induced by a cooperative lattice-orbital response. This would require a certain minimum photodoping level to begin the coherent motion. Such an observation substantiates our claim that the lattice is triggering the CO/OO in $La_{0.5}Sr_{1.5}MnO_4$.

In a nutshell, this experiment shows three major outcomes. Firstly, the 18 fs bottleneck time scale for the melting of the orbital order is far way slower that the impulsive exciting pulse of ∼ 4fs. Secondly, Jahn-Teller mode with a period of 70 fs is observed which is approximately one-fourth of the bottleneck. This correlation strongly emphasizes the fact that the melting of orbital order occurs along the line of the coherent Jahn-Teller motion. Thirdly, the occurrence of very similar threshold features in the melting of OO state and the motion of the lattice mode strongly hints towards the cooperativity of lattice involved in the phononic motion.

We conclude that the orbital ordering in $La_{0.5}Sr_{1.5}MnO_4$ is likely to be stablized by

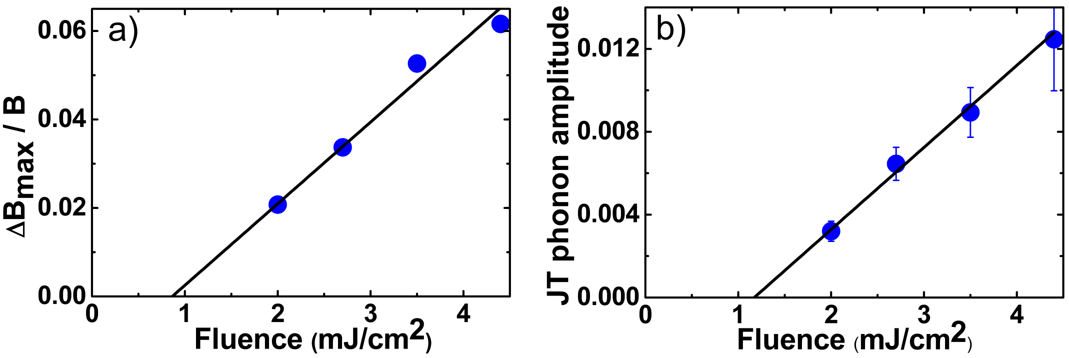

Figure 4.13: (a) Amplitude of the transient birefringence and (b) coherent phonon oscilations as a function of pump fluence. Solid black lines are linear fits to the data.

structrual distortions instead of electronic interactions.

4.6 Summary

We used sufficiently short optical pulses that can trigger the electronic transfer faster than all lattice vibrations. All experiments so far have used longer pulses, insufficient to separate fast electronic excitation from slow lattice dynamics.

We used sub-4 fs laser pulses to study the photo-induced melting of the charge/orbital ordered manganite $La_{0.5}Sr_{1.5}MnO_4$. We find that the time required for the phase transition has a structural bottleneck and is accompained by coherent 14.7 THz oscillations, significantly with a time period fourfold to the melting time of birefringence. In addition, we find that the photo-induced amplitude changes in birefringence and in the high frequency oscillations exhibit similar linear growth with fluence with a threshold of $\sim$1 mJ/cm^2, indicating a non conventional mechanism behind the coherent phonon generation. The coherent phonon is likely triggered by the cooperativity of lattice-orbital response. Our experiments strongly suggest that the orbital order is stabilized via structural effects.

5 One dimensional correlated systems

5.1 The physics of 1D Mott insulators

The properties of one dimensional systems are elementary very different from the analogous 2D and 3D systems. The influence and effect of quantum fluctuations become enhanced in low dimensional solids. The Fermi liquid theory of interacting electrons, relevant to 2D and 3D, gets replaced by the Luttinger liquid theory in 1D [119, 120]. Figure 5.1 shows the qualitative difference between the two. The quantum confinement of electron motion is enhanced in low dimensions. In 2D and 3D scenario, an electron can move independently of others in contrast to 1D framework, whereas in the latter, majorly the collective movement exists [121]. One of the main consequences of this collective behaviour is spin-charge separation in 1D. In ordinary Fermi liquids, the quasiparticle carries together both the spin and the charge information of the electron. But for 1D systems, there are two independent quasiparticles to describe an electron: the 'spinon', carrying information on the spin and the 'holon' carrying information on the charge [120]. This outlandish phenomena was predicted more than four decades ago [122] and was recently experimentally demonstrated on the quasi-1D organic conductor TTF-TCNQ via angle-resolved photoemission [123]. Also, in $SrCuO_2$, signatures of spin-charge separation were observed [124], a system which also show large

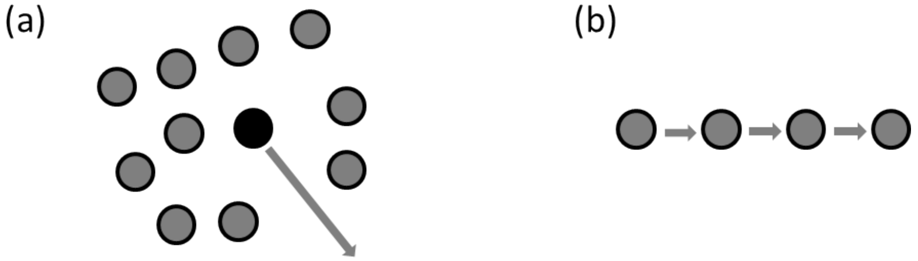

Figure 5.1: Cartoon depicting that (a) in 2D and 3D systems, the electron movement in space is possible between the others (b) whereas in 1D, only collective excitations are possible [Adapted from [121]].

non-linear behaviour under electric field thereby serving as a promising candidate for optical switches [125].

Another consequence of the collective behaviour in 1D is that the quantum effects are prominent. The electronic bandwidth W=2zt (z is nearest neighbour number) is strongly reduced because z goes down in 1D systems. This enhances the relative role of Coulomb interactions [121]. Consequently 1D systems provide an opportunity to study Mott physics which is of great relevance in today's research in condensed materials.

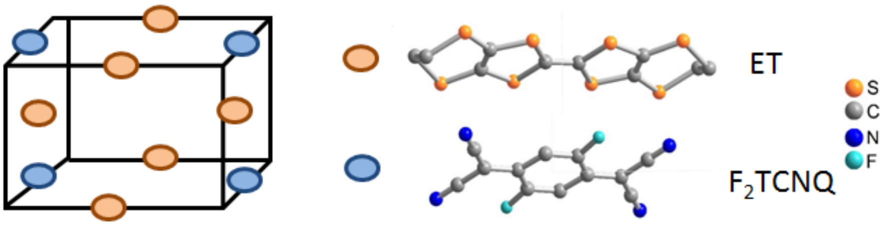

Figure 5.2: Structure of an organic molecular crystal ET-F_2TCNQ

Our system of interest are one-dimensional organic molecular compounds. The organic molecular compounds offer highly tunable electronic correlation properties in all dimensionalities because the molecular structure allow to tune interaction parameter via the overlap between the molecular orbitals (along various crystal axis) and via the tilt of the individual molecules at their lattice positions. And having them in low dimensions enhance the Mott physics. A unit structure of such a 1D molecular organics ET-F_2TCNQ is shown in figure 5.2. Unlike the usual crystalline structure comprising of the atoms in the unit cell held together by covalent or ionic bonds, in the molecular crystal ET-F_2TCNQ, the ET and F_2TCNQ molecules (blue and orange circles in figure 5.2) are far apart from each other held together by weak van der Waals forces [25]. The lattice spacing allows tuning the overlap integral giving rise to difference states of high or low conductivity. The effective interactions of U/t and V/t in such molecular crystals can be tailored by two means: (1) Applying chemical pressure via changing the anions like AsF_6, PF_6 etc. (see figure 5.3). This is readily possible because of the availability of variety of molecules, easily substitutable in the synthesis process [16]. (2) Because of the weak bonds between the molecules, external pressure can comfortably tune the lattice spacing. By both the means, the structural arrangement of the crystal is tuned thereby modifying the lattice spacing, bond angles and effective orbital overlap which in turn influence the interaction strength [17]. Figure 5.3 underscores this feature of large tunablity of interactions and hence phases, in quasi-1D organic compounds as a function of molecular replacement, external pressure and temperature. The arrows indicate the behaviour of the respective compounds at ambient pressure. Tetrathiofulvalene-tetracyanoquinomethane (TTF-TCNQ) and tetramethyltetraselenafulvalene (TMTSF) salts were among the first organic compound observed to exhibit one-dimensional conductivity at low temperatures.

In the next section, we present a prototypical quasi-1D organic molecular solid ET-F_2TCNQ, investigated in this thesis, being a very simple and therefore a clean representation of a solid state 1D Mott insulator. The compound is a charge-transfer complex comprising of two kind of molecules ET and F_2TCNQ, where one molecule acts as an electron donor and other molecule acts as an acceptor. There are two kinds of charge transfer in this solid, the donor-acceptor *i.e.* from ET to F_2TCNQ and the Mott transition from ET$^+$ to ET$^+$. Its crystal structure and the main optical properties are discussed, followed by photo-induced modulation of the effective interactions.

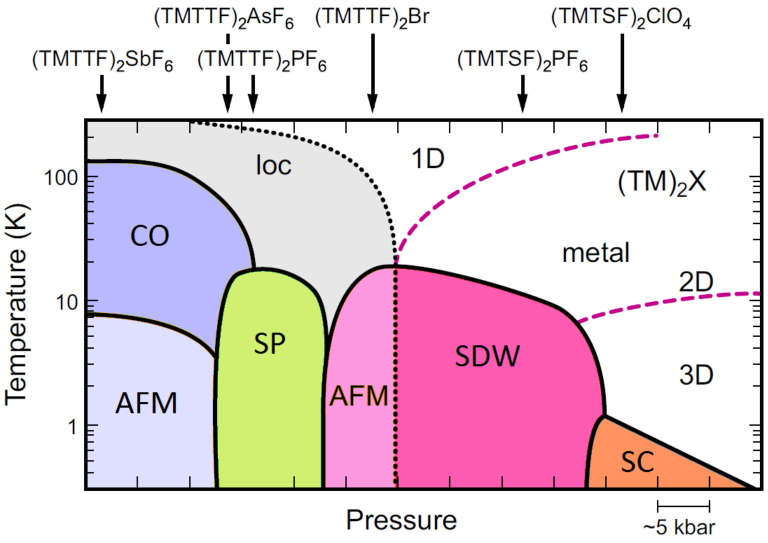

Figure 5.3: The phase diagram of the quasi-1D compounds TMTTF and TMTSF. Abbreviations are antiferromagnetic (AFM), charge ordered (CO), spin Peierls (SP), spin density wave (SDW), superconductor (SC), localization (loc) [Adapted from [126, 127]].

5.2 ET-F_2TCNQ, a prototypical 1D system

5.2.1 Crystal structure

Bis - (ethylendithyo) - tetrathiafulvalenedifluorotetracyano - quinodimethane (ET - F_2TCNQ) is a quasi-1D charge transfer solid. It has a monoclinic P2/m structure with lattice constants, a = 5.791 Å, b = 8.210 Å, c = 25.100 Åand Volume = 1186.34 Å^3. The

ET and F_2TCNQ molecules are present in mixed-stack columns facing each other along *b*-axis as shown in figure 5.4 (a). Their structure is characterized by three main features:

- An electron from a ET molecule transfers to the neighbouring F_2TCNQ molecule, making it a charge transfer crystal [128]. The charge transfer between the donor and the acceptor site is complete, experimentally disclosed by the measure of $C = C$ double bond length in the ET molecule [129]. Owing to donor-acceptor charge transfer, the ET molecules are half-filled.
- Compared to other mixed stack organic salts, the intermolecular distance between the donor and the acceptor site along *b*-axis (figure 5.4(a)) is large. There is no direct overlap of their π-orbitals. The structure and the tilt of the molecules is such that the ET-ET overlap is preferred compared to overlap.
- The intermolecular distance between the ET molecules lined up along *a*-axis is smaller than two times of the van der Waals radius. The large overlap between their π-orbitals makes side by side interactions possible. This gives them quasi-1D electronic properties as discussed in the next subsection.

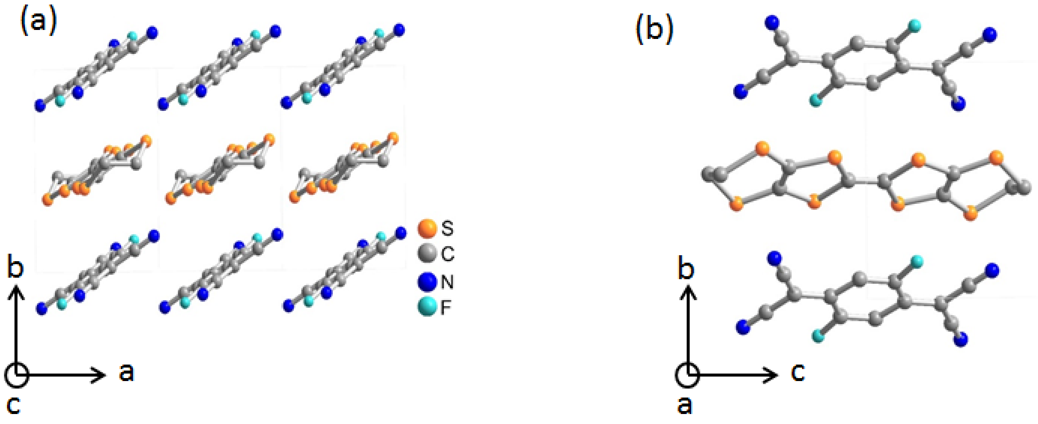

Figure 5.4: (a) Crystal structure of ET-F_2TCNQ (b) Molecular structure of individual molecule along c-axis

Figure 5.4 (b) shows the spread structure of individual molecule along *c*-axis [130]. The structure associated to the molecule give it additional on-site degree of freedom. Other significant characteristics of this organic salt is its weak electron-lattice interactions, evident from the lack of Peierls distortion even at low temperatures [1] and significant coupling of the local electron density to molecular vibrations.

---

[1] Peierls distortion refers to the lattice dimerization, resulting in band gap opening at Fermi surface, even in the absence of correlations [131].

5.2.2 Optical properties

Quasi-one dimensionality of the compound is evident from its optical response. Figure 5.5 shows the optical reflectivity spectrum of ET-F_2TCNQ along all the three directions. Strikingly, along the *a*-axis (figure 5.5 (b)), there is a distinct absorption band, centered around 5500 cm^{-1}. This feature corresponds to the transfer of charge from one ET molecule to neighbouring ET molecule *i.e.* $ET^{+}ET^{+} \rightarrow ET^{0}ET^{2+}$ and referred as charge transfer (CT) resonance. The on-site effective correlation U/t at the ET site is high, preventing the hopping of electron. Hence the the charge-transfer peak occurs at such high energy. In the DOS, this corresponds to split of the quasi-particle peak at the Fermi-energy into LHB and UHB. Transition from the LHB to the UHB give rise to Mott gap, or the so-called charge transfer peak for this case in the optical reflectivity (see figure 2.6). ET-F_2TCNQ has characteristic small intersite tunneling t $\sim$ 40 meV and large Coulomb repulsion U $\sim$ 840 meV [19, 53]. The value of these parameters are extracted by fitting the CT peak (in equilibrium) with a model based on the extended Hubbard model. This is discussed in detail in section 5.2.3. The strong electronic interactions U/t $\sim$ 20 make the material a strong Mott insulator even at room temperature. Along *b*-axis, the spectrum is mostly featureless (figure 5.5 (a)) as there is no inter- or intra-molecular transition process owing to negligible overlap between the molecule along this direction. Only few molecular vibrations modes are present in the low energy mid-infrared frequency range. Along c-axis, the features around 10000 cm^{-1} and 25000 cm^{-1} in the optical reflectivity (figure 5.5 (c)) belong to intra-molecular transition of ET and F_2TCNQ. Summarizing, the sharp spectral feature along *a*-axis indicates the strong 1D nature of ET-F_2TCNQ.

Additionally, there are many lattice and molecular phonon modes at low frequencies, as shown in figure 5.5 (e). Notably, the local molecular modes are different from the lattice phonons. Whereas the phonon mode refers to the collective displacement of the lattice involving changes in the distance between the nearest neighbours atoms, the local molecular modes represent the local motion of the molecule at its site, changing only the intra-atomic distances of the molecule and without disturbing the structure of the lattice [129]. Another point to note that in ET-F_2TCNQ, the lattice modes do not couple significantly to electronic degrees of freedom owing to weak electron-lattice interactions in this compound. However molecular modes are likely to couple strongly, as we shall show shortly. There are various molecular modes which are likely to couple strongly to charge [132]. In particular, the modes which involves motion of $C = C$ bond and $C - S$ bond etc. since the charge densities are high there. The mode at 1000 cm^{-1} (30 THz) shown in blue is also a 'charge coupled molecular mode'. It is an infrared active, ring deformation mode, linked with the vibration of the ET molecule parallel to the a-axis and it is accessible with our available laser setup. Later in the chapter, we discuss the dynamical coupling of this mode to the electronic degrees of freedom, and thereby changing the effective Mottness.

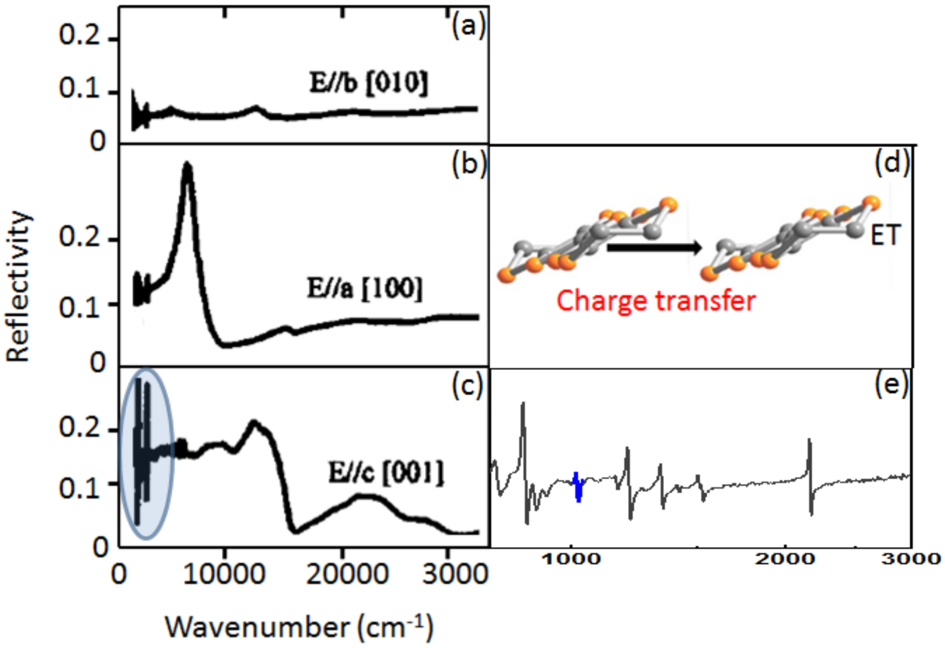

Figure 5.5: (a) - (c) Optical reflectivity spectrum of ET-F_2TCNQ parallel to the b-axis, a-axis and c-axis respectively [Adapted from [130]], (d) Sketch of charge transfer along a-axis between neighbouring ET molecules (e) zoom in of reflectivity along c-axis, in the low frequency range, with a mode near 1000 cm^{-1} shown in blue.

Steady state optical conductivity σ (ω): The optical conductivity can be extracted from the reflectivity curve. Normal-incidence reflectivity is a non-linear function of the microscopic response function of the material *i.e.* the dielectric constants. The frequency dependent reflectivity at certain frequency ω is related to the complex dielectric function $\epsilon_r(\omega)$ by the Fresnel formula given as,

$$R(\omega) = \left| \frac{1 - \sqrt{\epsilon_r(\omega)}}{1 + \sqrt{\epsilon_r(\omega)}} \right|^2 \tag{5.1}$$

The real and imaginary part of the conductivity can be extracted using Kramer-Kroning transformations [49]. The optical conductivity of ET-F_2TCNQ $\sigma_1(\omega)$ extracted from the reflectivity for light polarized along a-axis at ambient temperature and pressure is shown in green in figure 5.6 (b). It exhibits a fully established Mott gap of 700 meV and a narrow bandwidth of 100 meV. Transition over the gap in the real space, leaves a hole behind at the ET site (called holon) and creates a doubly occupied electron site at the neighbouring ET site (called doublon). There is no Drude peak in the σ_1 in agreement with the negligible d.c. conductivity (less than $10^{-5}\omega^{-1}\mathrm{cm}^{-1}$) observed in transport measurements of the Mott insulating state at room temperature [130].

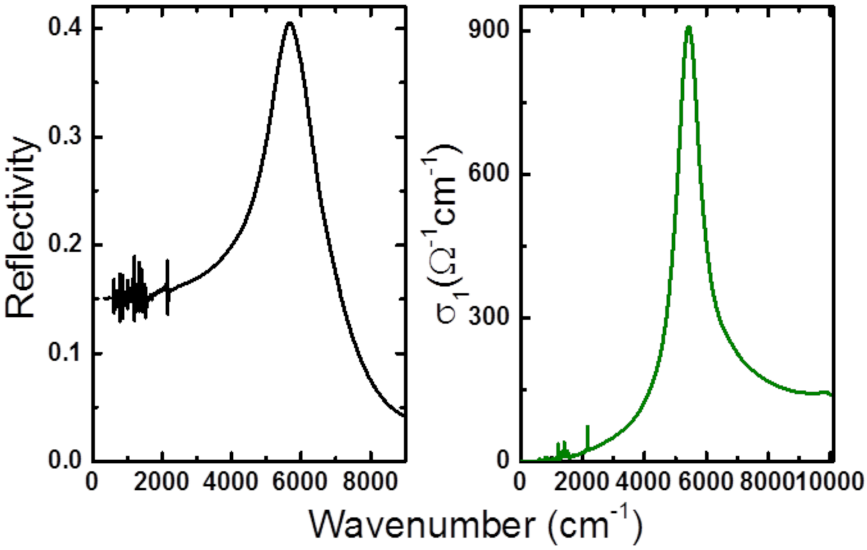

Figure 5.6: Static optical reflectivity and conductivity of ET-F_2TCNQ at room temperature along a-axis.

5.2.3 Fit to the steady state optical conductivity

Common practise in interpreting optical conductivity is to apply Drude-Lorentz model that is based on the harmonic oscillators. But in this case, since we are in 1D and the system is almost ideal, we can model the optical properties with the analytical response of the extended Hubbard model [49, 133]. In the limit of finite nearest-neighbour Coulomb repulsion V and hopping amplitude t << U, the extended Hubbard model can be analyzed in 1/U expansion term. We restrict our analysis to the case where in the ground state, all the sites are singly occupied and in the excited state, the number of doublons are conserved. To include the spin contribution in the optical conductivity, we add spin correlation constant g_q at quasi-q momentum [134] [2].The optical response after the spin integration is dictated by charges through current-current correlation

---

[2] In the "no-recoil approximation", the main contributions to the conductivity comes from transitions between parallel bands *i.e.* at q = 0 (LHB (k) $\rightarrow$ UHB(k)) and from transitions between anti-parallel bands *i.e.* q = π (LHB (k) $\rightarrow$ UHB(k+π)) [135] ,where $g_0 = 2.65$ and $g_\pi = 0.05$. Their values were calculated from DMRG simulations [136, 137].

function $c_{jj}(\omega)$. The reduced optical conductivity is related to this function as follows [135].

$$\omega\sigma_1 = \mathrm{Im}\left\{c_{jj}(\omega)\right\} \tag{5.2}$$

The complete reduced optical conductivity can hence be written in the analytical form as following [19]

$$\begin{aligned}\omega\sigma_1(\omega) = {} & \pi g_\pi t^2 e^2 \delta(\omega - \omega_2) + \\ & g_0 t^2 e^2 \left[\theta(V - 2t)\pi(1 - \frac{4t^2}{V^2})\delta(\omega - \omega_1) + \theta(4t - \omega - U)\frac{2t\sqrt{1 - (\omega - \frac{U}{4t})^2}}{V(\omega - \omega_1)}\right]\end{aligned} \tag{5.3}$$

Here θ is the Heaviside function, ω_1 = U - V - $4t^2$/V and ω_2 = U-V. The main contribution [19, 135, 138] to the optical conductivity is represented by a delta peak at ω_1 corresponding to a Mott-Hubbard exciton. The peak is centered at energy ω_1 and accounts for bound holon-doublon (HD) pair. Bound HD represents the configuration when the holon and the doublon site are next to each other (see the sketch in figure 5.7.). Importantly, the δ peak is multiplied to a heaviside step function θ(V - 2t), to account for the fact that the bound HD pair exists only for V $>$ 2t. The last term in eq. 5.3 with heaviside function, represents a semi-elliptic contribution coming from the unbound holon and doublon called particle-hole continuum (see the sketch in figure 5.7) [19, 53]. It is a broad feature and exists for $\mid \omega$-U $\mid \leq$ 4t. The sharp features coming from δ and θ functions have been convolved to a Lorentizian of width $\eta_1 \sim$ 2t for HD configuration and η_2 for PH continuum. This is to include their broadening caused by other degrees of freedom, not accounted for the extended Hubbard model. In particular, since the number of holon-doublon pairs is assumed to be a constant of motion in the excited state, the approximation does not account for electronic processes which cause their recombination. Additionally it also neglects their coupling to lattice vibration which will also result in them having a finite lifetime, broadening their δ peak. A Lorentzian oscillator at 14000 cm^{-1} is added to the model fit to consider the background coming from the high energy inter-molecular transitions. The theortical model provides a good fit (dashed black) to the experimental conductivity (green curve) as shown in fig.5.7. Both the exciton peak and partice-hole continuum contributions are shown in red and blue curves in figure 5.7. The additional second negligible contribution to the optical conductivity coming from the second δ peak centered at ω_2 can be ignored in the analysis because of the small value of g_π (= 0.05). From the model fit, we henceforth deduce the values of U ($\sim$ 840 meV), t ($\sim$ 40 meV) and V ($\sim$ 100 meV) with η_1 = 85 meV and η_2 = 175 meV for ET-F_2TCNQ.

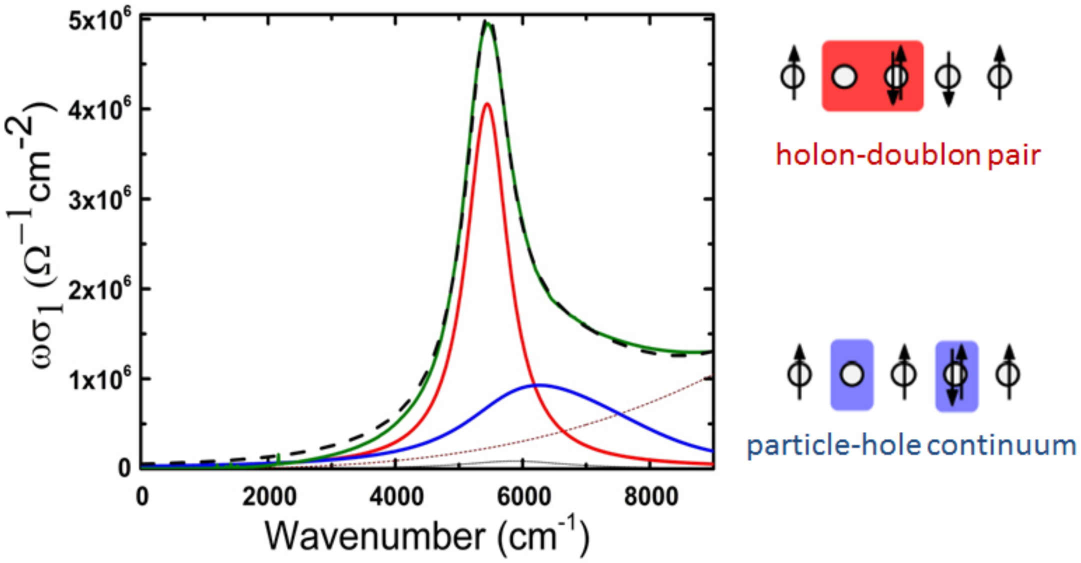

Figure 5.7: Reduced optical conductivity (green line) at ambient temperatuer and pressure, together with fit in dashed black. Red and blue curves are contribution from holon-doublon pair and particle hole continuum respectively. Dashed brown is a background Lorentzian oscillator at 14000 cm^{-1}. On the right panel, top is the sketch of holon-doublon pair and bottom is the typical particle-hole continuum.

5.3 Optical excitonic states in a 1D Mott insulator

The dynamical studies on 1D Mott insulator is of interest both from experimental and theoretical point of view. It provides the opportunity to study and understand genuine many-body physics in a real solid state system with rather simple theoretical models owing to the reduced configurations in one-dimension. Here we discuss the the theoritical picture of the states that can be formed via optical excitation across the CT resonance of a half-filled Mott insulator. Figure 5.8 shows the different possible excited states calculated using density-matrix renormalization group (DMRG) method. The ground state correlation parameters defines the ground state of the system: Mott insulating state or charge density wave (CDW) state. For high U/t and low V/t (as in our case of ET-F$_2$TCNQ), a Mott insulating ground state is formed clearly owing to strong on-site Coulomb repulsions. As V/t is increased, strong interactions to the neighboring site drags back the doublon near to the holon forming adjacent and pinned HD pairs, which overall forms long ranged charge ordering *i.e.* a CDW state [136] (see CDW in figure 5.8) . The solid line in the figure shows the separation of the two ground states.

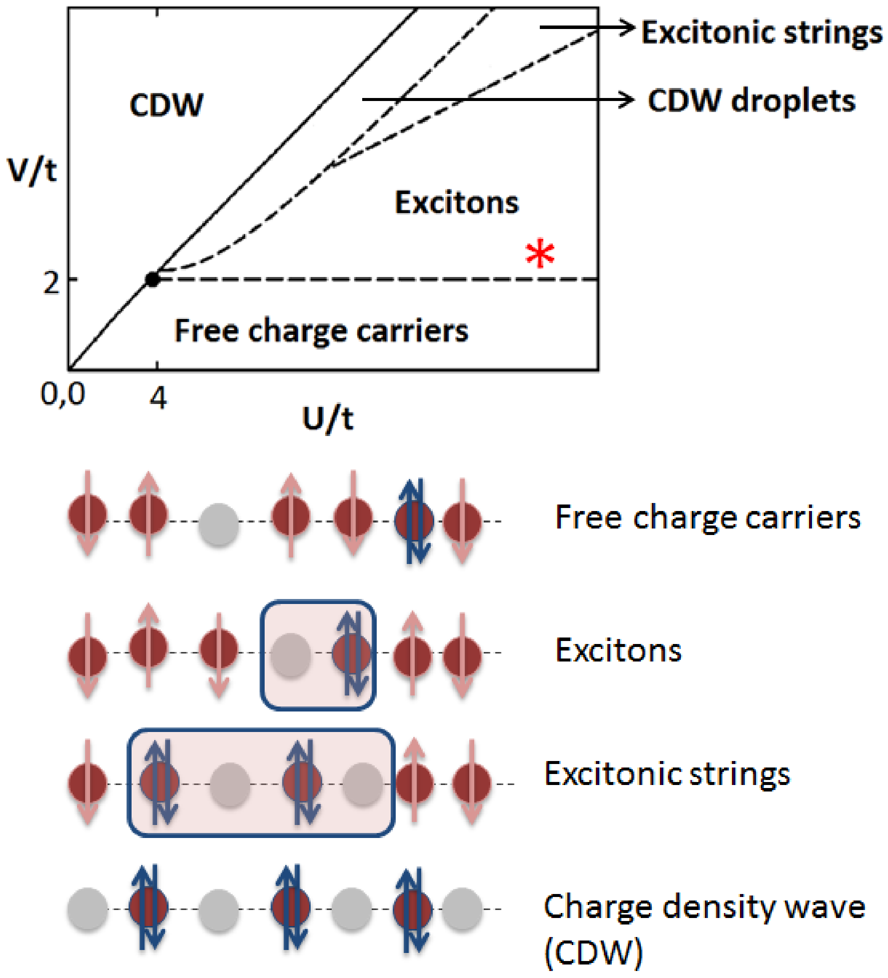

Figure 5.8: Optical excitation pathway as a function of correlation parameter U, t and V of the system [Adapted from [138]].

On optical excitation, for the system with $V \leq 2t$ and moderate U/t, the holons and the doublons are free to move and constitute free charge carrier metallic state. As V/t is increased, they start to bind to each other owing to more binding energy V compared to the kinetic enegy t. A sharp transition to bound HD pair called exciton occurs at V = 2t. Keeping U constant and further increasing V/t, the system falls into formation of multiple bound holon-doublon pairs called the excitionic string and lead the system towards the extreme case of long range bound HD *i.e.* CDW formation.

Our model system of ET-F$_2$TCNQ with large $U/t \sim 20$ and $V/t \sim 2.5$, falls in the Mott state (shown by star in figure 5.8)and suggests that excitons can be created upon optical excitation.

5.4 Photo-excitation of the Mott gap

The photo-excitation in 1D correlated solids are important both from experimental and theoretical point of view. The various phases in the rich phase diagram of the 1D correlated systems are particularly unstable near the crossovers. A tiny optical perturbation can change the electronic properties dramatically. The various analytical and numerical methods (like time-dependent Density-Matrix Renormalization Group) available are indispensable to our understanding about non-equilibrium dynamics in these low dimensional solids dominated by correlations [121, 135]. The photo-induced phase transitions have been studied in various 1D Mott insulators like halogen-bridged Ni halides, TCNQ salts, ET-F_2TCNQ [139–141]. Their dynamical study underpin the physics of electron localization, delocalization and electron-hole asymmetry. Some of the first pioneering dynamical studies are indroducd in this section.

Iwai et al. were the first to observe the photo-induced Mott transition in a 1D correlated system of Br-bridged Ni-chain. The response to the photo-doping across the Mott gap in Br-bridged Ni-chain is found to be dependent on the photodoping concentration. At low photon density, the spectral weight from the CT excitation at 1.2 eV is transferred to the low energy excitations below 0.5 eV. The newly created absorption band in the in-gap region is termed as midgap absorption band. However, at high pump fluence, transition from insulator to metallic state is observed [139]. The experiment has two main conclusions: First, that the electron carriers are responsible for the photoinduced phase transition since a similar weak midgap absorption at approximately same energy position is also observed in the case of small number of electron carriers doped during sample synthesis. Secondly, the electon carriers are localized by the presence of lattice modes at low phonon concentrations. Other 1D systems such as Sr_2CuO_3 and K-TCNQ equipped with electron-phonon coupling (and Peierls distortion) show similar midgap absorptions [142].

Remarkably, our model system ET-F_2TCNQ has a unique arrangement of the molecules such that both the electron-lattice and spin-lattice interactions are negligible. Hence, the consequences of photodoping on half-filled ET-F_2TCNQ can be expected to be different to the 1D system described above which suffer from Peierls distortions. ET-F_2TCNQ acts as a perfect testbed to the study of bare electronic excitations in the Mott insulating state. We will next discuss the photo-induced melting of Mott gap in the model system.

Okamoto et al. were the first one to demonstrate photo-doped I-M transtion in ET-F_2TCNQ [143]. On photo-excitation of CT band, the spectral weight is transferred from the CT excitation to the Drude component (around $\omega = 0$) with no mid gap band formation for all doping concentrations measured [143]. By pumping above the Mott

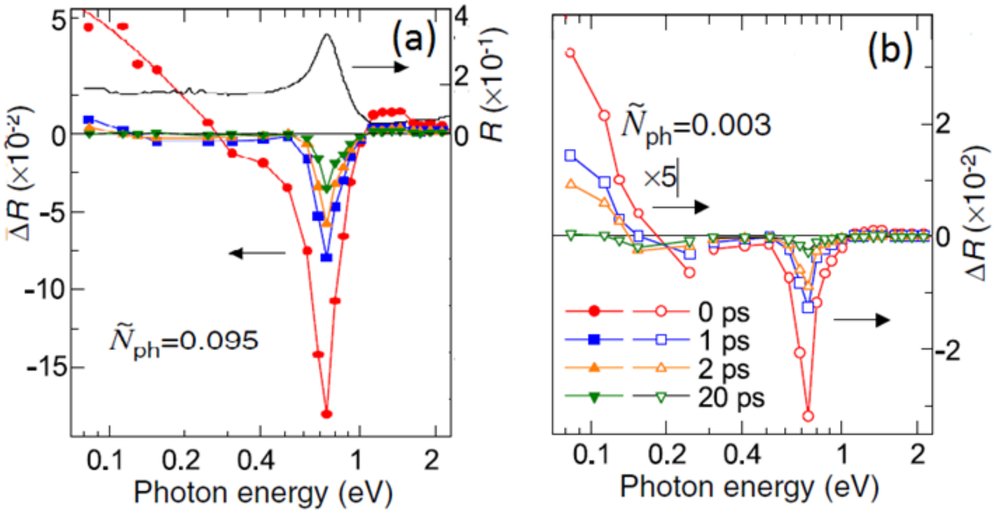

Figure 5.9: The static optical reflectivity of ET-F_2TCNQis shown as black line. The colored lines show photo-doped spectral changes in reflectivity at various time delays at (a) high fluence and (b) low fluence [Adapted from [143]].

gap with 800 nm (1.55 eV) photons polarized along the ET chain and by probing the broad spectrum (0.08 - 2.5 eV) covering the Drude upto the CT transition, they report a prompt depletion of spectral weight in the CT band and an increase in the low energy spectral weight (below 200 meV) as shown by colored lines in figure 5.9 (a) and (b) for high and low fluence respectively. The Drude peak (below 200 meV) suggests the formation of a transient metallic state. The delocalization of the charge for all the pump fluences is due to low electron-phonon coupling in this compound. The experiment point towards a spin-charge separation behaviour, typical of 1D correlated electronic systems [143, 144]. The theoretical studies of chemical doping on half-filled 1D Mott insulator also suggests the formation of metallic state at any doping concentrations [145]. The metallic state formed at higher pump fluences decay slower suggesting the crucial role played by electron-electron scattering in the relaxation into the CT insulator.

The dynamics happening while the melting of the Mott gap could not be seen in Okomoto experiment with low temporal resolution. To observe the delocalization process, one requires to measure the band gap on the time scale of hopping ($h/t \sim 40$ fs; $t \sim 100$ meV) of electron. S. Wall et al. observed the coherent electronic excitations in ET-F_2TCNQ on the intrinsic time scale of hopping[53]. The CT resonance was pumped and probed with spectral resolution using nealy single-cycle sub-10 fs long near-infrared laser pulses. The integrated response (not shown here) suggests that the photo-excitation leads to creation of holon-doublon pairs which decays back to ground state of half-filling through a double exponential relaxation. The important result of

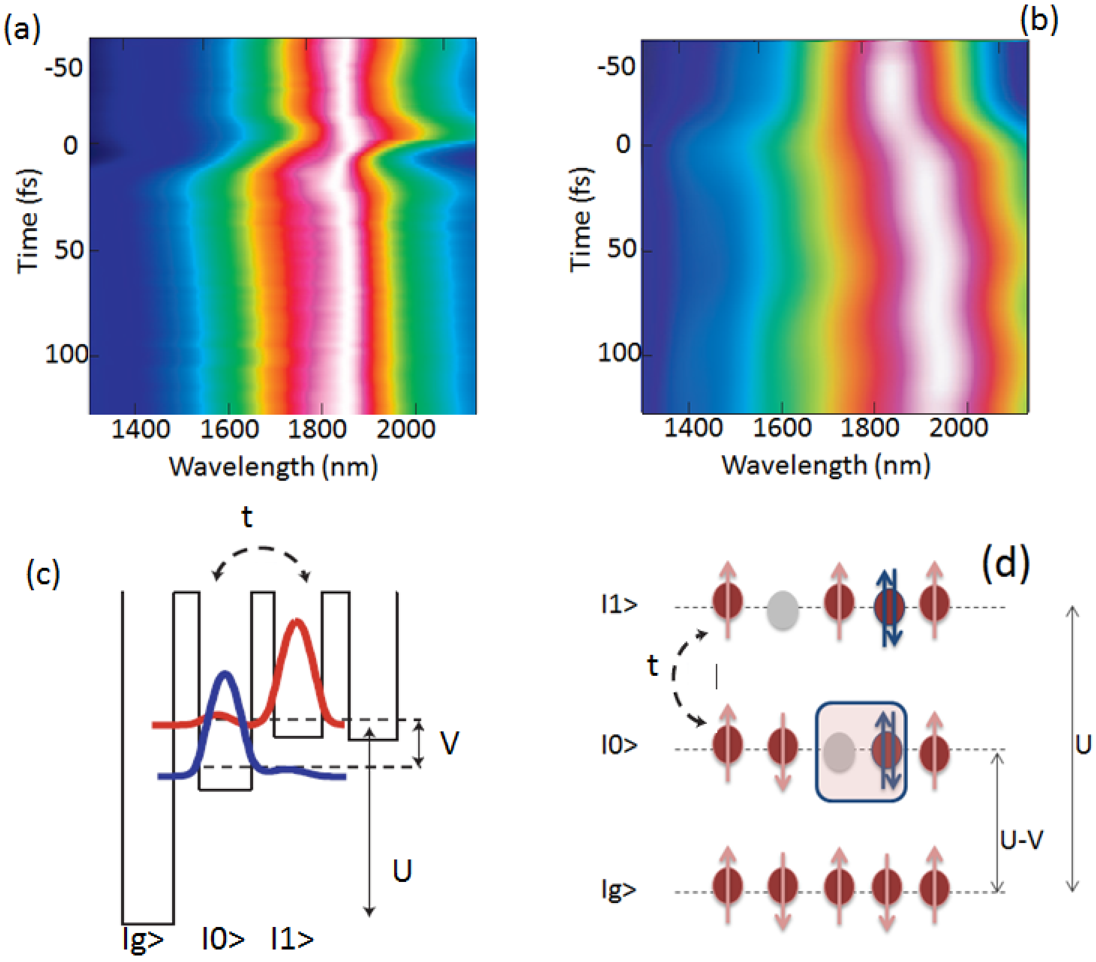

Figure 5.10: (a) Normalized optical conductivity extracted from the reflectivity data for first 150 fs, displaying an oscillatory behaviour of charge transfer band [Adapted from [53]] (b) The time-dependent normalized optical conductivity obtained using two time current-current correlation simulations (c) The potential well of the ground state |g>, bound holon-doublon state |0> and ionized holon-doublon state |1> where the later two are seperated by an energy of V and have hopping amplitude t (d) The representation of the states where red circle corresponds to a half filled ET site, grey cirle represents holon and red circle with up and down arrows represent doublon.

the experiment is the observation of oscillations in the spectrally resolved reflectivity at 25 THz. The retrieved optical conductivity shown in figure 5.10 (a) clearly shows the beating of the CT band around zero pump-probe delay time. This manifest from the fact that during the melting of the Mott insulator, a coherent superposition of two configurations, bound HD pair and unbound HD pair, present in the photo-excited state.

The coherent beating of the two excited states can be reproduced within the framework of the extended Hubbard model. The photo-excitation creating the bound holon-doublon pair (state $\mid 0 >$ in figure 5.10 (c-d)) can evolve into ionized holon-doublon pair (state $\mid 1 >$) through the hopping of the electron to the next site away from the hole. State $\mid 1 >$ plays an important role in the delocalization dynamics of the strongly correlated complexes and most importantly, the quantum many-body physics which so far are studied only in controlled enviornment of optical lattices [146]. The state $\mid 0 >$ has an energy of U -V relative to the ground state $\mid g >$ owing to the on-site Coulomb repulsion between the doublon and inter-site Coulomb interaction between the next to each other holon and doublon. State $\mid 1 >$ has an energy of U as is free from inter-site interactions between the distant holon and doublon. In the photo-excited state, a superposition of bound HD and unbound HD exists and since these states are seperated by energy V and requires one hopping 't' event, the beating frequency between the two states would appear at the calculated frequency given by $((V^2 + t^2)/h)^{1/2}$ = 27 THz (see figure 5.10 (c)). The value is in close agreement with the observed value of 25 THz. The simulated optical conductivity based on the extendend Hubbard model and considering the intereference is shown in figure 5.10 (b). The simulated σ_1 shows the oscillations as observed in the experimental data. This indeed suggests that the superposition of the two states happen during the melting of Mott gap. It demonstrates that the measured reflectivity/conductivity response oscillates due to quantum interference between these different charge pathways.

So far we learned about the I-M phase transition on photodoping the CT band of ET-F_2TCNQ with it being probed on the ultrafast time scale of hopping. The electronic ground state can be modified through the change in filling at lattice site (the case studied so far) or through tuning the microscopic degrees of freedom U, t and V. The next sections deals with the modulation and control of these intrinsic degree of freedom *i.e.* the interaction parameters U, t and V. Their role in controlling the electronic properties of ET-F_2TCNQ is demonstrated. The literature mentioned is among the very first experiments where the remarkable understanding on the relaxation dynamics in 1D Mott insulator ET-F_2TCNQ is revealed by modifying the microscopic parameter of V and t.

5.5 Control of interaction parameters in ET-F_2TCNQ

Three microscopic parameters namely the on-site electron-electron correlation U, the inter-site correlation (V) and the hopping (t) together with their coupling to lattice governs the macroscopic electronic properties and gives rise to its different ground states ranging from metallic to insulating [5, 147, 148]. These parameter are indeed directly related to spatial arrangement of constituting atoms/molecules. The influence of electronic interactions can be very well investigated in the artificial system of ultra-cold atoms trapped in optical lattices [149][3]. The depth and lattice spacing between the potential wells can be controlled straighforwardly by varying the intensity and the angle between the laser beams respectively. The depth of the well defines 'U/t' and lattice spacing defines 'V/t'. This provides a unique opportunity to tune U, t and V for the atoms trapped inside those wells. Feshbach resonances in ultracold atoms involving interaction of the laser light with the cold atoms, faciliates even the independent control over the on-site interaction U [150]. The control of interactions and study of these artificial systems have given us insight into many body physics [151, 152].

The relaxation dynamics of artifically created doublons to single occupancy in a three-dimensional optical lattice was studied by N. Strohmaier et al. [153]. The measured decay life time was found to behave as an exponential function of U/J, where U is the on-site interaction and J is the kinetic energy of the system. This decay relation implies a decay mechanism involving high-order scatterings. The microscopic understanding of such a decay process is relevant to other many body systems and calls for their understanding in real systems.

Though the cold atoms in optical lattices have helped us in gaining an insight on many body physics, however the strong interactions with various correlated electron phases which lead to competing or interwined order parameters in correlated real solid are difficult to replicate. As an example, it is complicated to mimic features like interaction with lattice structure via phonons in case of artificial systems.

It is important to understand in real materials what determines the timescale of ultrafast phase transitions happening at the intrinsic timescale set by the electronic interactions. This study comes with its own challenges. In the next part, we discuss the ways to modify and control precisely the electronic interaction parameter and measure various interesting phenomena like the decay mechanisms of excitons and non-linear coupling of effective Mottness to the lattice parameter in our real solid state model system of ET-F_2TCNQ.

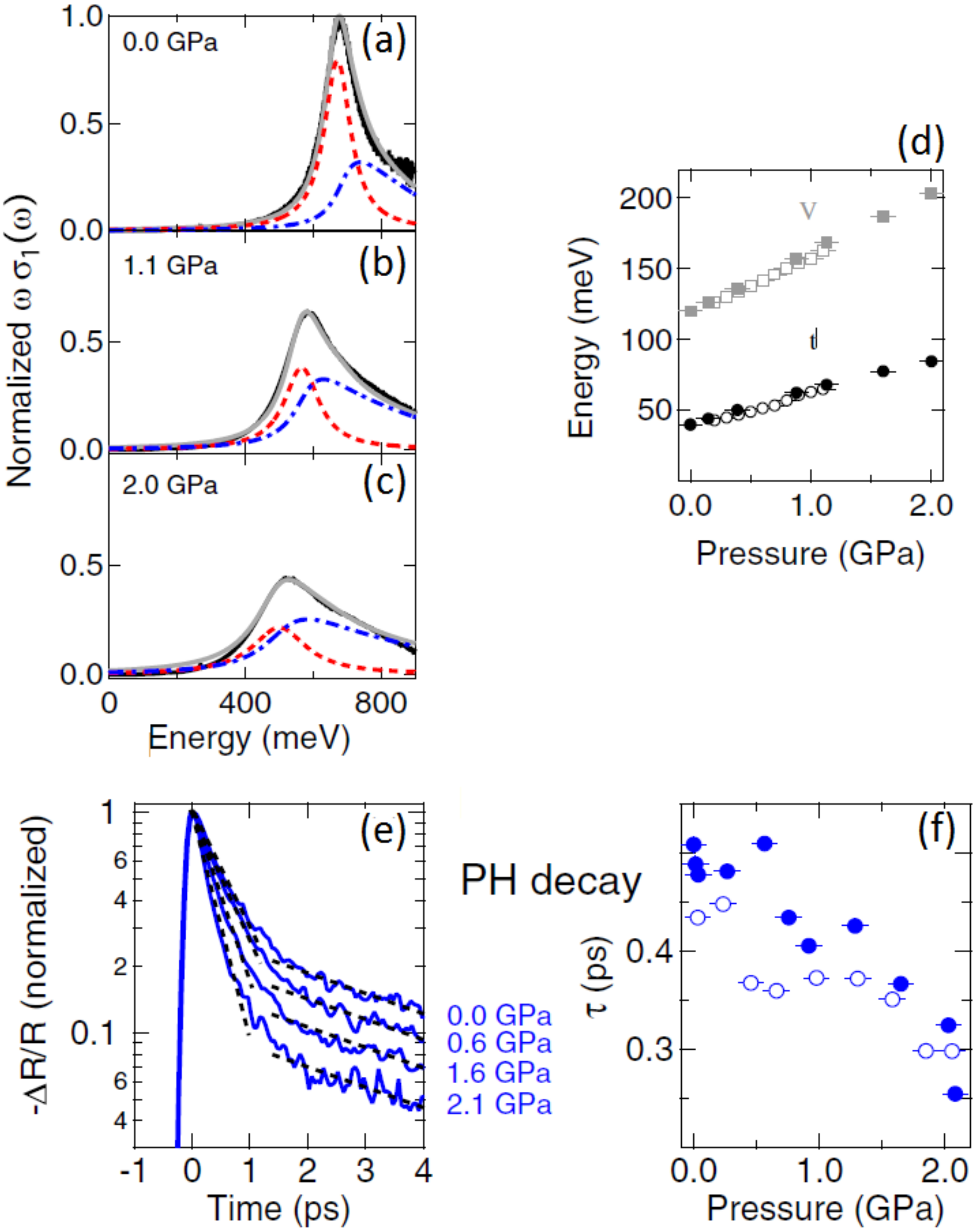

Figure 5.11: (a), (b) and (c) Normalized reduced optical conductivity of ET-F_2TCNQ at various pressures (black line), together with their fit (grey line). Dashed red and dashed blue lines are the contributions from the holon-doublon pair and particle-hole continuum respectively (d) Variation of energies V and t with external pressure. (e) Time-resolved pump induced changes in reflectivity (normalized) at various pressure (f) The fast decay time extracted from pump-probe scan ((i.e.) from fig.5.11(e)) as function of external pressure [Adapted from [19]]

5.5.1 Role of pressure dependent V and t in quasiparticle dynamics

In solids, external or chemical pressure is applied to control the effective interactions [154, 155]. In our model system ET-F_2TCNQ, we applied external pressure (upto 2.0 GPa) using diamond anvils [4] to modify 'V' and 't' and study the influence of the same on the non-equilibrium electronic properties. The quasiparticles relaxation rate studied in this compound is found to have different interaction dependence compared to the simple case of metals and semiconductors, the former being dictated by correlations [19] (see section 2.2 for relaxation dynamics in non-correlated systems).

The application of external pressure can possibly reduce the inter-molecular spacing, thereby increasing the π-orbital overlap between the neighbouring ET molecules. This would correspond to an increase in the hopping probability 't' and also the inter-site Coulomb repulsion 'V'. On the other hand, the local on-site interaction U, relying on the local molecular orbital structure is assumed to stay constant as the pressure applied is not so high to deform the molecule. Information on these tuned microscopic parameters can be then accessed through the model fit on CT band of this molecular compound (as in sec. 5.2.3). The CT resonance is dictated by holon-doublon and particle-hole continuum, defined by the excitonic binding energies and hence the interactions (see the description of eq. 5.3). To extract the interaction parameters, the change in reflectivity was measured across the CT resonance as a function of external pressure varying from 0.0 GPa to 2.0 GPa and at room temperature. Figure 5.11(a-c) shows the corresponding reduced optical conductivity extracted using KK consistant fit to measured reflectivity. With pressure, the CT resonance reduces in amplitude and increases in width. This retrieved optical conductivity (black) was fitted with model (grey line) as described in section 5.3. The variation of the contributions from HD and PH continuum and all the three microscopic parameters were extracted as function of pressure. The lineshape of the HD and the PH continuum individually show different evolution. The HD (the red dash lines) reduces in intensity together with a red shift (lower energy). The red shift of the HD peak given by $U - V - 4t^2/V$ represents an increase of V and t (U is constant). The PH continuum remains centered at fixed value of U but broadens with pressure. Qualitatively, it shows that U remains unchanged and 't' which is function of bandwidth increases. Quantitative values of V and t (assuming U to be constant at 845 meV) calculated with the model fit are plotted as a function of pressure in figure 5.11 (d). As expected, the reduction in the lattice spacing on applying

---

[3] The optical lattice is created by two interfering laser beams, thereby fabricating a periodic pattern of laser energy analogous to the periodic potential wells for the real materials. Atoms are placed inside these periodic intensity wells.

[4] In-situ pressure on the sample squeezed between the diamonds was measured using standard ruby fluorescence method [156] with CsI powder as the hydrostatic medium

pressure led to an increase in the hopping integral t and the inter-site repulsive energy V.

The ultrafast recombination dynamics of photo-excited holons and doublons is studied with pump-probe spectroscopy under pressure. We perform a degenerate pump-probe experiment in which we resonantly excite at the HD peak with 100 fs long pulses and probe the quasiparticles decay dynamics. In our 1D system ET-F_2TCNQ, the CT transient reflectivity reduction can be approximated proportional to the number of holon-doublon pairs injected into the system. Hence the reported pump-probe reflectivity measurement allows to directly access the recombination dynamics of quasiparticles [53, 143]. Normalized pump induced changes in reflectivity at various applied pressures is shown in figure 5.11(e). Reflectivity shows a prompt decrease on photo-excitation because of transfer of spectral weight from the CT band into the Drude peak as is explained in ref, [143]. It is followed by relaxation through two decay channels which are fitted with a double exponential function. The fast decay channel is identified as the holon-doublon relaxation via coupling to molecular vibrations. The decay time constant τ plotted in figure 5.11 (f) decreases with increase in pressure. Similar behaviour is observed when the PH continuum was resonantly excited. The fast decay constant associated to the PH relaxation also decreases with pressure. The increased hopping with pressure, the two states intermix thereby slowing down the relaxation process. The slower decay constant is associated to the coupling among various local molecular vibrations and is found to independent of pressure for both HD and PH within the experimental error bar (not plotted here). The crucial observation is decrease in decay time of both photo-excited HD and PH on application of pressure, which implies that correlations are playing a role in the relaxation dynamics of quasiparticles. Figure 5.12 (a) shows the HD and PH decay time (τ) normalized to ambient pressure decay time constant (τ_0) as a function of effective interactions (U-V)/t , the Mott criterion with pressure.

The recombination of an exciton requires dissipation of energy of the order of U-V (*i.e.* the energy associated to the bound HD pair) to the whole system. The far more likely assumption is that the energy dissipation occurs through a bosonic dissipative bath coupled to the excitons. In case of ET-F_2TCNQ, phononic bath is not feasible owing to its negligible electron-phonon coupling and the large energy to be deposited would require many scattering events to low energy phonons. The other possibility is the high frequency molecular modes as they are coupled well to the electronic charges.

We now consider a simple "Two-sites model" and calculate the decay constant. The decay process introduced only acts on adjacent holon-doublon pairs. This model considers only two neighbouring lattice site in the recombination process. The photo-

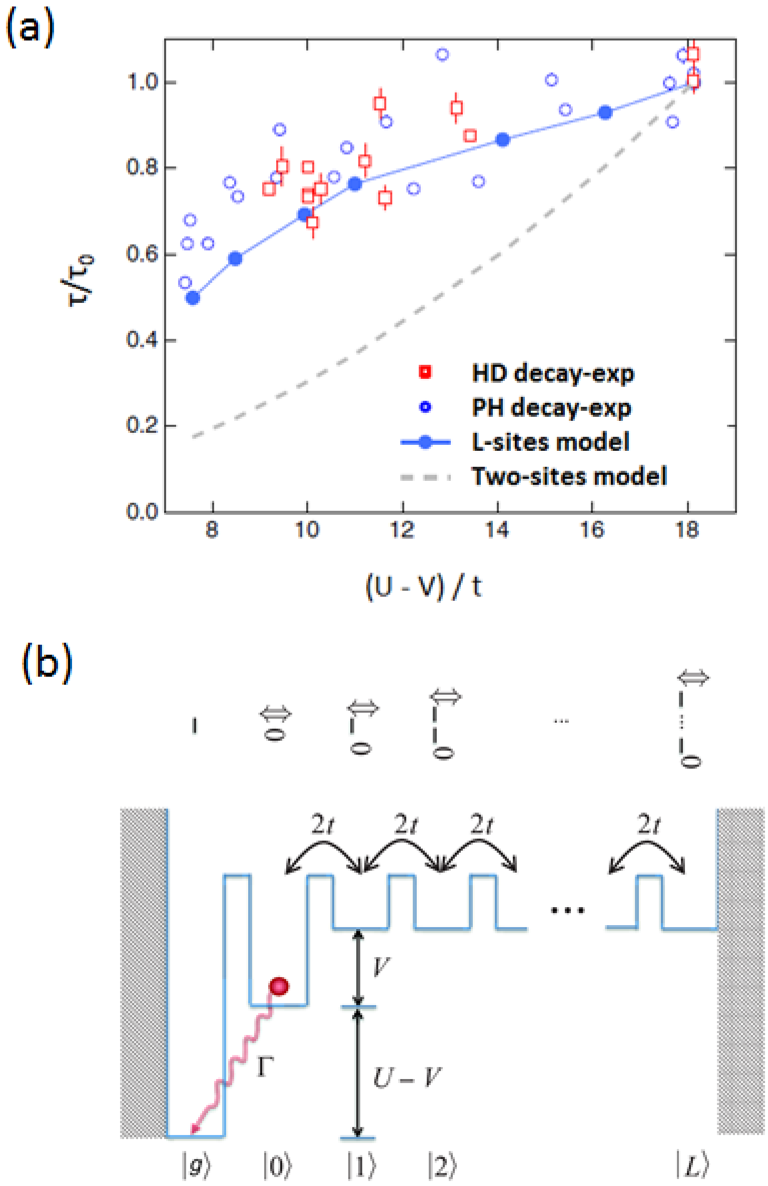

Figure 5.12: (a) Relaxation time of HD and PH (in red and blue open boxes) normalized relative to the value at ambient pressure as function of (U-V)/t values. Dashed grey line is curve for two-site model fit and solid blue line is curve for L-site model fit; L = 20 (b) Effective model of holon-doublon dynamics in the limit of strong-coupling. The ground state |g> is a half filled state with one fermion at each site, whereas the state |0> contains bound holon-doublon pair. The remaining states |l> represent the holon and doublon separated by l sites. These unbound states form the particle-hole continuum in the limit L→∞ t [Adapted from [19]]

induced holon-doublon pair recombines back to the singly occupied ground state configuration via dissipation into local on-site bosonic molecular modes. The two states are seperated by an energy barrier of U - V. Tunneling of bound HD pair to ground state would require energy equivalent to tunneling amplitude t. The incoherent transition |0> → |g> is this two-site model via a Markovian quantum dissipation process with large-bias limit (U - V *ge* t) [157]. The decay constant for this case can be worked out to get [158]

$$\Gamma = \frac{t^2}{(U-V)^2} J(U-V) \tag{5.4}$$

where J(U-V) is the dissipative spectral function. The decay rate obtained is plotted in figure 5.12(a) as the "Two-sites model". Though it shows an increase with effective Mottness consistent with the experimental observation, it also predicts five fold times less slower increase at the highest of the pressure than the observed rate. The model does not account the fact that the holon-doublon pair before recombination to the ground state, can hop to the neighboring site forming unbound HD pair. This is most likely the reason for the observed slow decay constant in the experiment. Such a model is now outlined to see if we get close to the experimental finding on the decay time.

The recombination physics is analyzed under the consideration that 'L' number of sites are involved in delocalization of HD before they recombine. Figure 5.12 (b) shows a model of energy levels of various possible quasiparticle states in photo-excited state. The bound HD state |...− 0 $\Updownarrow$ − − ...> via one hopping event tunnel to ionized HD state |...− 0 − $\Updownarrow$ − − ...>, where |...0...>, |...$\Updownarrow$...> and |... − ...> refers to a holon, a doublon and a singly occupied site respectively. This transition depends on the hopping integral t and on the difference of potential between the two states *i.e.* V. Notably, state |...− 0 − $\Updownarrow$ − − ...> has less chances of holon and doublon recombination compared to |...− 0 $\Updownarrow$ − ...>, as the former requires two hopping events. This qualitatively suggests that the coherent evolution to finite 'L' sites would lead to the suppression of the effective decay rate. In this L-site model, even for L=1, the effective decay constant suppresses as [19, 157]:

$$\Gamma_{eff} = \frac{\Gamma}{2}\left(1 + \frac{V}{\sqrt{V^2 + 16t^2}}\right) \tag{5.5}$$

For L =20, the model (filled circles in figure 5.12 (a)) can completely mimic the experimental lifetimes. The experiment and the theory establish two important conclusions:

- Correlations are important to the quasiparticle decay rate.
- Delocalization dynamics between bound HD pair and unbound HD pair slows down the recombination process of quasiparticles.

5.5.2 Control of effective correlation U/t by selective mode excitation

Importantly, the on-site interaction U is not affected by the above described low pressure dependent experiment as pressure acts only on the molecular spacing. On the other hand, U is influenced by the local atomic physics of individual site. In the artificial system of cold atoms trapped in optical lattices, the strength of this interaction can be controlled through Feshbach resonances [151]. However, on demand control of on-site correlations in real solids has been a long standing target. The molecular solids give a unique opportunity to access the local properties via coupling to their local molecular modes. The control of U has been demonstrated via the molecular replacement method in correlated molecular solids [16] but their active control on ultrafast timescales is non-trivial. As U directly influences the electronic state of the material by tuning U, one can turn the Mott insulating phase to metallic phase and these studies are of relevance for the switching devices.

Here we discuss an experiment reported by Kaiser et al. [18] on the same prototypical 1D Mott insulator ET-F_2TCNQ, a benchmark for the effective electronic interaction modulation which previously has been an inaccessible parameter in solids. They have addressed a remarkable way to control the on-site interactions by exciting a local vibrational molecular mode in a molecular compound. This technique is conceptually different from excitation of phononic vibrational modes. Whereas, the collective lattice motions creates the transient non-equilibrium crystal structure with transient new lattice parameter (bond length and bond angles) and hence new electronic properties, the intra-molecular motion creates transient change in the local parameters like the Mott correlation energy. The molecular vibrational mode facilitates the modulation of the molecular orbital wavefunction, thereby changing the screening and hence the onsite Coulomb repulsion. The lattice modulation over decades have shown novel phenonema like that of insulator-metal transition in $Pr_{0.7}Ca_{0.3}MnO_3$ [12], the enhanced superconductivity in $YBa_2Cu_3O_{6.5}$ [75] and $La_{1.675}Eu_{0.2}Sr_{0.125}CuO_4$ [74]. Here, we discuss the consequence of local molecular mode modulation.

Our model system of ET-F_2TCNQ is photo-excited with mid-infrared laser pulses at 10 μm and electric field strength of 10 MV/cm, resonant to an ET molecular vibrational mode. Figure 5.13 (a) shows the corresponding motion along *c-axis* of the constituent atoms in ET molecule under the vibrational excitation. The displacement leads to deformation of the ring structure of the molecule. The electronic charge in this molecule is mainly placed on C = C and C - S bonds. Therefore a strong modulation of the electron density is accompanied with the molecular orbital variation[5]. After photo-excitation,

---

[5] The displacement of charge density in space creates a transient change in the dipole moment of the ET molecule. That is the reason that this mode is infrared active and hence accessible with light.

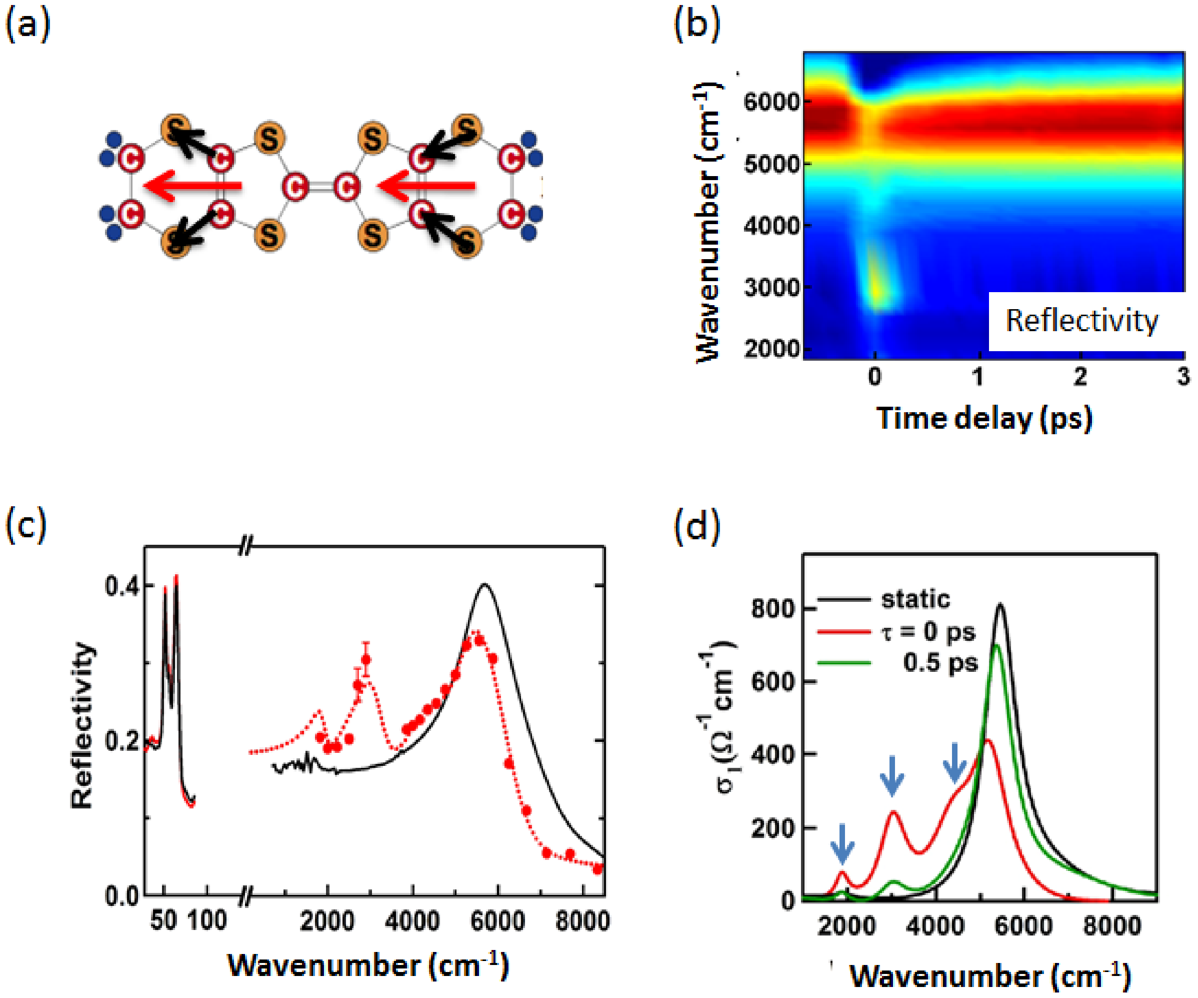

Figure 5.13: (a) Sketch of ET molecule with arrow showing the displacement direction under 10 μm modulation (b) Frequency resolved reflectivity spectra of ET-F_2TCNQ as function of pump-probe delay time (c) Reflectivity cut at equilibrium (black line) and at t = 0 for pump induced reflectivity (red dots). Dashed red line is the Lorentz fit to deduce the optical conductivity (d) The retrived optical conductivity in equilibrium (black line) and in non-equilibrium state at time = 0 ps (red line) and 0.5 ps (green line) after the pump pulses [Adapted from [18]].

the subsequent changes in the reflectivity across the CT band and inside the Mott gap was interrogated over a broad spectral range in MIR (1800 - 3000 cm^{-1}), NIR (4000 - 7000 cm^{-1}) and THz (25 - 85 cm^{-1}) (see figure 5.13(b)). Three important effects could be identified:

- There is reduction in the amplitude and a red shift of the CT band (figure 5.13(b)), pointing towards the reduction of U.
- A prominant side band at $\sim$ 3000 cm^{-1} is formed shifted by approximately 2ω from the CT peak. There is a shoulder to the CT band at $\sim$ 4200 cm^{-1} and a mid-gap absorption at $\sim$ 2000 cm^{-1} in the otherwise fully open Mott gap (see red curve of figure 5.13 (c)).
- No change in the spectral response in the THz range of the spectrum is observed. The equilibrium response (black) and photo-induced response (red) almost overlap in that regime (figure 5.13 (c)). This implies that the vibrationally excited system do not turn metallic in contrast to the above band gap photo-excitation [143].

The reduction and red shift of CT band indicates the reduced U as expected since the electrons on the driven molecular site are more delocalized with larger distributed density, larger molecular orbital wavefunction and hence reduced on-site Coulomb repulsions. Figure 5.13 (d) shows the optical conductivity calculated from the reflectivity curve and shows the same features of side bands labelled by arrows as in the reflectivity response.

We now put upfront a simple picture to understand the experimental observations. In the infinitely heavy oscillator limit, the classical displacement of the molecule under vibration can be expressed as a function of time τ as q=Q cos(ω τ), where Q is the amplitude of displacement and ω is the vibrational frequency (= 1000 cm^{-1}). The quadratic coupling of on-site interaction to the displacement mode would lead to its modulation in the fashion given by U $\sim q^2 \propto Q^2$ (1+cos(2ω τ)). From classical picture, a sideband can be expected at $\pm$ 2ω shifted to the CT peak position. The present picture is certainly different to the Holstein coupling case which considers linear coupling and would have resulted in a sideband located at +/- ω from an unshifted CT resonance.

However, still the simple classical model cannot explain various experimental observations, especially the appearance of other mid-gap absorption bands. These observations are explained by taking into account the finite mass oscillator quantum picture. By considering the back action of the holon and doublon on the vibrational potential, a stiffening and slacking of the oscillator potentials is expected respectively. The driven state is described by a deconstructed Hamiltonian, which considers the local

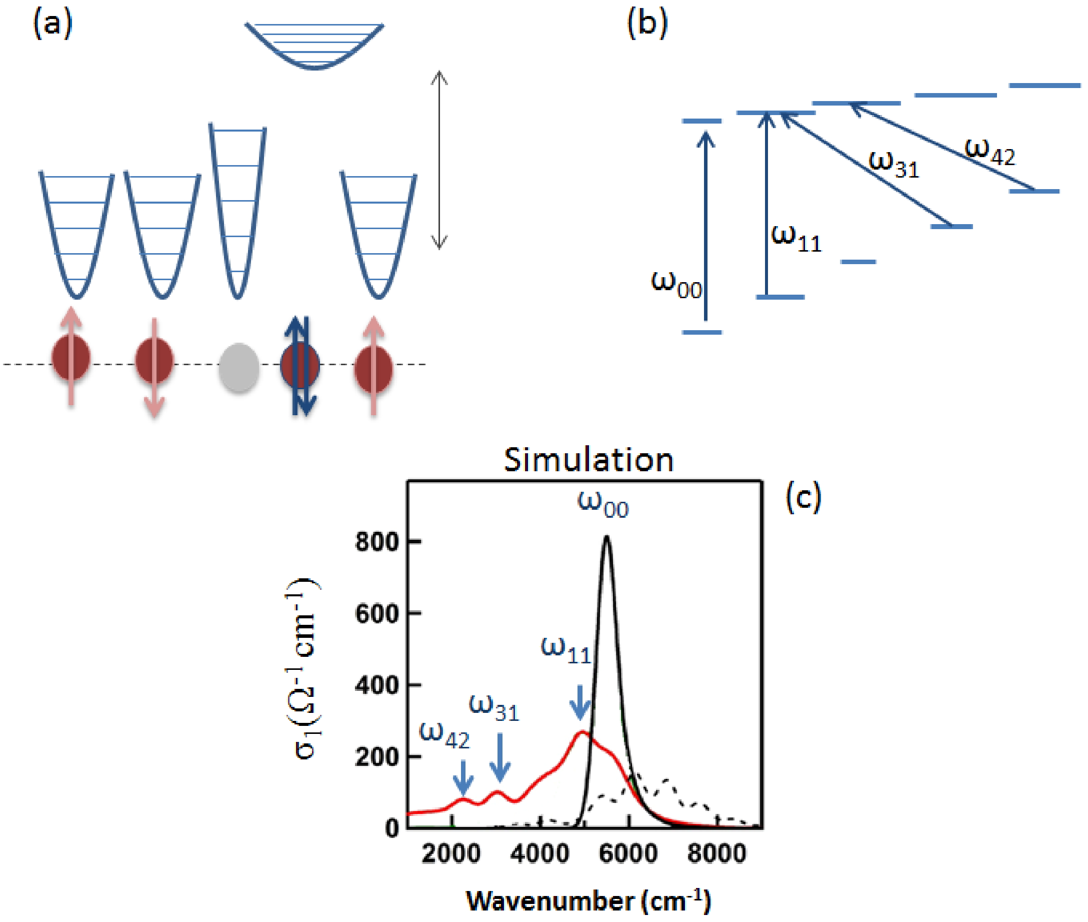

Figure 5.14: (a) The vibrational oscillator belonging to various ET lattice site; the harmonic oscillator at holon site stiffens and at doublon site slackens. (b) Possible transitions accessible exploring the vibrational degree of freedom (c) Simulated optical conductivity in equilibrium (black) and in the driven state (red). Dashed black line represents the case where doublon is mildly coupled and holon is strongly coupled [Adapted from [18]].

vibrational degree of freedom associated to each ET molecule and its interplay with electronic degree of freedom and given as:

$$\hat{H}_{LVH} = \hat{H}_{Hub} + \hat{H}_I + \sum_l \hat{H}_l \tag{5.6}$$

The *deconstructed* Hamiltonian has three contributions:

- $\hat{H}_{Hub}$ is the extended Hubbard Hamiltonian (see eq. 2.2). It includes on-site and inter-site interaction and hopping integral. This Hamiltonian appreciably captures the static as well as the photo-injected dynamics of the optical properties for ET-F$_2$TCNQ [19, 53].

- $\sum_l \hat{H}_l$ is the sum over the harmonic oscillators at site l. Each oscillator is associated with a vibrational frequency Ω_l and displacement coordinate written as $\hat{q}_l$. These oscillation modes are the ones which couple to the CT electron through the charge modulation of their frontier molecular orbitals.

- $\hat{H}_I$ is the coupling Hamiltonian. It is associated to the coupling between the electronic charges and the driven vibrational coordinate under scrutiny and is given by

$$\hat{H}_I = \sum_l (h_l \mathbb{H}_l - d_l \mathbb{D}_l)\hat{q_l^2} \tag{5.7}$$

Here $\mathbb{H}_l$ = (1 - $\hat{n_{l\uparrow}}$) (1 - $\hat{n_{l\downarrow}}$) is the holon projector which couples to the vibrational displacement coordinate q_l^2 with coupling constant d_l. $\mathbb{D}_l$ = $\hat{n_{l\uparrow}}$ $\hat{n_{l\downarrow}}$ is the doublon projector with coupling constant h_l. Clearly, the incorporation of the term $\mathbb{D}_l$ associated to electron double occupancy ($\hat{n_{l\uparrow}}$ $\hat{n_{l\downarrow}}$) makes the Hamiltonian some form of dynamic Hubbard model (see eq.2.6). It is beyond the Holstein model which considers the dressing of even singly occupied electronic state by the bosonic modes.

The deconstructed Hamiltonian $\hat{H}_{LVH}$, termed as the "vibrating dynamical Hubbard model" and includes the role of electronic and vibrational modes and the influence of double occupancy of electron at lattice site [57, 58].

$\hat{H}_I$ and $\sum_l \hat{H}_l$ are negligible in the ground state owing to sufficiently small coupling but if the molecular mode is driven then its influence can be enhanced and made visible. If we consider now the onsite interaction term with different coupling constants for holon and doublon, its effective modulation would be (h-d) q^2. The higher coupling to doublons compared to holons give negative value to the term (h - d) and this explains why the charge transfer dictated by U shows red shift.

Under the influence of different charge background provided by the holon and the doublon to the the vibrational oscillators, these oscillators renormalize differently. The vibrational oscillator at holon site stiffens and the one with a doublon slackens [159, 160] as shown in figure 5.14(a).

The real part of optical conductivity is calculated based on vibrational dynamical Hubbard molel via two time current-current correlation function (see figure 5.14). To fit the experimental data, the renormalization of oscillations at holon and doublon site is required. The renormalized value of doublon oscillator frequency is Ω_d = 0.26 Ω and for the holon is Ω_h = 1.10 Ω. The later required a mild change compared to the doublon oscillator. This reorganization is shown in figure 5.14 (b). The different oscillator ladder on the holon and the doublon site led to the possibility of new transitions which corresponds to mid-gap bands at ω_{00}, ω_{11}, ω_{31}, ω_{42}. The simulated σ_1 (ω) convincingly reproduce the optical conductivity extracted from the experimental data (see figure 5.13(d)). The key conclusions that can be made are:

- The dynamic control of Hubbard U is possible via local vibrational mode excitation in a solid state system.
- The holon and the doublon generated in the charge transfer process couple differently to the molecular vibrations.
- Another important finding of this experiment is the quadratic coupling of U with respect to the vibrational displacement coordinate.

One of the ways to better understand this quadratic coupling would be to measure real time changes in U while the molecule is oscillating. This approach demands for very high resolution of the order of sub-10 fs and carrier-envelope phase stable driving field. We undertake this approach to understand the electronic dynamics and its coupling to vibrational modes and is reported in chapter 6.

5.6 Summary

This chapter introduced 1D correlated electron systems and their significant difference compared to higher dimension systems. In particular, the enhancement of the quantum effects and henceforth, a richer hitherto phase diagram was described. A prototypical 1D organic salt ET-F_2TCNQ with half-filling was introduced. This molecular charge transfer solid is a perfect testbed to study and control the electronic properties. The optical properties reproducing the quasi-1D characteristic were described followed by the steady state fits to the optical conductivity required for the extraction of microscopic parameters U, t and V. The theoretical understanding of photo-excitation of 1D Mott insulator in general was put forward, underlining the fact that the correlation parameters define the excitonic pathway taken by them. The experimental literature on the photo-doping of the CT band in ET-F_2TCNQ is reviewed giving insight into the delocalization dynamics of excitons. Various schemes are explained to access the control over the microscopic parameters U, t and V in real solid state system. In particular, two different experiments are introduced: (1) varying V/t using pressure, the reduction of quasiparticle relaxation rate with effective correlation in a Mott insulator established that the relaxation to ground state is suppressed by the delocalization of quasiparticles. (2) The control of the Hubbard U is acheived via accessing the local molecular vibrations. Its quadratic coupling to the vibrational displacement coordinate is exposed. Taking advantage from the deconstructed *vibrational dynamic Hubbard* *model*, we propose the asymmetric renormalization of holon-doublon harmonic oscillators to the charge coupling.

6 Dynamic control of electronic correlations in a solid state Mott insulator

6.1 Dynamic control of Hubbard U

In the previous chapter, we introduced the technique to control the Hubbard U through the excitation of the molecular vibration mode in ET-F_2TCNQ. There the spectrally resolved measurements strongly suggest a quadratic coupling of the vibrations to the interaction U as the cause of observed sideband shifted by 2ω from the CT resonance. To substantiate this observation and to have a direct insight into the dynamics of U, the temporal evolution of CT band is required. As described in section 5.2.3, the CT band governs information on the Hubbard U as well as on other two microscopic parameters *i.e.* V and t whose values can be extracted by fitting the optical CT band with our analytical model. This approach to see the changes in CT band faster than the phonon oscillation demands a non-trivial temporal resolution of the order of few femtoseconds and phase stable excitation for the experiment. Before discussing that, let us put forward this approach. The physical picture of the experimental idea is shown schematically in figure 6.1. Consider a pump laser pulse with the electric field of time period T (dashed black line), resonant to the 10μm vibrational mode of ET molecule along *c*-axis. This would lead to concurrent local movement of the electron densities of the ET molecule along the electric field of the pump pulse. The crest of the electric field will displace the electronic densities along one side of the *c*-axis and the trough, to the other side. This movement accompanied by the periodic variation of electron densities within the ET molecule is depicted in the lower panel of the figure 6.1 (the electronic orbital densities of the ET molecule were calculated by Kaiser et al. using Gaussian03 software [18]). The time dependent variation of the local charge densities (solid black line) would occur at twice the driving electric field because it is proportional to square of the displacement. This modulated charge density changes the screening and therefore the on-site interaction U. To measure the changes in Hubbard U, we aim to measure out the evolution of CT band over time.

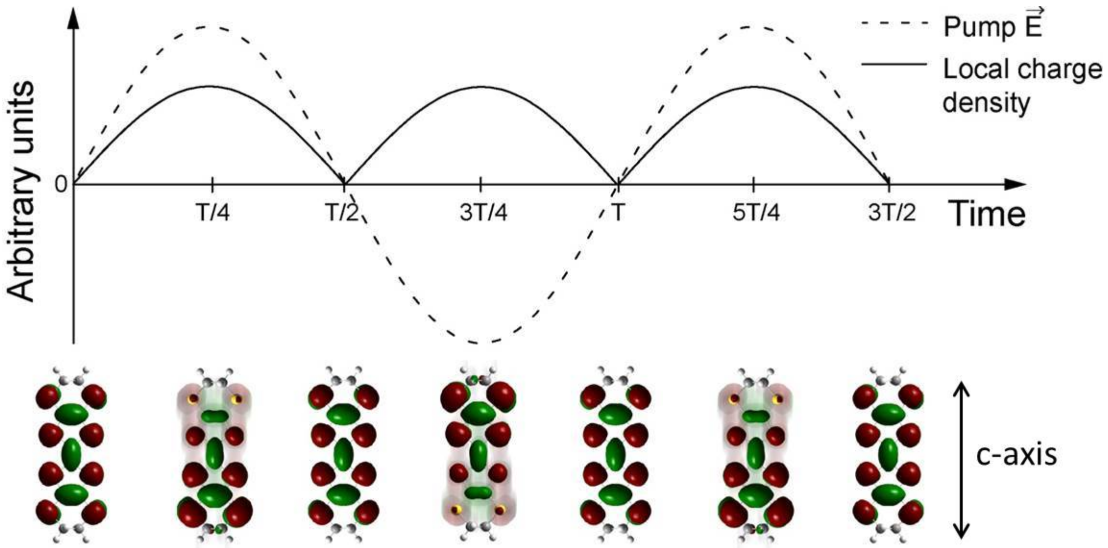

Figure 6.1: (upper panel) The temporal variation of the pump electric field (dashed black line), together with the resultant change in the local charge density (solid black line) and (lower panel) the corresponding orbital motion of vibrationally excited ET molecule along c-axis in time.

This task requires the interrogation of the CT band while the molecule is oscillating with the electric field of the pump. The pumped phonon is at 10μm which corresponds to oscillation period of 33 fs. Atleast one-fourth of this time period is requisite for the probing [114]. Altogether it implies that a ultrafast broadband probe, approximately 8 fs long and overlapping the CT band are essential. Another crucial requirement for the experiment is having the carrier-envelope phase stable pump pulses at 10 μm (with electric field time period of 33 fs). If the pulses are not stable over phase, the effect due to the electric field will be averaged out over scans and we will be left with just the effect of envelope of the pump. We instead target the dynamics within the electric field and hence need CEP stable MIR pulses. Thanks to the advent in nonlinear optics which could fulfill both the requirement on the pump and the probe side. Mixing two near-infrared signals produced from the same white light in the difference frequency generation (DFG) process results in phase stable pulses and for the extreme time resolution in near-infrared pulses, we applied pulse compression scheme using a deformable mirror. Their generation is discussed in the next section. Based on both superior temporal resolution (approaching the single-cycle limit) and the phase stable pump laser, we have been able to access the electronic dynamics within the single cycle of oscillation of the molecule.

6.2 Nearly transform limited NIR pulse generation

This section brings forward the scheme used to generate broadband spectra spanning over 1200-2200 nm wavelength in the near-infrared region. The pulses generated are compressed to nearly transform-limited duration. This verifies when all the colors in the spectrum have same spectral phase, corresponding to a minimum in the time-bandwidth product, in accordance with Heisenberg's uncertainity principle. The lower limit of pulse duration for a given spectrum is a characteristic feature of the Fourier transform. These laser pulses are used as a probe to capture the fast dynamics in an organic Mott insulator.

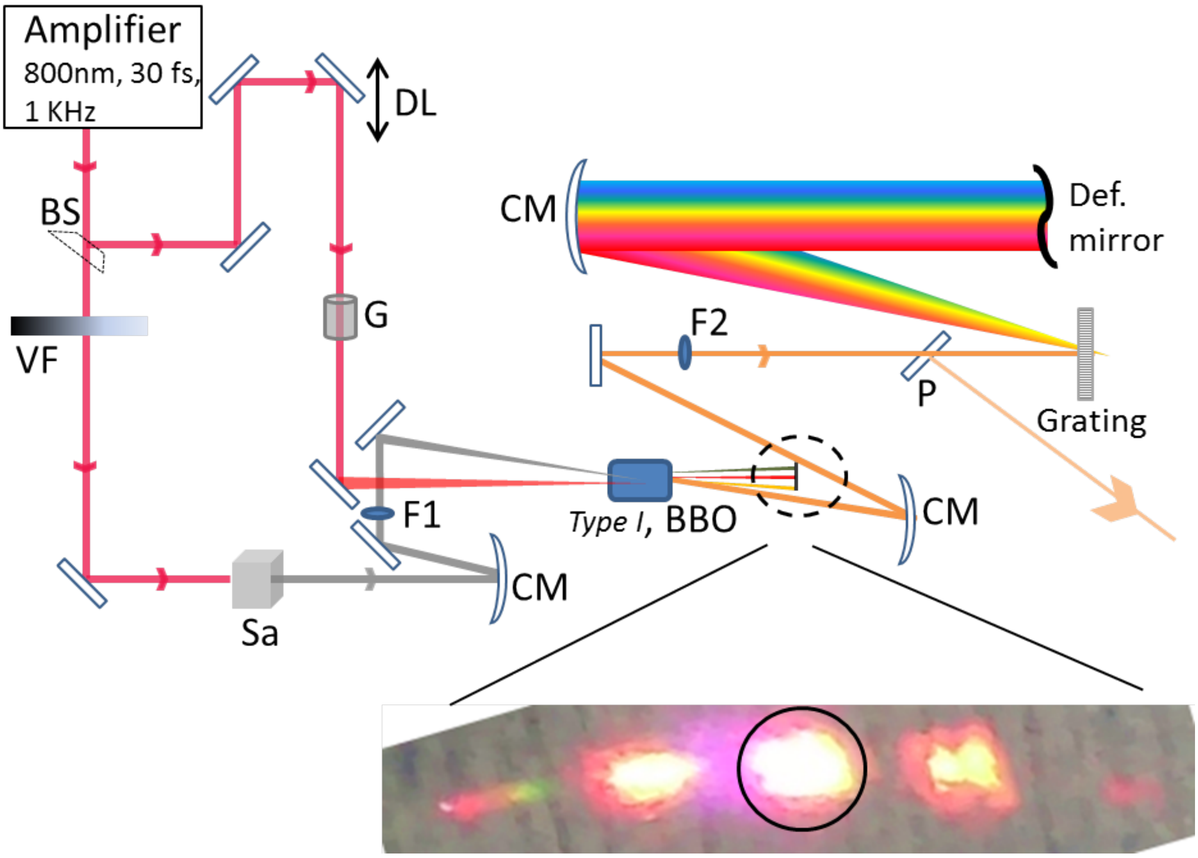

Figure 6.2: Schematic diagram of NIR pulse generation and compression. BS:Beam Splitter, VF: Variable Filter, CM: Curved Mirror, G: Glass block, DL: Delay line, F1: Filter λ>1000 nm, F2: Filter λ>1150 nm, Sa: Saphire crystal. A zoom into the signal beam (in solid black circle) and idler beams generated is also shown.

The schematic diagram of near-IR OPA setup is shown in the figure 6.2. The system is pumped with 120 μJ, 35 fs long, 800 nm pulses at repetition rate of 1kHz from a

Ti:sapphire laser. Approximately $\approx 3\ \mu$J of pump energy is focussed on a sapphire crystal, generating a white light continuum spectrum ranging from 400 nm to 2200 nm. They are transmitted through a long pass filter F1 with $\lambda > 1000$ nm, to avoid any amplification of the shorter wavelengths. These pulses then serve as our seed for the OPA. The remaining pump energy is focussed together with the orthogonally polarized seed pulses on a nonlinear crystal (BBO) cut for type I phase matching (θ = 19.8°, ϕ = 90°, thickness = 0.03 cm). A small angle of approximately 1° between the pump and the seed is used to ease the separation of the amplified seed from the pump beam and also to avoid any interference between identically polarized signal and idler beams. Figure 6.2 also shows a zoom into the array of colors generated on a black paper about 5 cm away from the BBO. The near-infrared spectrum obtained has a broad gain bandwidth, thanks to the low group velocity mismatch between the signal and idler beams, owing to satisfaction of near degeneracy condition. The spectrum of NIR is captured using a Bayspec NIR spectrometer: 1100 to 2200 nm model, an array detector of InGaAs at sensor temperature of $-13°$ C and is shown in figure 6.3. The spectrum has a FWHM = 600nm. The output pulse energy varies from 2 μJ to 4 μJ.

Compression of pulses using deformable mirror The next step toward the generation of ultrashort pulses is the compression in time domain apart from the broad spectrum generation. This is achieved using deformable mirror (DM) in combination with a grating in a 4f-configuration. The DM is a 45 X 15 mm rectangular mirror made of thin silver coated membrane, with 30 electrodes at its back to control the shape of the membrane. Each electrode can apply voltage upto 300 V [161, 162].

The generated near-infrared beam is spatially chirped using the grating as shown in figure 6.2. A concave mirror (f = 25 cm) collimates the beam and send to the DM. The position of the frequencies is calibrated on the DM. One of the calibration table ensuring the beam hitting symmetrically with respect to the center of DM is written below. thereby sending the different frequencies within the broadband NIR spectrum to different parts of the DM.

Calibration table

Position on the Deformable mirror	-10	-6	0	6	10
Wavelength(nm)	1472.5	1599	1727.7	1852.7	1977.6

0 position refers to the center of the DM. The values quoted above are among the good ones when the beam hit the DM without being clipped. The beam goes back onto the CM and the grating at a lower height and is sent out by the pick mirror P. The grating, CM and DM are in 4-f configuration, implying beam travels 4 times "f" in between these components. The optical path for each frequency can be tailored applying

different voltages to the electrodes. The last component of the NIR setup is 8.5 mm thick SF11 glass used to compensate the positive chirp of the near-infrared beam and thereby helping deformable mirror as it would require less deformation.

Before discussing the process of DM compression, we discuss here the pulse characterization method *i.e.* FROG.

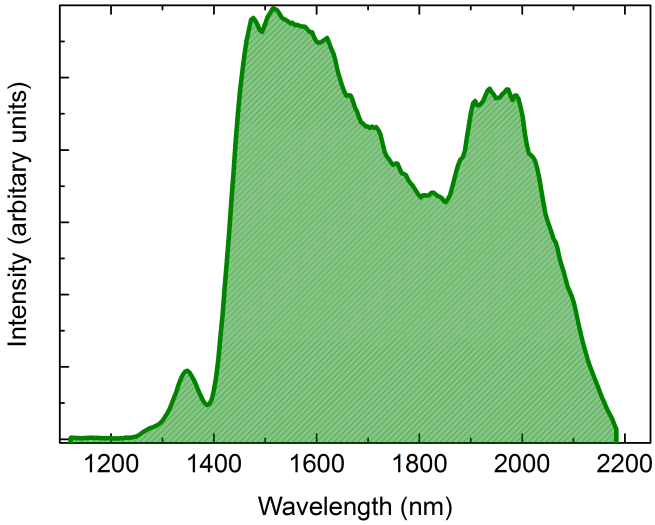

Figure 6.3: Typical spectrum of ultrabroadband NIR OPA.

Frequency resolved optical grating (FROG) technique FROG can be described as frequency resolved auto-correlation. The setup is shown in figure 6.4. A beam splitter (BS) is used to split the beam in a ratio of 50:50. The beam splitter for our broadband NIR pulses were manufactured in Laser Zentrum, Hannover. They have metallic coating on testglass B270, optimized for 45 degree angle of incidence and S-polarization. The beams are focussed onto a BBO crystal for second harmonic generation, which is then sent into a spectrometer for frequency resolved information of the near-infrared pulses. By varying the time delay between the two beams using delay line (DL), the frequency and time resolved second harmonics of our NIR is mapped and plotted in figure 6.5 as frog 1.

The efficiency of SHG inside a BBO is higher for lower wavelengths (see eq. 14 where parametric gain is directly proportional to the frequency). In such a case, the output second harmonic intensity for lower wavelengths can be large enough to saturate the spectrometer. To prevent this to happen, we used filters G16 from HEBO spezialglass with 27% transmission at 700 nm and 90 % at 900 nm. In such way, we could increase the integration time of the spectrometer to capture photons at longer wavelengths without saturating it. Furthermore, the lens to focus the second harmonic into the spectrometer was set on the delay stage to optimize for longer wavelengths, facilitated by the fact that the different frequencies have different focal points.

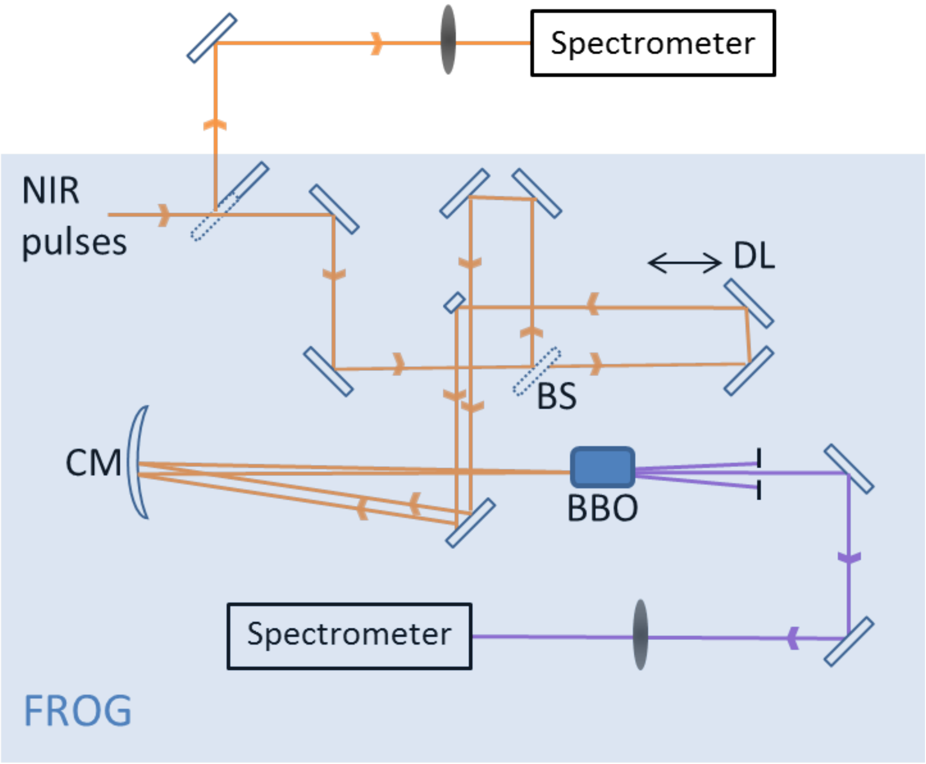

Figure 6.4: FROG: Setup for NIR pulses characterization

The measured FROG trace is shown as Frog 1 in figure 6.5. The electrodes were set to 0V for this first measurement ensuring flat surface of the DM. The temporal chirp is observed in Frog1. The phase information is extracted from the Frog1 and is sent to the DM software for compensation. The mirror bulges out for a negative phase of certain wavelength and vice-versa. The FROG trace after the first compensation is shown as Frog 2 in figure 6.5. Further iterations are made on the phase and the corresponding FROG traces are shown. The normalized intensity profiles corresponding to the four FROG traces is shown in figure 6.6. Each iteration led to a decrease in FWHM of the pulses, demonstrating the compression of the pulses. The final iteration generating Frog 4 trace is 10 fs long, reaching almost the transform-limited duration of 8 fs.

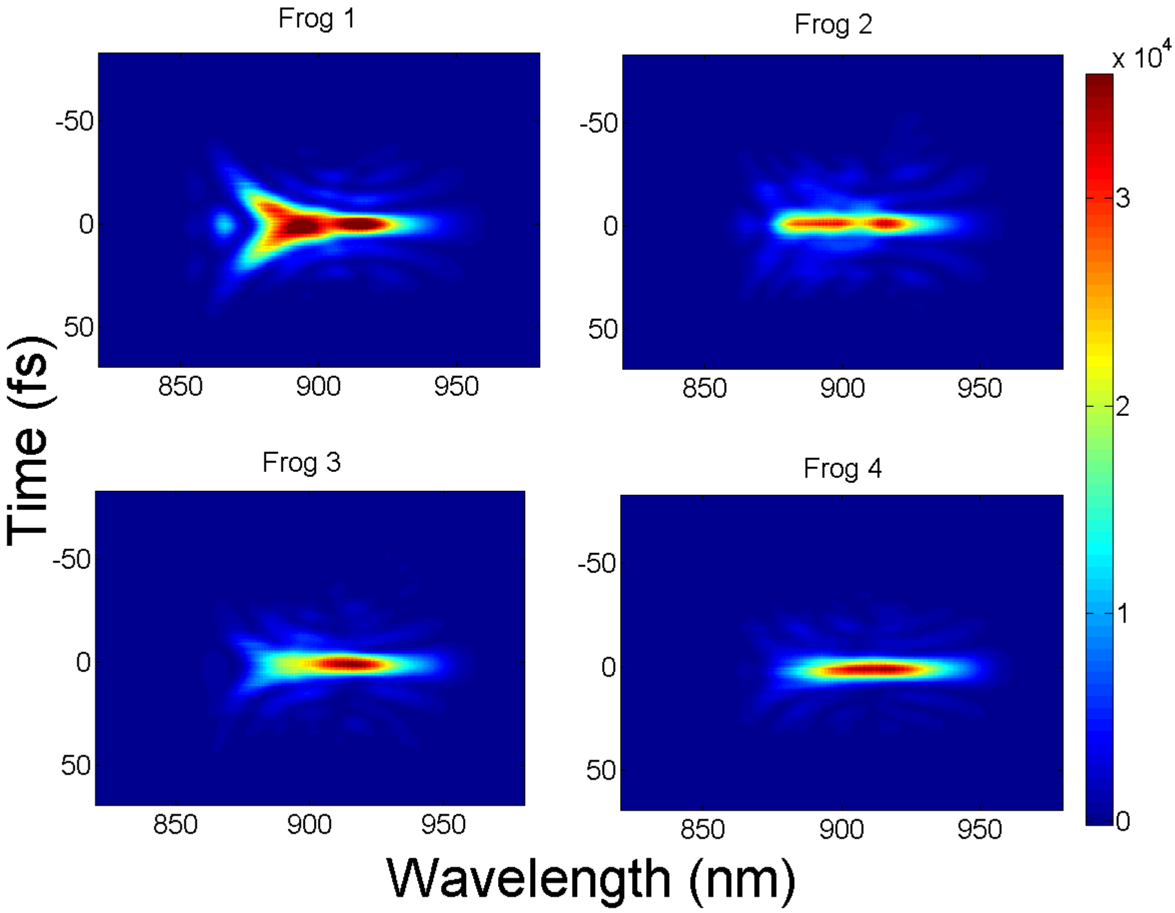

Figure 6.5: Frog1 - 4 are the FROG attained with phase correction iteration done with deformable mirror, where Frog 1 is with flat front of the deformable mirror.

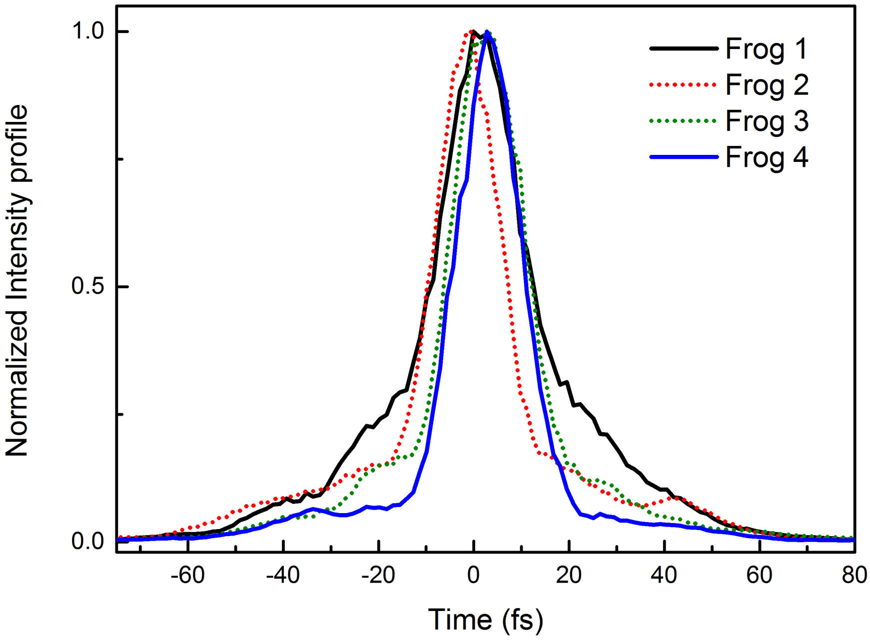

Figure 6.6: The normalized intensity profiles for Frog's 1 - 4.

6.3 Phase stable MIR pulse generation

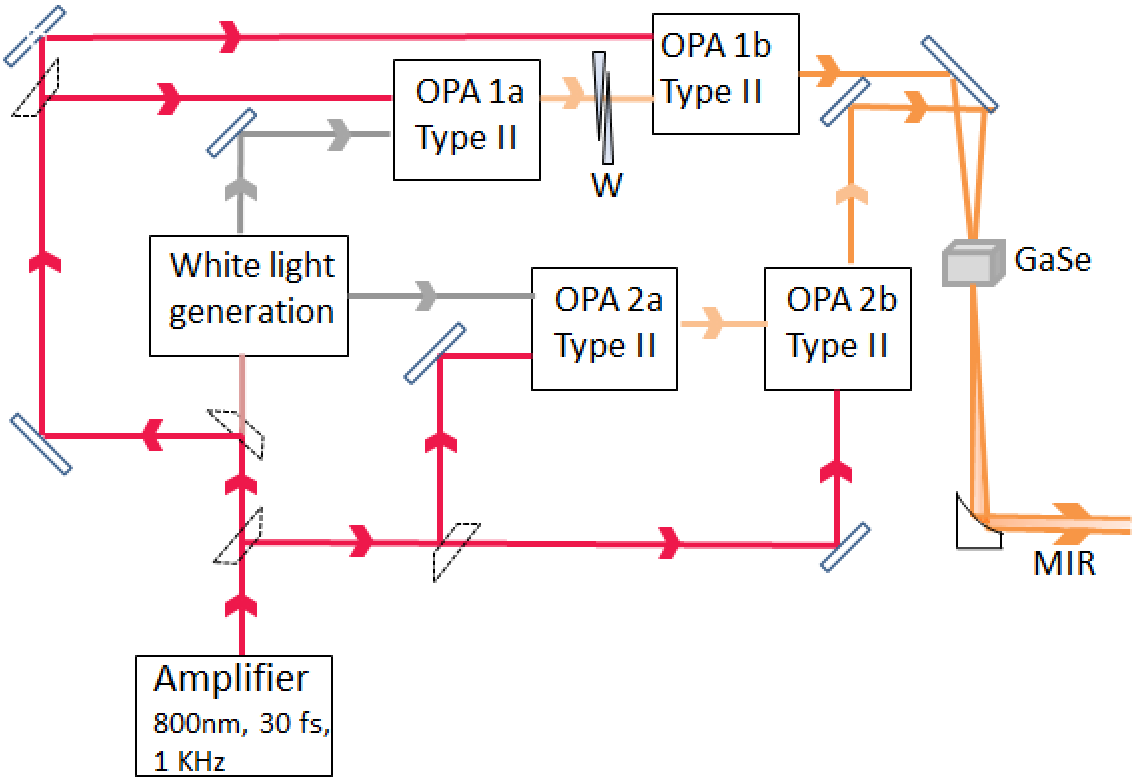

Figure 6.7: Schematic diagram of the optical setup generating mid-infrared beam.

An OPA (see apendix 7.2) is limited to near-infrared pulses generation because of the limited spectrum of the white light seed. However, the mid-infrared pulses can be generated by exploiting the concept of DFG between two near-infrared beams from OPA's. This section describes DFG employed together with active phase stabilization technique to obtain the carrier-envelope phase stable mid-infrared pulses *i.e.* with the relative phase of the envelope and the electric field which stays constant from one shot to another.

Figure 6.7 shows the schematic picture of the setup used for the generation of phase stable mid-infrared laser pulses. Approximately 1 mJ of the 800 nm from the Ti:sapphire amplifier at 1 kHz repitition rate is pumped into the setup. 2-3 % of this energy is used for white light generation and rest of it is divided into two equal parts to run two similar OPA branches, where each branch contains two amplification stages. The first stage of each OPA branch amplifies a narrowband of white light at the cost of pump power. The BBO crystal is tuned to phase match at 1200 nm for one and 1385 nm for the other branch. These weakly amplified beams are sent to the second amplification stages. The output energy is ∼120 μJ for 1200 nm and ∼100 μJ for 1385 nm. Their intensity spectra (with different integration times) are displayed in figure 6.8. For the generation of mid-infrared, both near-infrared beams are focussed on a 200 μm thick galium selenide (GaSe) crystal. The DFG ($(1/1200 - 1/1385)^{-1}$) between the two generates pulses at wavelength of 10000 nm (10 μm or 30 THz) producing 2 μJ of energy. The electro-optic sampling method employed to characterize the pulses is discussed further.

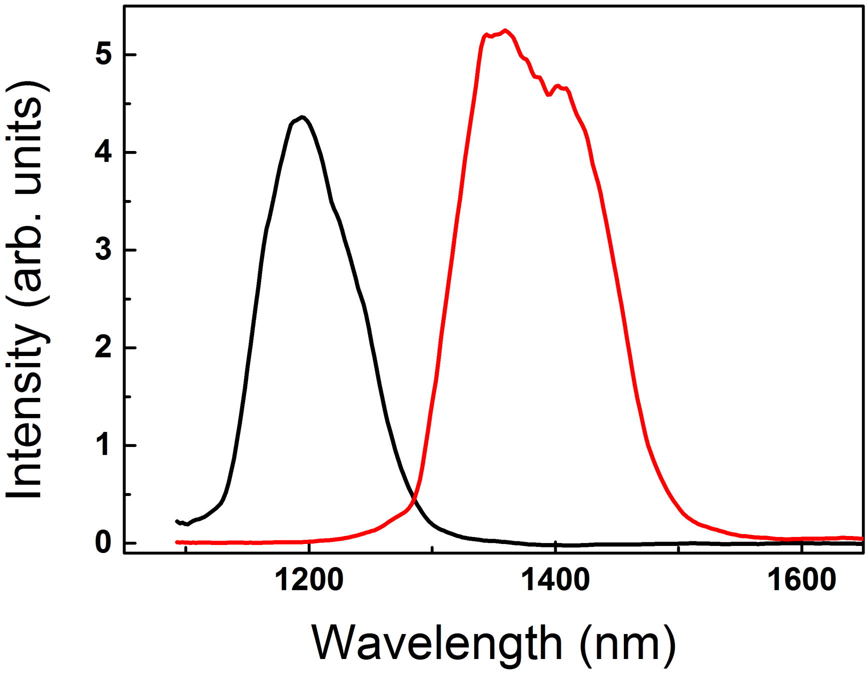

Figure 6.8: The power spectrum of consitutuent NIR beams at 1200 nm and 1385 nm for MIR generation

Electro-optic sampling: The setup of electro-optic sampling (EOS) is shown in figure 6.9. It is also based on DFG between cross-polarized MIR pulses and 800 nm gate pulses in GaSe crystal. The side band generated is cross polazied with respect to the MIR. The wave plate and Wollastone prism are aligned such that in the absense of MIR, the component of the gate pulse with parallel and perpendicular polarization are fed into the two balanced detectors scheme. In the presence of the MIR pulse, a side band with rotated polarization proportional to the electric field of the MIR enters the balanced detectors. The difference in intensity at the two detectors is the measure of the electric field of the MIR pulses. Figure 6.10 shows the measured electric field of the MIR pulses and its Fourier transform at 30 THz. The asymmetric shape of the electric field must come from the nonlinearity of the detection crystal [163].

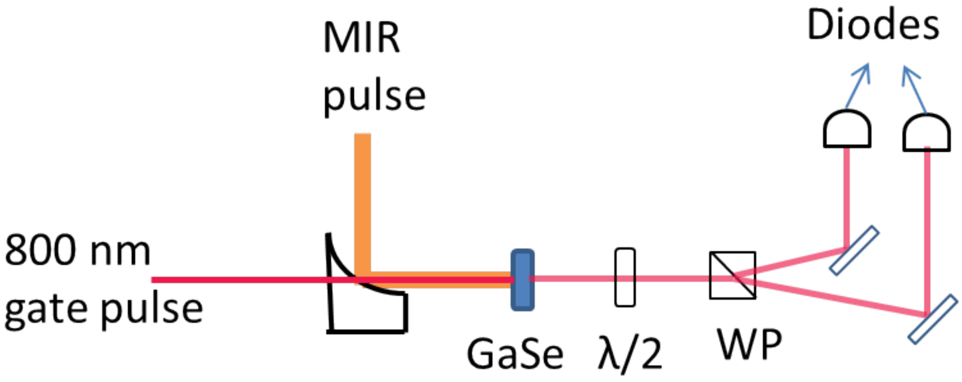

Figure 6.9: Schematic diagram of electro-optic sampling of MIR pulses

6.3.1 Carrier envelope phase stablization

When the temporal offset between the electric field and its intensity envelope is constant, the pulses are termed carrier-envelope phase stable. If ϕ_1 and ϕ_2 are the absolute phases of the two NIR pulses, undergoing difference frequency to produce MIR, then the phase of MIR pulse generated is given by ϕ_{DF} = ϕ_1 - ϕ_2 -$\pi/2$. The two NIR pulse used originate from the same white light, implying that they relatively should have constant phase difference. Their phases are related to each other as ϕ_2 = ϕ_1 + $\Delta\phi$, where $\Delta\phi$ is constant phase difference the two. One therefore expects to have constant phase of the MIR, as ϕ_{DF} = - $\Delta\phi$ - $\pi/2$.

However, instabilities of the two NIR beam relative can lead to some drift of ϕ_{DF}. The instability can arise from temperature variation creating mechanical modulation of the path length of the two beams [164]. Figure 6.10 (a) shows the shift of the electric field phase over time from one shot to another.

To compensate for these slow drift, we use a EOS stablization technique in time domain. We fix the timing of the optical gate on the delay stage such that the electric field value is zero on the lock-in. Over time, when the electric field starts to drift, the value also starts to deviate from zero on the lock-in, reflecting the shift of the MIR carrier-envelope phase. The software reads this shift and accordingly inserts or removes the wedge placed in the path of one of the NIR beams, thereby compensating for the optical path difference. Figure 6.10 (b) shows the two EOS trace at different times when the compensation scheme was active. Clearly, the electric field traces on top of each other confirms that the MIR pulse is phase stable.

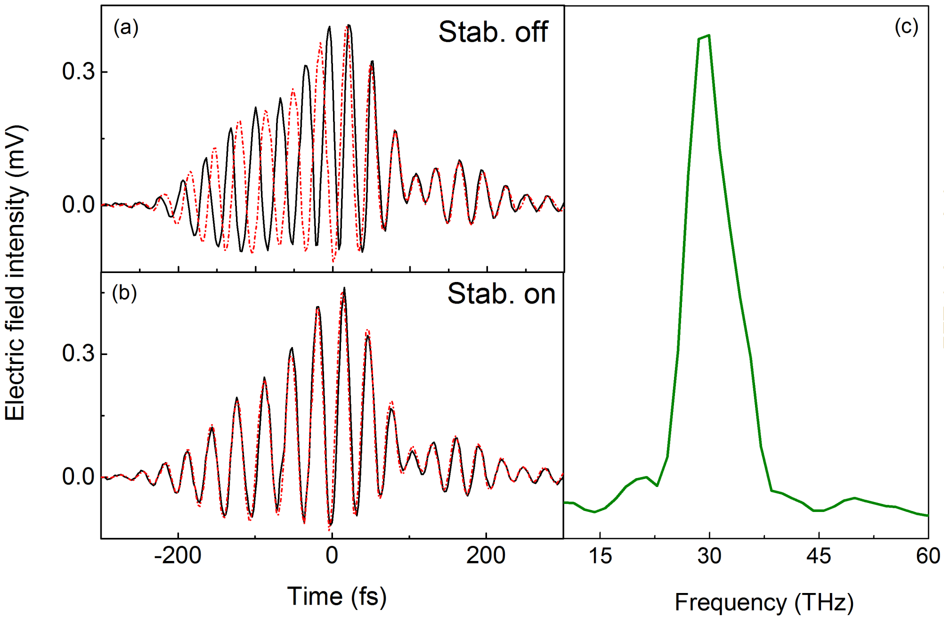

Figure 6.10: Electric field deduced from Electro-optic sampling of MIR pulses at 30 THz at interval of 5 minutes in black line and dashed red line, with corresponding Fourier transform.

6.4 Non-degenerate pump-probe setup

The pump-probe setup used to perform dynamical studies on ET-F$_2$TCNQ is shown in figure 6.11. The carrier-envelope phase stable MIR pulses are used as pump beam. They are focused to a spot size 230 μm onto the sample using a parabolic mirror with focal length of 5 cm. The probe beam can pass through a hole in the parabolic mirror. Both pump and probe are in collinear geomerty. The nearly transform-limited NIR probe pulses are used as probe pulses and are focused onto the sample using a concave mirror of focal length 20 cm. Both pump and probe are incident nearly normal to the sample surface, important for these extreme time resolution measurements. The reflected NIR probe from the sample is collected onto a diode for the computation of the integrated response. The photo-diode used is InGaAs baised detector with absorption band ranging from 1.2 μm to 2.6 μm. For the spectrally resolved measurements, the diode is replaced with a NIR spectrometer. (Bayspec NIR Spectrometer:1100 to 2200 nm). The pump beam is physically blocked to prevent scattered light in the detectors. The ET-F_2TCNQ crystals used in the experiment were grown as described in ref. [165] and are approximately 80 μm thick and 0.8 mm length along the *b*-axis.

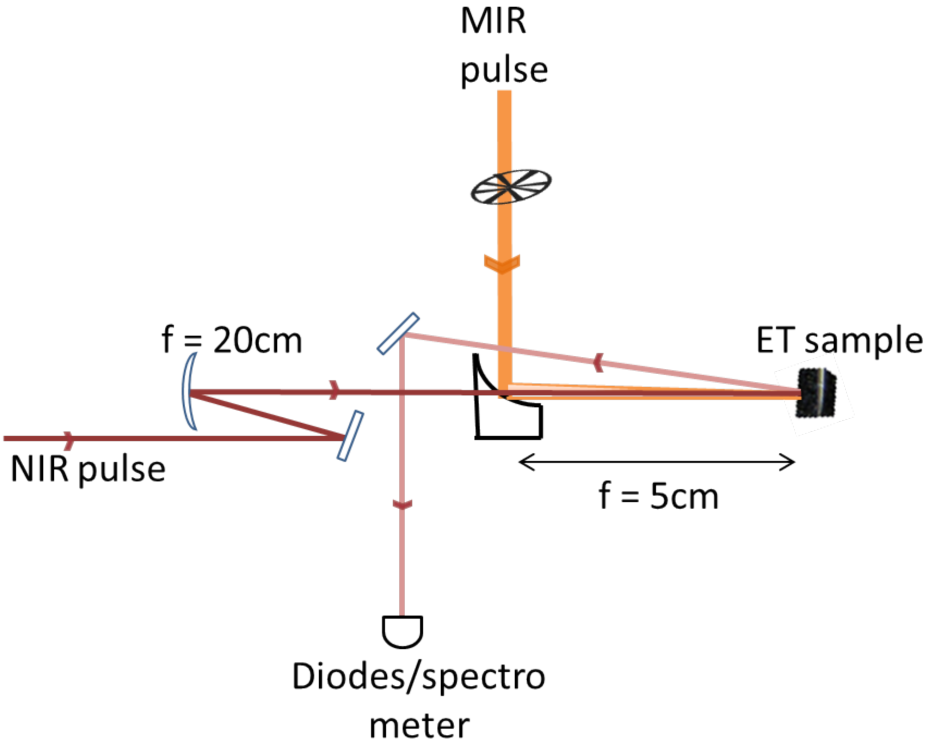

Figure 6.11: Schematic diagram of pump-probe setup used for MIR pump-NIR probe experiment on ET-F_2TCNQ.

The details of the laser setup generating the required pump and probe laser pulses and their characteristics are given in sections 6.2 and 6.3. Summarizing the experiment, we investigate the ultrafast dynamics of the electronic correlations in a 1D Mott insulator ET-F_2TCNQ while its molecular vibrational mode is being perturbed. Figure 6.12 (a) shows the intensity spectrum of the mid-infrared pump pulse (in orange) overlapping the ET vibrational mode (in blue) along c-axis at 1000 cm^{-1}. Clearly, this mode is well isolated from the other vibrations and our narrow pump with FWHM of 115 cm^{-1} resonantly excite 10 μm mode without any overlap with other vibrations. The broadband near-infrared laser pulses polarized along *a-axis* (the green shaded region in figure 6.12 (b)) are used to observe the changes in CT band of ET-F_2TCNQ (black line in figure 6.12 (b)). It entirely covers the CT band, starting from 4600 cm^{-1} to 7950 cm^{-1}.The electric field of the pump and the intensity profile of the probe pulses are shown in figure 6.12 (c) and (d) respectively. The FWHM of the probe pulse is 10 fs and they can measure upto 3 points within the 33 fs long single oscillation cycle of the pump electric field and the changes induced by it.

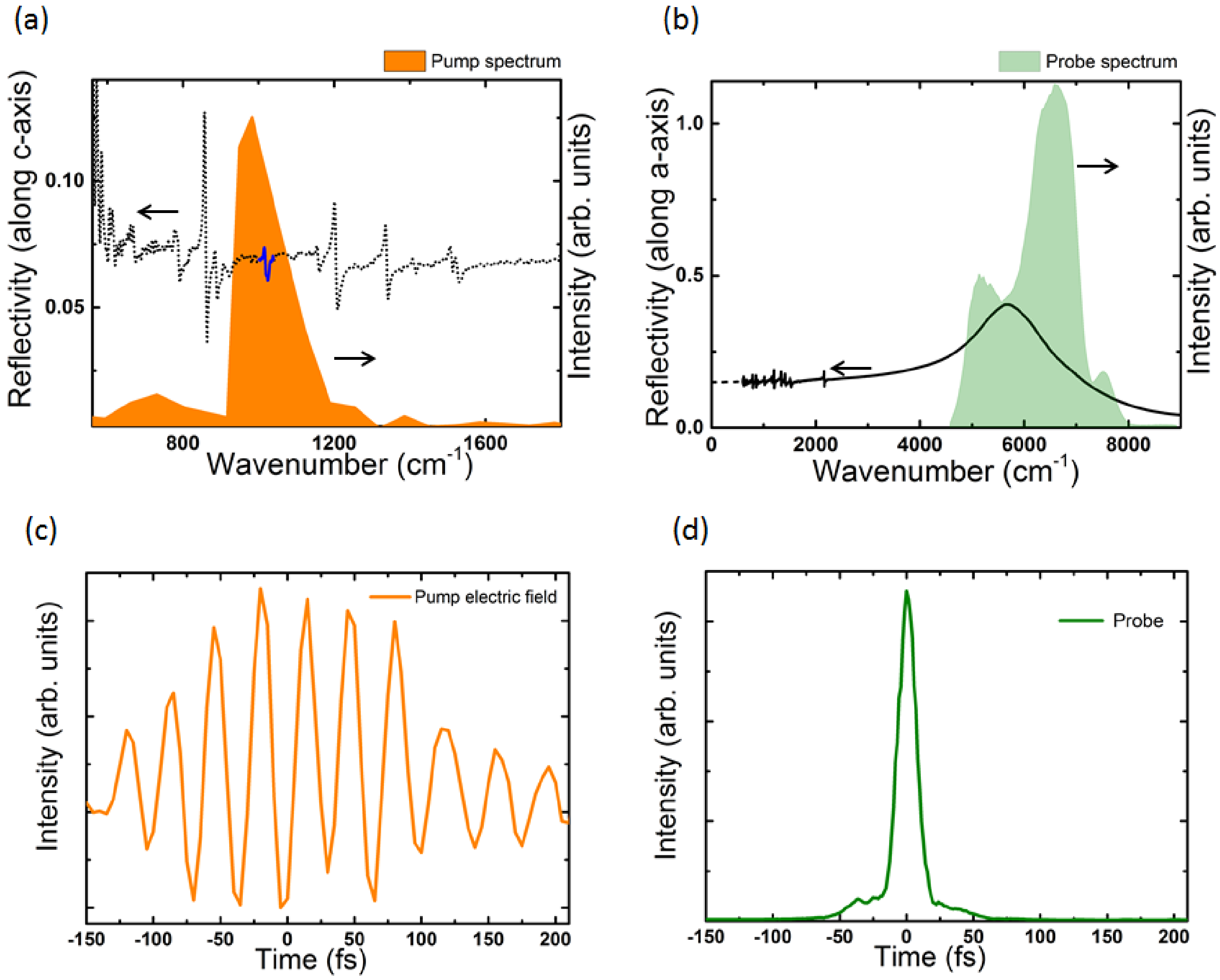

Figure 6.12: (a) (orange) Spectrum of the mid-infrared excitation pulses centered at 1000 cm-1 (10 μm wavelength) resonant to the ET molecular vibration mode (blue). The sample reflectivity in direction perpendicular to the c-axis is shown in dashed black line. (b) (Green) The spectrum of the near-infrared probe beam covering the charge transfer band centered at 5500 cm^{-1} along a-axis. (c) Phase locked electric field of the mid-infrared pump pulse measured via electro-optic sampling (d) Intensity profile of near-infrared probe pulses.

6.5 Photo-vibrated changes in the charge transfer band

Figure 6.13 shows the spectrally integrated time-resolved reflectivity changes $\Delta R/R$ across the CT band in ET-F$_2$TCNQ at room temperature. A pump fluence of 0.9 mJ/cm^2 is used for the measurement. As the pump excites the sample, the reflectivity decreases and within 100 fs reaches a minimum of approximately 4% (green curve). The driven

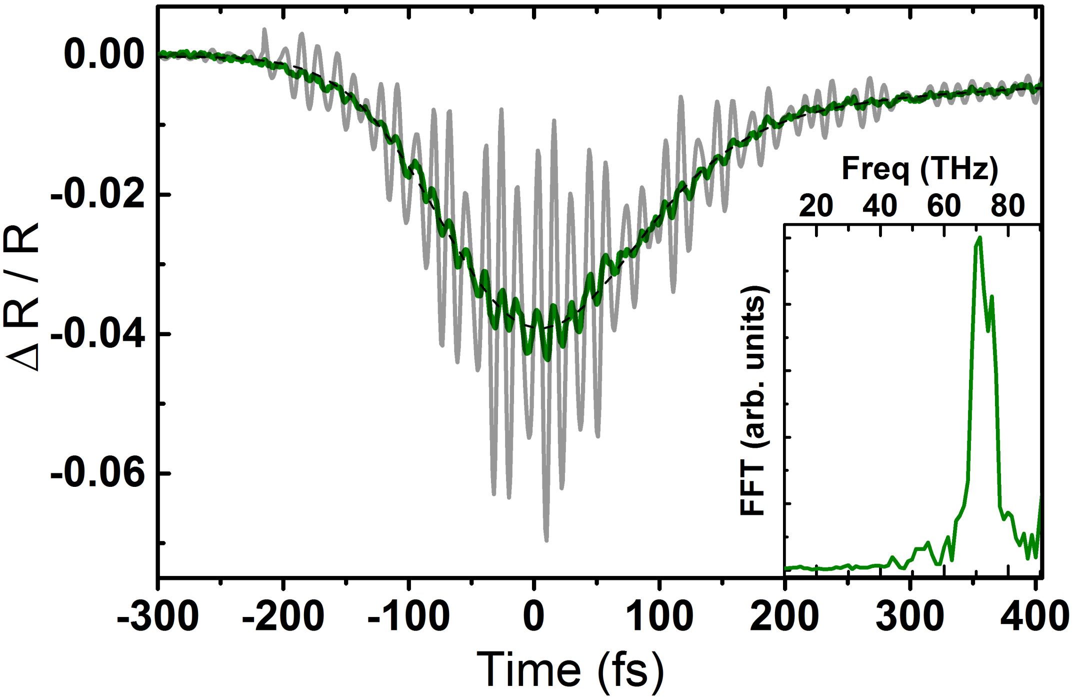

Figure 6.13: (Green) Spectrally integrated time dependent reflectivity changes in ET-F_2TCNQ at a pump fluence of 0.9 mJ/cm^2 at room temperature, together a double exponential fit in dashed black. The grey solid line shows the deconvolved reflectivity changes. The inset shows a Fourier transformation of the measured deconvoluted oscillations, peaking at 70 THz.

state relaxes back by 90 % in next 400 fs. The fast relaxation time reveals that the molecular vibrational driven changes are different from the usual slow lattice modulated effects [13, 14]. The longer decay times for the latter case is due to inter related relaxation channels available to the lattice compared to the molecular site. The experimental curve is fitted with an error function for the falling edge and a double exponential decay function (dashed black line) for the recovering dynamics given as:

$$\frac{\Delta R(t)}{R} = A * erf(1 + \frac{t}{t1}) * (A_1 e^{-t/\tau_1} + A_2 e^{-t/\tau_2} + constant) \qquad (6.1)$$

The reduction in reflectivity suggests that some spectral weight transfer from CT band to mid-gap absoption band as described by Kaiser et al. [18]. The relaxation of the excited CT bands is accompained by two channels. The fast decay constant τ_1 = 45 fs is obtained for the trailing edge of the pump pulse and is attributed to the direct relaxation of the excited molecular mode. It is followed by a slower exponential decay constant τ_2 = 500 fs and is attributed to thermalization of the hot mode via phonon-phonon coupling. This involves the low frequency phonon modes in THz range and likely to be dictated by their lifetime and hence occurs on the time scale of hundreds of femtosecond.

Remarkably, fast oscillations are superimposed to the overall reduction of $\Delta R/R$. The Fourier transform of the oscillations shows a peak at approximately 70 THz (see inset of figure 6.13). The oscillations have an amplitude of 0.7 %. Notably, this observed frequency is approximately double the frequency of the driving field (at 30 THz). The optical conductivity response do not show any possible Raman mode at 70 THz frequency. The quadratic modulation of the CT peak with respect to the displacement coordinate of ET molecule therefore is likely to be associated with the variation of on-site correlation term with quadratic dependence described in the previous chapter.

Since the oscillations detected have time period of 14 fs and are comparable to the probe duration of 10 fs, the overall response can be expected to be smeared. The response is convoluted with the width of the probe pulse and therefore reduced in the peak amplitude. To have an estimate on the amplitude of the oscillations, we employ the deconvolution analytical method and extract the response [1]. The deconvoluted data is shown in grey in figure 6.13. Clearly, the oscillation amplitude is as big as 4 % and is on the same order as the overall reduction in reflectivity. The electric field of the mid-infrared pump not only induced a change in the charge transfer reflectivity but also led to the appearance of high frequency modulation at approximately twice the driving field. The integrated response already shows features that are in agreement with the previous experiment by Kaiser et al [18]. Also the 2ω oscillations are in agreement with the picture in figure 6.1 presented before.

Figure 6.14 (a) shows the spectrally integrated reflectivity change for various pump fluences measured. The amplitude of the $\Delta R/R$ shows a linear increase with the pump fluence with a threshold of approx. 0.4 mJ/cm^2 (figure 6.14 (b)). The fast Fourier transform is shown in the lower panel of the figure. For the low fluences , the 2ω response is prominent. At the highest measured fluence of 4.2 mJ/cm^2, a highly non-linear phonon spectrum is observed with weaker 2ω peak. This response was not analysed any further.

---

[1] Deconvolution of the data is done in the Fourier space. If 'R' is the resultant output, 'O' is the original signal and 'p' is the intensity envelope of the probe pulse in time domian, then R can be written as the convolution between the later two functions, then $R = O \otimes p$, where $\otimes$ is the convolution function. In Fourier space, the equation reads as $F(R) = F(O) . F(p)$ and hence $\Rightarrow O = \text{ifft}\ (F(p) \ / \ F(R))$

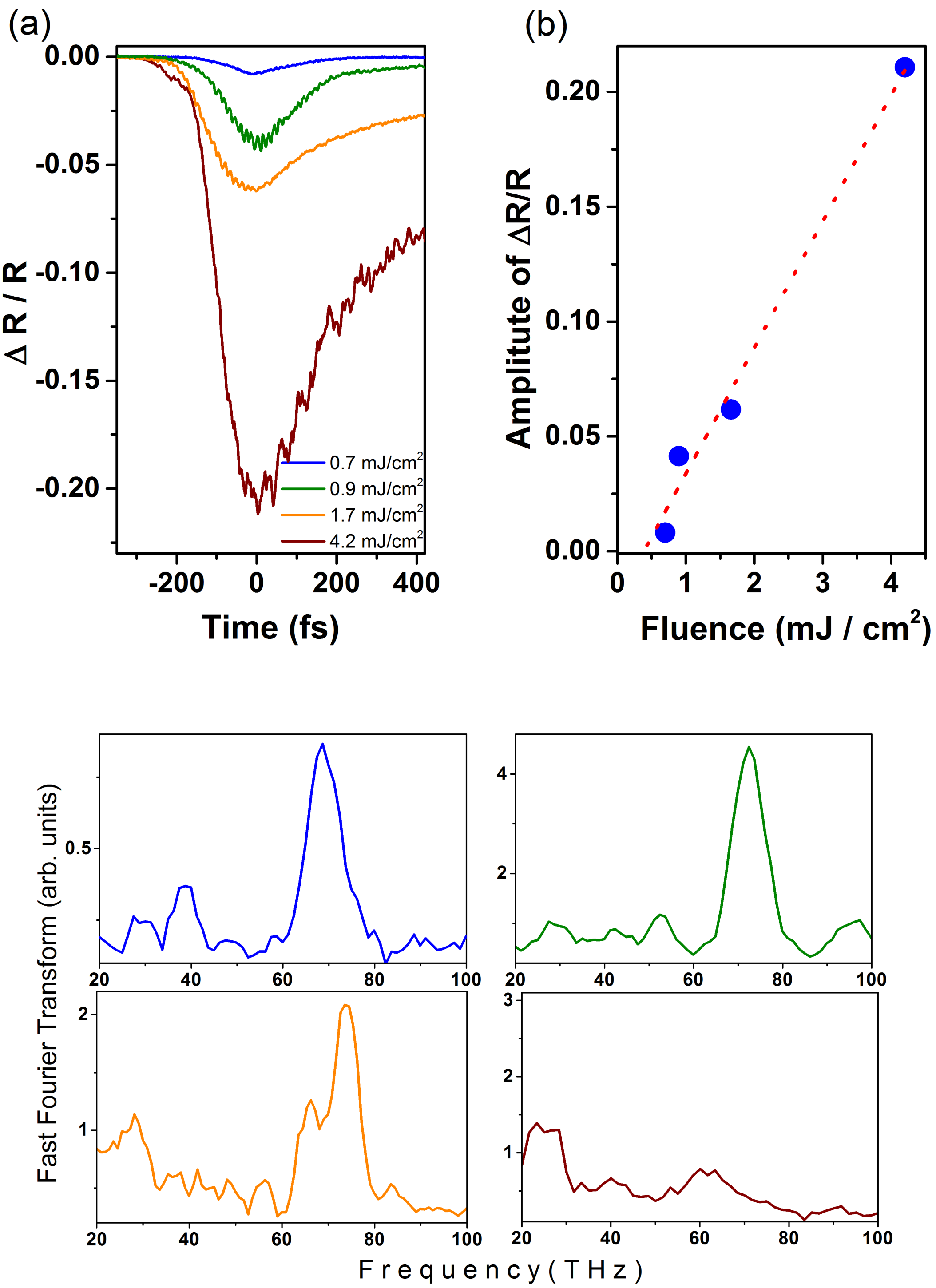

Figure 6.14: (a) Spectrally integrated time dependent reflectivity changes in ET-F_2TCNQ at various pump fluences at room temperature (b) Amplitude of reflectivity change as a function of pump fluence (in blue circle), together with a linear fit (in dashed red line). Below are the fft for each fluence curve.

6.6 Spectrally resolved photo-excited dynamics

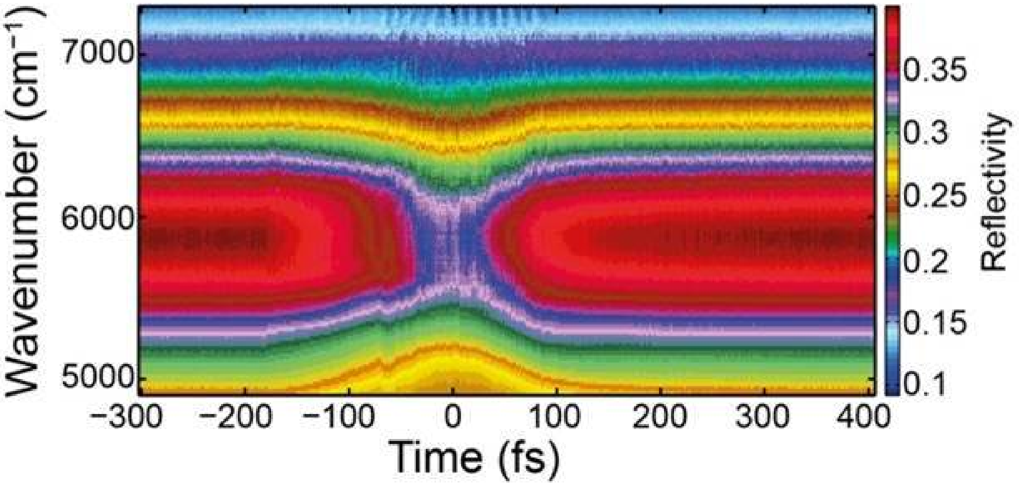

Figure 6.15: (a) Frequency resolved change in reflectivity as function of time in 1D Mott insulator ET-F_2TCNQ at room temperature.

Additional information on this dynamics can be accessed through the analysis of its spectral features. To really prove the quadratic picture conjectured, we performed a spectrally-resolved pump-probe measurement under the same experimental condition of temperature and pump fluence. A gated spectrometer[2] was used for the detection of the frequency resolved changes in the probe pulse. The frequency and time dependent reflectivity is shown in figure 6.15. Three observations can be made from the colored plot:

- There is a reduction in the total reflectivity. The peak reflectivity decreases from 0.4 to 0. 33 absolute value.

- The reflectivity peak shows a red shift of approximately 70 cm^{-1}.

---

[2] A gated spectrometer can be gated in time. A waveform generator is used to generate a rectangular waveform in syncronization with the laser pulse. It forms a rectangular waveform completely covering the laser pulse and otherwise stays zero. This information about the arrival of the pump pulse is sent to the gated spectrometer. It then registers the spectral data within the time of the waveform as the pump-on signal and hence pump-induced changes in the probe. For rest of the time, the data corresponds to pump-off and hence unperturbed probe.

- Crucially, the oscillations at 70 THz frequency are observed in CT band and the response is in agreement with the spectrally integrated diode measurements.

The observed reduction in the CT amplitude and the shift of the CT peak comes from the same physics associated with the appearance of the side band in Kaiser et al. paper [18]. The redshift is smaller owing to less fluence compared to ref. [18] . It is likely related to the reduction of the effective U (see section 5.5). A red shift implies that the energy required to make the charge transfer across the ET molecules has transiently reduced. The fast oscillations are spread across the whole of the CT band.

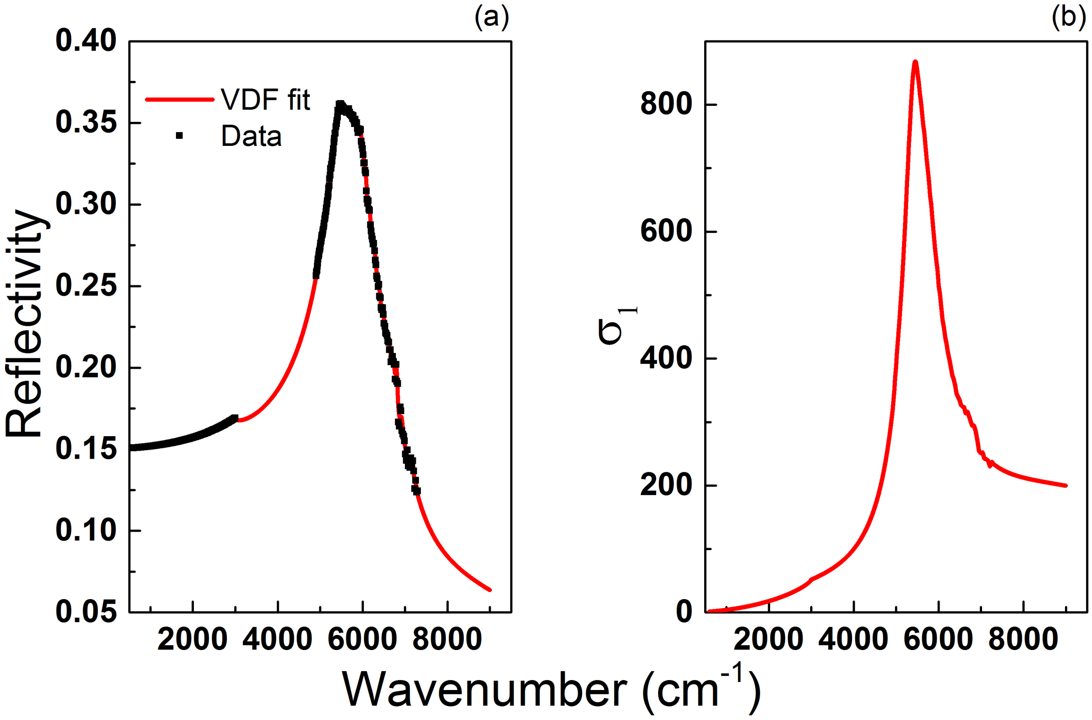

Figure 6.16: (a) The static reflectivity from 600 - 3000 nm (black line) stitched to experimental time dependent reflectivity from 4900 -7300 nm (black squares). The red line is the VDF fit to the complete spectral range. (b) The optical conductivity extracted from the reflectivity using VDF function.

To understand the role of the microscopic parameter behind the salient features in the reflectivity, we extract the optical conductivity for all time delays, from the collected reflectivity spectrum, applying Kramers-Kronig (KK) consistent variational dielectric function (VDF) fit [166]. Our acquired reflectivity is in the frequency range from 4900 cm^{-1} to 7300 cm^{-1}. The static reflectivity data from 600 cm^{-1} to 3000 cm^{-1} is merged to the measured frequency range under the assumption that there is no change in that low energy spectral region (see figure 6.16 (a)). To this spectral range, variational dielectric function fitting is done using a software RefFIT by Kuzemko[166] allowing to extract in a model independent way, the KK consistent optical conductivity response in the narrow frequency range (see figure 6.16 (b)). Drude-Lorentz oscillator model is only used as the first approximation in VDF. The central idea of this fitting procedure is that for each experimental point, an oscillator is assigned. The purpose is not on the value of parameters associated to the oscsillator, but to calculate the complex optical conductivity. This method is a universal approach, applicable to even off-normal angle of incidence data, reflectivity from layered samples and small experimentally available frequency range as is the case with us.

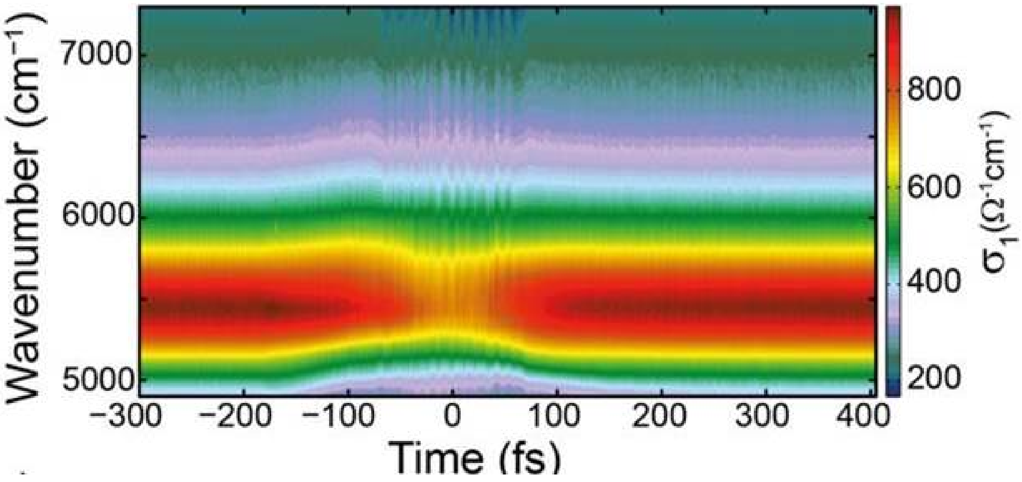

Figure 6.17: The optical conductivity extracted from the reflectivity using Kramer-Kroning consistant variational dielectric fits.

The retrieved time-dependent optical conductivity spectrum retains all the features of the reflectivity plot and is shown in figure 6.17. Fast oscillations at 70 THz are found, in addition to the amplitude reduction and red shift of the CT band. We gain further insight by fitting the transient conductivity spectra for each time and identify the Hubbard parameters responsible for 2ω response, in the simple framework of extended Hubbard model (eq. 2.2). We extract parameters effective Mottness U/t and effective inter-site interaction term V/t as a function of time dictating the dynamics of CT resonance.

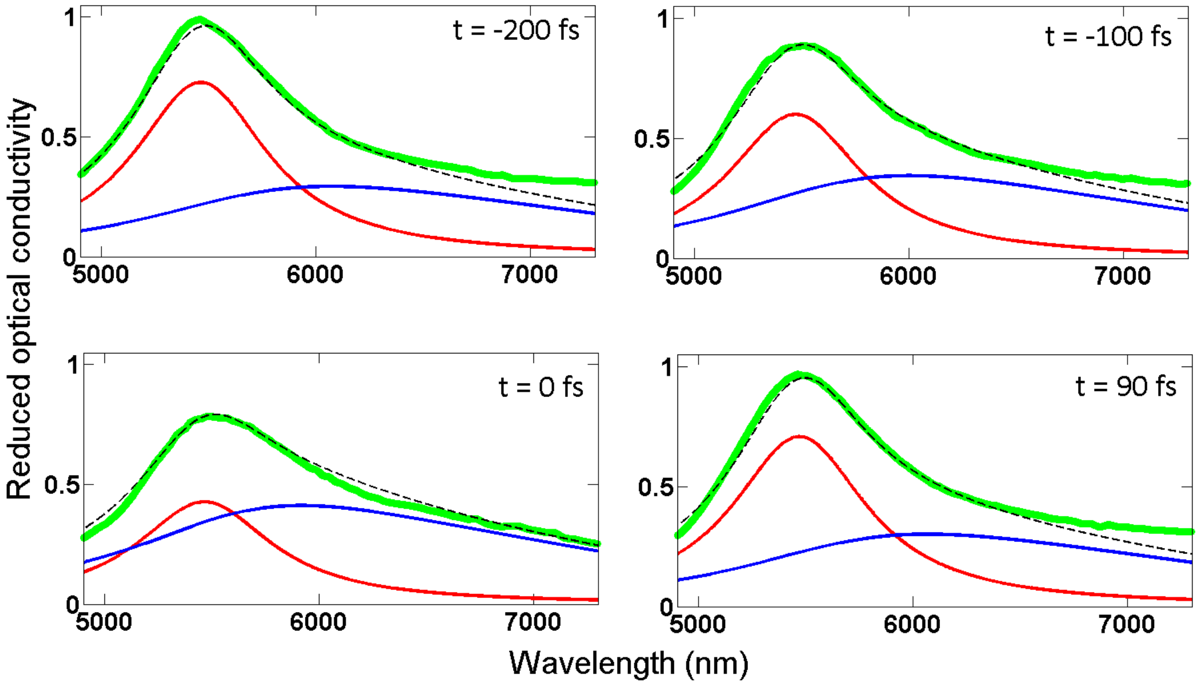

Figure 6.18: Reduced optical conductivity (in green) with model fit (dashed black) on top at various pump-probe time delays. Red and blue are the corresponding HD and PH continuum extracted from the fits.

6.6.1 Fitting of Mott gap

The changes in the charge transfer resonance are due to the changes in the correlations. To extract the contribution of the excitons and the interaction parameters U, t and V, we use the analytical model based on the extended Hubbard model. Like in the equilibrium case (see section 5.2.3), the fit to every snapshot in the transient response also allows a good description of the experimental data. For the fits, we have considered t to be constant as it is influenced by spacing between the molecules which to leading order is not modified by excitation of the local on-site molecular mode. Figure 6.18 shows the fits from the model in dashed line to the reduced optical conductivity in green at various times = -200, -100, 0 and 90 fs. The model yields a good fit to our experimental CT curve for all the time delays. As we learned in the previous chapter, the CT resonance is attributed to two configurations: holon-doublon pair and particle-hole continuum. The model filters out both the conributions coming from HD and PH continuum shown in red and blue line respectively in figure 6.18. With the vibrational driving, we observe that the HD peak reduces in amplitude and PH peak shows an increase. This point towards the dominant delocalization holon-doublon physics.

In addition to the modulation of the amplitudes, a fast oscillation of the response is observed along the frequency axis. The peak of both the HD and PH continuum oscillates in frequency position. To visualize this effect better, we plot individually normalized HD and PH as shown in figure 6.19. Evidently, the exciton peak stays almost centered to its steady state value given by U - V - 4 t^2/V = 5460 cm^{-1} and shows fast oscillatory component at frequency of 70 THz. On the other hand, the PH continuum peak (centered at $U_{equilibruium}$) shows red shift and oscillates too at 70 THz. Qualitatively, this hints that the reduction and oscillations are originating from the corresponding reduction and oscillation in the on-site Hubbard U.

To investigate better the periodicity of the transient changes induced by the pump, line cuts of individually normalized HD and PH contributions at time interval of one-fourth of the time period T of the pump electric field (*i.e.* at interval of approx. 8 fs) is shown in figure 6.20. Time 0, T/2, T represents the zero point of the electric field and time T/4, 3T/4 etc represents crest and trough respectively. For half the cycle of the electric field of pump *i.e.* from 0 to T/2, both HD and PH complete one complete oscillation in frequency. We find that the peak positions of both HD and PH goes back and forth in frequency by 35 cm^{-1} (4 meV) and 93 cm^{-1} (12 meV) wavenumbers respectively every T/4 interval. From the analytical model, we know that the peak positions of both PH and HD are dominated by U. In fact, the peak of the PH continuum is at Hubbard U and of the HD continuum is at U-V-4t^2/U $\simeq$ U. The oscillations of the peak position at 70 THz strongly point towards the 2ω modulation of U under the on-site molecular vibrational excitation at ω.

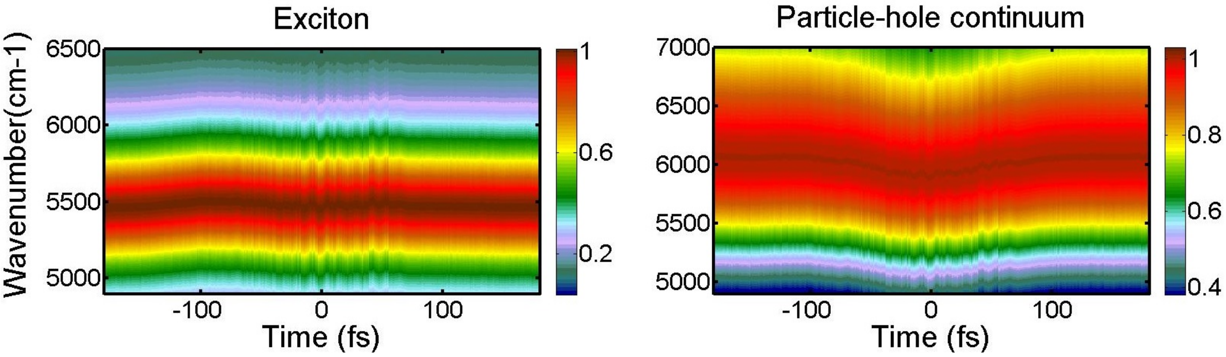

Figure 6.19: Normalized reduced optical conductivity contribution from (a) holon-doublon (b) particle-hole continuum

We report on the value of microscopic parameters U/t and V/t extract from the fitting of the optical conductivity (as done for the static data in section 5.2.3) [19]. We

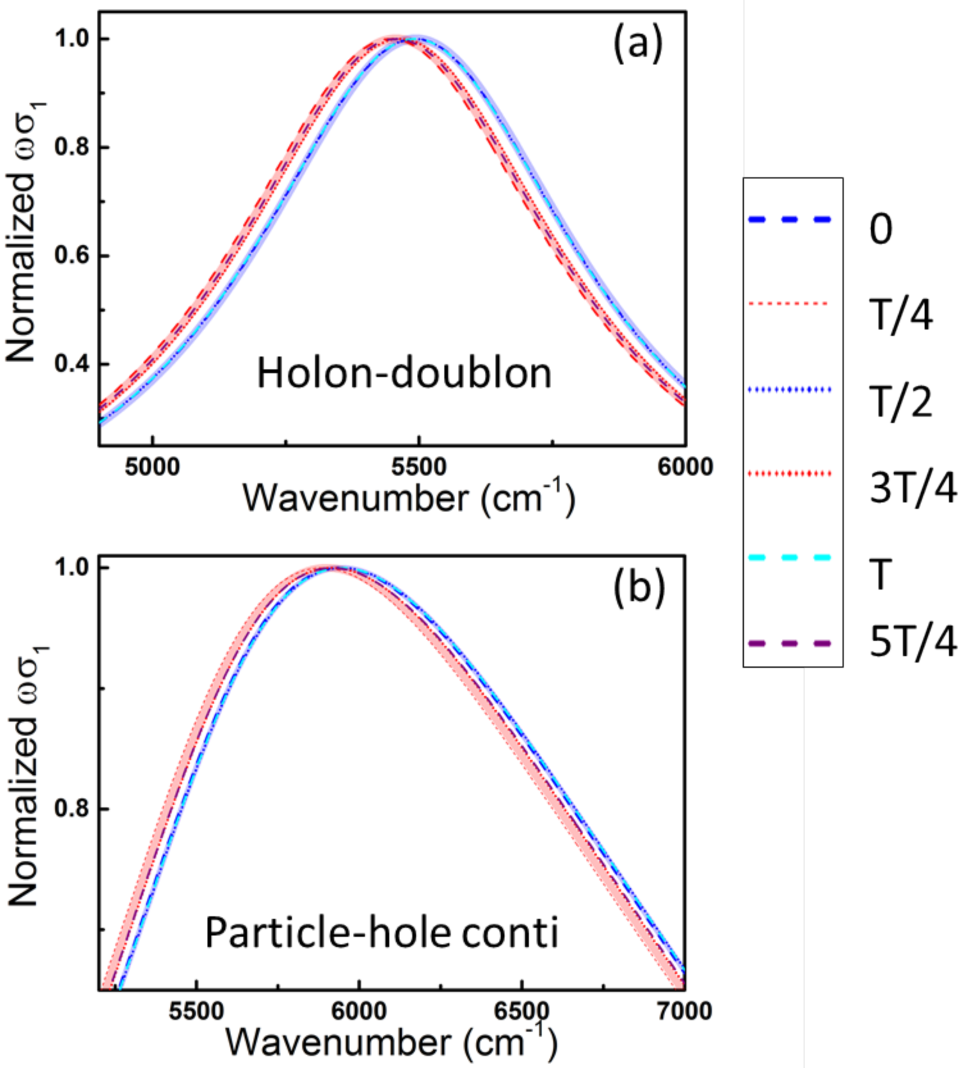

Figure 6.20: Normalized reduced conductivity from (a) holon-doublon contribution (b) particle-hole continuum for time corresponding to the crest and trough of the pump electric field of time period T (see figure 6.1 for pump electric field).

plot the effective on-site correlation term U/t and the inter-site interaction term V/t as a function of pump-probe delay time (figure 6.21 (a) and (b)). We have two effects: (1) The overall reduction of U/t and V/t (2) On the top, we have 2ω oscillation on U/t. The Fourier transform of U/t shows peak at 70 THz, whereas V/t has rather flat Fourier transform (see figure 6.21 (b) and (d)). The 2ω oscillation is due to the quadratic coupling of the effective Mottness U/t to the displacement coordinate of the driven molecular mode. The reduction in U/t is due to the fact that the orbital wave function is enlarged in the driven state, thereby reducing the charge density on the ET molecule.

The effective correlation U/t is exclusively coupled to the molecular displacement coordinate. In principle, all the microscopic parameters (U, V and t) are entangled. Though we cannot distinguish t independently, but it is clear that t is not dominating the 2ω oscillations since the distance between the ET molecules do not change on molecular vibration. Remarkably, the molecular vibrational pumping coherently modulated only U. If V was modulated, one would likely see oscillations in V/t, which we do not see here. We claim the dynamical modulation of the effective Mottness is the reason towards the observed experimental 2ω oscillation. Other possibilities like that of change in half-filling can be convincingly discarded (see Appendix A.3). While driving a local mode, the molecular spacing is not modulated, however the time average of orbital wavefunction changes and therefore V/t shows a change in average.

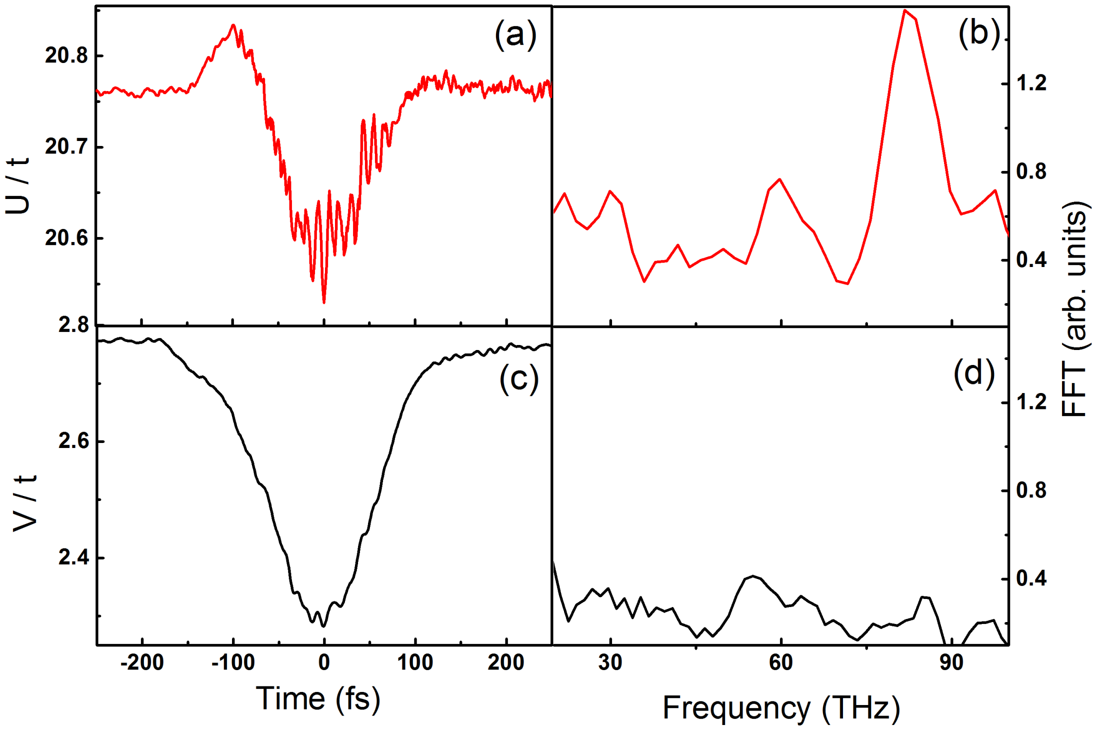

Figure 6.21: (a) and (b) Effective Hubbard correlation term U/t and V/t extracted from the fits as function of pump-probe delay time (c) and (d) with their respective fast fourier transforms

The 70 THz oscillations are a little higher than twice the excitation frequency of 60 THz. Second order effects might be playing role, which is beyond the considerations discussed in equation 5.3. If the duration of the laser pulse is shorter than the time period of the phonon, it can drive the phonon to oscillate with different frequency, resulting in squeezing of the vibrations [167, 168]. One can investigate such phonon squeezing by various methods like that of x-ray diffraction. No attempts were made to explore such possibilities in this work.

So far, we used the model which was for equilibrium state of ET-F_2TCNQ and showed with the time independent model, the variation of U/t and V/t by fitting the charge transfer curve for each time. Whereas the process under study is certainly not in equilibrium, hence the need for studying real time dynamics. For a full description of the effect we observe, a time dependent current-current correlations has to take into account the evolution of all interactions. We now substantiate our claim, taking aid from two-time current-current correlations of a simple model (see figure 5.12 (b)) and calculate reflectivity and optical conductivity when U/t and V/t vary in time in a way similar to that exposed by the fitting to the experiment. All this is discussed in the next section.

6.7 Simulations

A numerical simulation of time dependent optical conductivity for the excited state ρ is done using the two time current-current correlation function $c_{jj}(\tau,T)$, where T is the pump-probe delay time. These further supports our claim of 2ω modulation of U/t.

The vibrational oscillations are considered to change the coordinate described by $q_j(\tau) = q_0$ [sin $(\omega_{IR}\tau + \phi)$], where q_0 is the amplitude of the displacement and ϕ is its phase. The resultant quadratic modulation of U together with overall gaussian evelope is considered and is given by

$$U(\tau) = U\{1 - A_U e^{-(\tau-\tau_P)^2/T_P{}^2}[1 - P_0 q_{IR}{}^2(\tau)]\}$$

where τ_P and T_P are center and width of the pulse in accordance with the experimental value and A_U is the overall decrease in amplitude in accordance to the fits to the experimental observation. P_0 is the amplitude of the oscillations of U around the overall envelope. The width and amplitude of the gaussian envelope and amplitude of the oscillations are extracted from the fit to figure 6.21 (a). Similarly, for V, a simple gaussian envelope is employed with its parameters similar in figure 6.21 (b). These input time dependent parameters for the simulations is shown in figure 6.22 (a) and (b).

For non-equilibrium condition, the two time current-current correlation function is needed. Two time coordinates τ and $\tau^{'}$ includes the time dependent variation of the on-site Coulomb interaction due to molecular vibrations. The expression is the form as [134, 151, 169]:

$$\chi_{JJ}(\tau,\tau^{'}) = \langle 0|\hat{U}^{\dagger}(\tau+\tau^{'})\hat{J}\hat{U}(\tau+\tau^{'})\hat{U}^{\dagger}(\tau^{'})\hat{J}\hat{U}(\tau^{'})|\rangle \tag{6.2}$$

We use the effective model of Hamiltonian given below to dictate the time map of $\hat{U}$.

$$H = (U-V)|0><0| + U\sum_{l=1}^{l}|1><1| - 2t\sum_{l=0}^{l-1}(|l><l+1| + |l+1><l|).(A2) \tag{6.3}$$

where l=1,2,3,...L For more details on two time current-current correlation function, see [170].

Figure 6.22 (a) and (b) shows the U/t and V/t assumed for the simulations and the resultant optical conductivity color plots obtained with two-time current-current correlation function simulation (figure 6.22 (d)). The reflectivity is retrieved applying KK-consistant VDF fit to the optical conductivity simulated data (figure 6.22 (c)). The plots are in good agreement with the one obtained experimentally (see figure 6.15 and

6.17). Clearly, the coherent modulation of U/t manifest itself macroscopically as the charge transfer oscillation of the reflectivity.

To discard the oscillations in V/t, similar simulations are done with input of U/t and V/t as shown in figure 6.23 (a) - (b). Here U/t is given as a function form of the time dependent gaussian envelope and V/t is function of a gaussian envelpe along with fast oscillation at 2ω on top of it. The resultant conductivity plot and the retrieved reflectivity plot is shown in figure 6.22. They are visually very different from the one obtained experimentally (figures 6.15 and 6.17). Thus, we can conclude that the modulation of U is the dominant contribution to the observed oscillations.

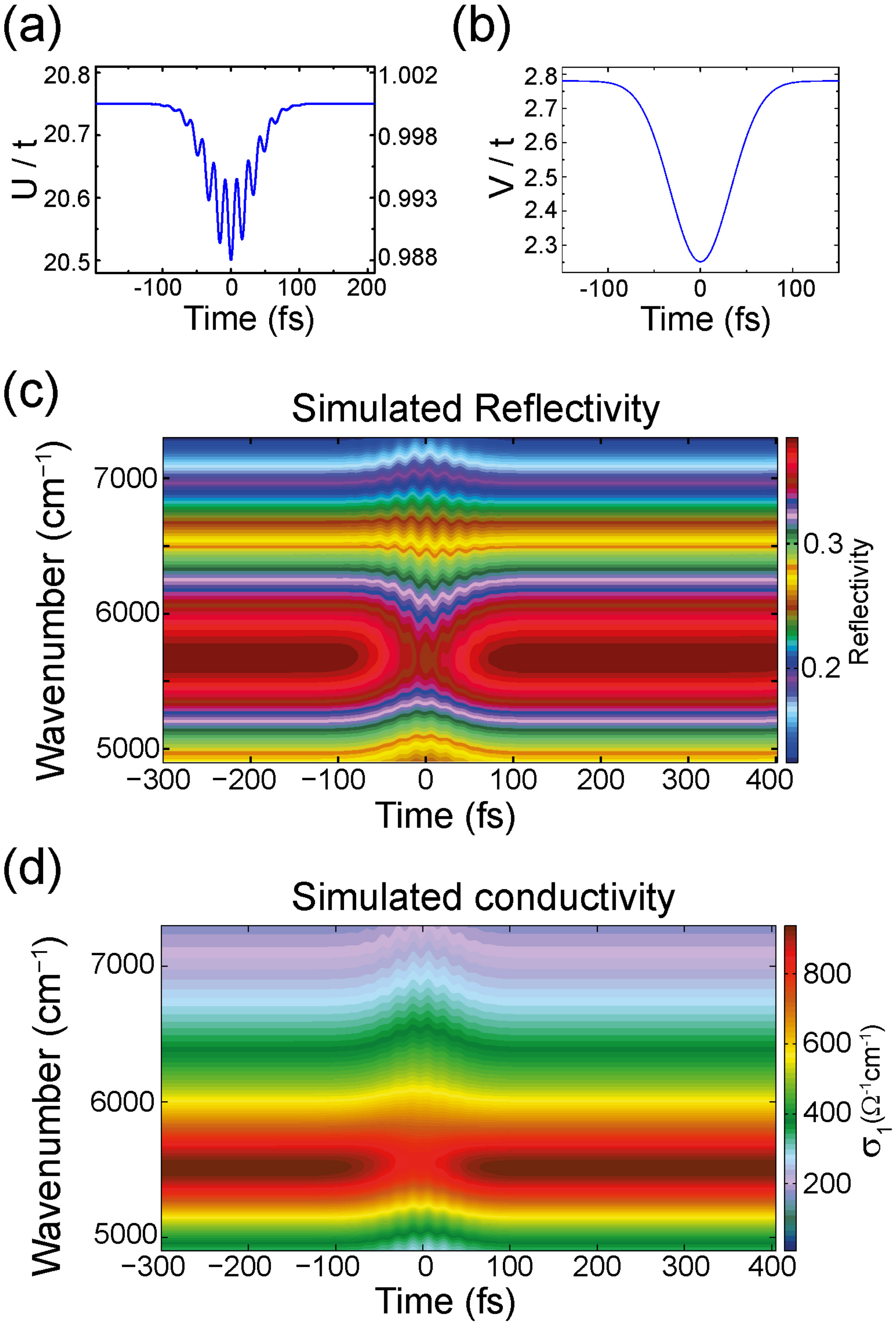

Figure 6.22: (a) Assumed variation of U/t over time for numerical simulation, similar to one obtained experimentally as in figure '6.21(a)' (b) Assumed variation of V/t over time for numerical simulation, similar to one obtained experimentally as in '6.21(c)' (c) Simulated reflectivity obtained via two-time current-current correlation function calculations of an effective strong-coupling model (d) Corresponding simulated conductivity

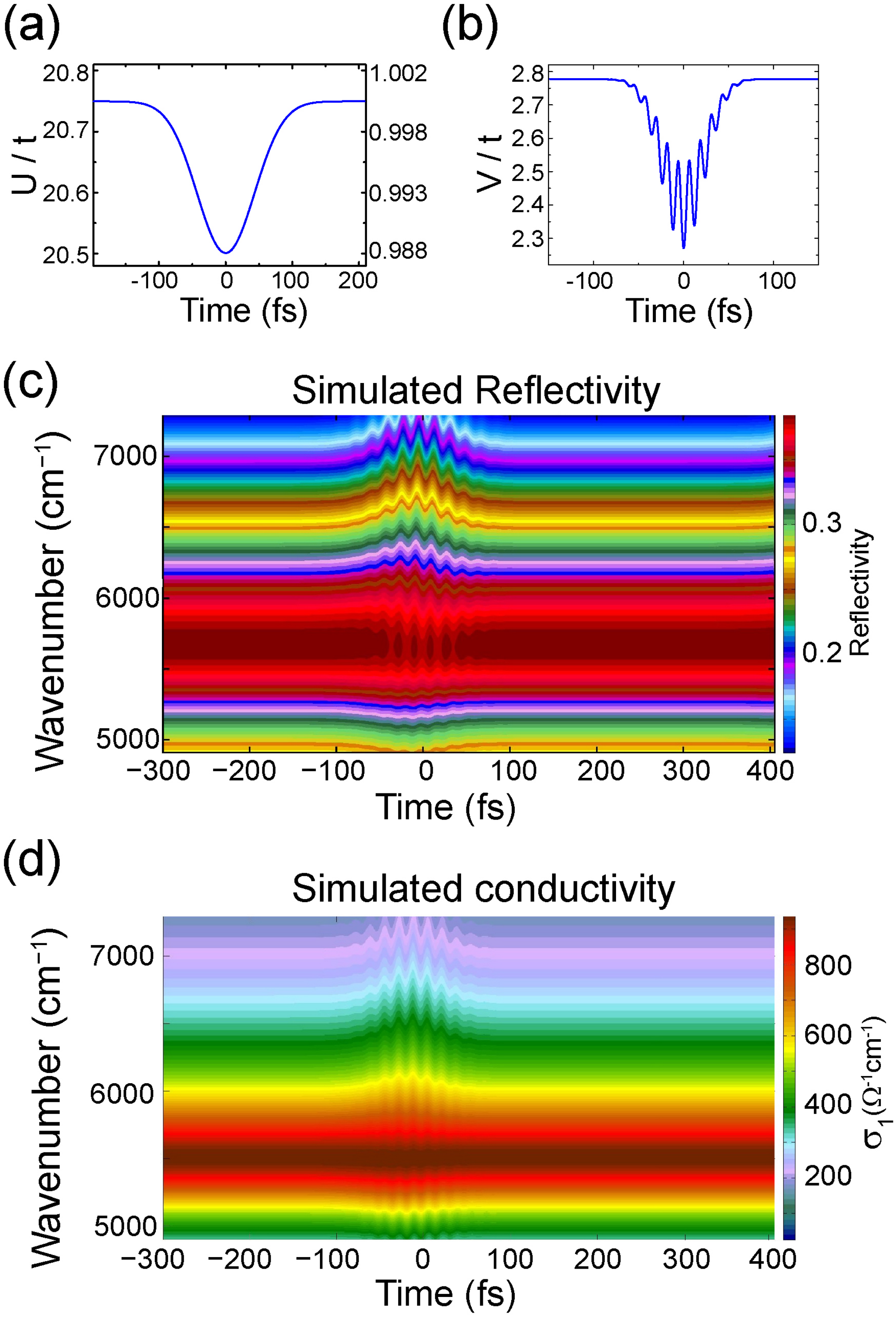

Figure 6.23: (a) Assumed variation of U/t over time for numerical simulation (b) Assumed variation of V/t over time for numerical simulation (c) Simulated reflectivity obtained via two-time current-current correlation function calculations of an effective strong-coupling model (d) Corresponding simulated conductivity

6.8 Summary

The chapter demonstrates a direct way to control on-site correlation term via vibrational molecular excitations. Phase-stable electric field modulates the electron charge densities of ET molecule in the molecular compound ET-F_2TCNQ. This change manifest itself in the quadratic response of the effective electronic interaction U/t. The charge transfer band with hidden information on the microscopic parameters U/t and V/t is interrogated with spectrally overlapping probe pulses on the time scale of oscillatory time period of the molecule. The spectrally integrated measurements show the reduction of the CT band superimposed by oscillations at twice the driving frequency and of the same amplitude as the gross reduction of the CT band. These oscillations also reported in the spectrally resolved measurements are rooted in the quadratic modulation of U/t. The analytical model based on extended Hubbard model and current-current correlations, aided the extraction of the parameters U/t and V/t from the experimentally retrieved reduced optical conductivity. Further, the claim is substantiated by the two time current-current correlation function simulations, where providing the time dependent variation of U/t and V/t are similar to obtained in experimental data analysis, repoduces to great extent the refectivity and conductivity spectrum.

7 Conclusions and outlook

7.1 Conclusions

The work presented in this thesis has established the importance of ever shortest time scale across the visible and near-infrared regions of the spectrum to gain new insights into the ultrafast dynamics of electronic interactions in correlated systems. While an optical stimulus is perturbing the system, thereby triggering electronic or molecular motions, the induced changes in the electronic correlations are captured on their inherent time scales. Taking this movie of electronic dynamics requires two technically challenging ingredients that were both implemented within this thesis.

- Ultrashort few-cycle or even single-cycle probe pulses in the near-infrared and visible spectral range, capable of delivering sub-10 femtosecond time resolution.
- Phase-stable mid-infrared pulses to coherently drive molecular motions with a fixed phase of the atomic oscillations.

Using these state-of-the-art techniques, the following scientific results were achieved.

7.1.1 Orbital dynamics in Manganites

We find a structural bottleneck in the ultrafast photo-induced melting of orbital order in the half-doped manganite $La_{0.5}Sr_{1.5}MnO_4$, a prototypical transition metal oxide. The orbital order, present at half-doping and low temperatures, shows partial reduction on the time scale longer than the full width half maximum of the excitation pulse. If the orbital ordering had mainly originated from the electronic interactions, one would expect it to melt on time scales characteristic of electronic distortions, *i.e.* as rapid as the stimulus. The delay found in the melting suggests that the photo-induced state is not driven by the carrier injection but occurs through a slower structural degree of freedom. We also found few cycles of coherent lattice oscillations associated to high-frequency Jahn-Teller distortions. Crucially, the excitation of this mode requires a threshold in the excitation fluence, contradicting the convensional mechanisms of coherent phonon excitation. This result highlights that the coherent motions are triggered above a sufficiently high fluence by a cooperative lattice-orbital response. The early time dynamics accessible with few- femtosecond pulse durations allowed us to shine light on the fundamental microscopic physics in manganites to establish the role of the structural distortion behind the orbital ordered state.

7.1.2 Dynamics of 1D Mott insulator

In an organic Mott insulator ET-F_2TCNQ, we establish coherent control of local Coulomb correlations by exciting a local molecular mode. This insight has become possible by the development of a special optical apparatus, in which the absolute phase of the molecular vibrations is stabilized through the phase-stable excitation and the electronic response is probed on a sub-cycle time scale with 10-fs near-single cycle probe pulses in the infrared. The vibrational perturbation modulates charge densities at the ET molecule site, thereby changing the electronic screening and hence the effective on-site Coulomb interaction U/t. The charge transfer band shows a reduction and oscillations at twice the frequency of the driving field, which manifest in the coupling of effective correlation to the displacement coordinate (q) of the excited molecule *i.e.* q^2U form .

The choice of the molecular crystal with negligible electron-lattice interaction and one-dimensionality allowed us to make use of model Hamiltonians for the theoretical understanding. The analytical fits to the frequency resolved optical data, based on the extended Hubbard model evidence the variation of U/t at approximately twice the frequency of the driving field. The simulations using the time-dependent current-current correlation function, which consider the time evolution of the electronic parameters U/t and V/t could mimic the experimental reflectivity and conductivity non-equilibrium response. This experiment establishes the control of on-site electronic interactions, Hubbard U and the realization of a dynamic Hubbard model in a strongly correlated molecular solid.

7.2 Outlook

We report substantive progress made in our quest to coherently control and understand complex, correlated electron solids using ultrashort laser pulses.

In transition metal oxides like the one studied for this thesis, further detailed understanding on the cooperative atomic motions involved in the photo-induced melting of the orbital order can be gained by time-resolved x-ray diffraction experiments carried out with highest time resolution in the sub-10 fs regime, which is nowadays accessible at free electron lasers.

On the other hand, electric field phase-stable mid-infrared pulses were used to modulate many-body correlation parameters, along the lines of what is achieved in cold gases through the Feschbach resonance. The ultimate goal can be to enhance or reduce correlations in systems such as superconductors with strongly correlated electrons, in which pairing strongly depend on the many body phenomena. Other possibilities could be to employ pulse shaping techniques to the mid-infrared pulses [171] that may help to investigate the detailed dependence of the correlation parameters to the phase of the excited molecular mode.

The phase locked excitations can be extended to the few-THz regime as is shown by Vicario et. al. [172]. This recent work shows that a phase-stable THz stimulation of a cobalt film triggers magnetic dynamics that directly follow the THz excitation fields. Coherent transients in the low energy range coud also be explored with phase stable THz pulses in many body systems.

A: Ultrashort laser pulses generation

The generation of ultrashort laser pulses is possible today because of the advent of some solid state materials which show unique properties like high Kerr-coefficient used in the Kerr-lens mode (KLM) locking technique [173] and property like non-linear interactions with light used in optical parametric amplifications. Titanium:sapphire($Ti:Al_2O_3$) is the most widely used material as an active medium in oscillators and amplifiers, creating femtosecond laser pulses in near-infrared range. The amplifiers, using the concept of chirped pulse amplification are availabe commercially, generating few millijoule (mJ) pulse energy at 800 nm, 30 fs duration at 1 KHz repetition rate. However, Titanium:sapphire lasing material based on stimulated emission approach has a limited tunability, generating pulses around 800 nm wavelength. In section 4.3, we have presented a Titanium:sapphire laser system, with additional features of pulse broadening and compression with respect to the standard commercially available, generating broadband short pulses of duration down to 4 fs.

Other widely used solid state material is the β-Barium Borate (BBO) showing non-linear response to high intensity lasers (electric field of the order $\sim 10^8$ volts per meter) and used as a popular source for tunable and ultrashort laser pulses over a wide spectral range.

The first section of this chapter introduces second order non-linear processes, the optical parametric amplification method and difference frequency generation to generate broadband, ultrashort laser pulses followed by the self phase modulation (SPM) concept exploited in a broadband white light (WL) continnum. Finally, the last section brings insight onto pump-probe spectroscopy employed as a method to study the dynamical properties of our systems.

A.1 Optical parametric amplification

A.1.1 Second order optical non-linearity

The quadratic response by non-linear crystals to high electric fields revolutionized the field of photonics. To this end, let us consider a linearly polarized light at frequency ω and envelope A(z,t), propagating along z inside a crystal, whose electric field is given by

$$E(z,t) = A(z,t)exp^{j(wt-kz)} \tag{1}$$

Owing to the electric field, polarization is induced inside the crystal in accordance with the following relation

$$\begin{aligned} P(z,t) &= \chi^{(1)}E(z,t) + \chi^{(2)}E^2(z,t) + \chi^{(3)}E^3(z,t) + ... & (2) \\ &= P^{(L)} + P^{(NL)} & (3) \end{aligned}$$

The linear polarization term $P^{(L)}$=$\chi^{(1)}$E(z,t) dictates the processes like reflection, refraction, absorption and transmission. However, when a strong electric field is incident, the non-linear polarization terms start to play a role. All the processes dicussed under this section are consequences of the second-order non-linearity. We will consider $P^{(NL)}$ = $\chi^{(2)}$ $E^2(z,t)$ thereby, neglecting the higher order terms. We will now show mathematically how $P^{(NL)}$ acts a source term for variation of amplitude and frequency of the propagating beam and for the parametric amplification process in the next section.
In accordance with Maxwell's equations, the evolution of the electric field follows the equation

$$\frac{\partial^2 E(z,t)}{\partial z^2} - \mu_0 \frac{\partial^2 D(z,t)}{\partial t^2} = \mu_0 \frac{\partial^2 P^{(NL)}(z,t)}{\partial t^2} \tag{4}$$

where D(z,t) is the linear electric displacement field and μ_0 is the magnetic permeability of the vacuum. In the approximation of slow amplitude variation of electric field *i.e.* (d^2A/dz^2) $\ll$ (dA/dz) and using eq. 4, the double derivative of $P^{(NL)}$ with respect to time can be expressed as

$$\mu_0 \frac{\partial^2 P^{(NL)}(z,t))}{\partial t^2} = -2jk[\frac{\partial A}{\partial z} + \frac{1}{2j} D \frac{\partial^2 A}{\partial t^2} + \frac{1}{v_g}\frac{\partial A}{\partial t}] \tag{5}$$

where v_g is the group velocity (= $\partial\omega/\partial$k) and D is the group velocity dispersion (=$\partial^2 k/\partial\omega^2$). Clearly, the nonlinear polarization induces change in the shape of the envelope moving with velocity v_g.

Let us now consider the two linearly polarized beams at frequencies ω_1 and ω_2 (ω_1 > ω_2) going through the second-order crystal. They interact with themselves and with each other as shown in figure 1. The outputs are second harmonic of each wave at $2\omega_1$ and $2\omega_2$, the sum frequency generation (SFG) at ω_1 + ω_1 and difference frequency generation (DFG) at ω_1 - ω_2.

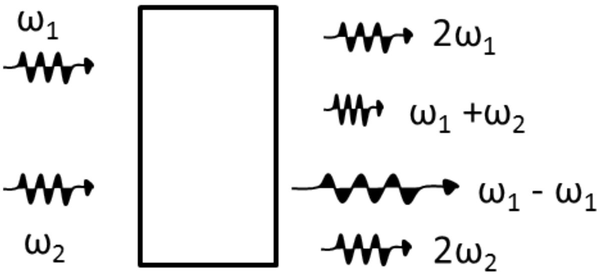

Figure 1: Second order polarization effect

A.1.2 Parametric Amplification

In order to understand the process of parametric amplification , which involves three frequencies, we now consider three monochromatic waves at ω_1, ω_2 and ω_3 such that $\omega_3 > \omega_2 > \omega_1$ and $\omega_3 = \omega_1 + \omega_2$. Their electric field can be written as:

$$E(z,t) = A_1(z,t)exp^{j(w_1 t - k_1 z)} + A_2(z,t)exp^{j(w_2 t - k_2 z)} + A_3(z,t)exp^{j(w_3 t - k_3 z)} \tag{6}$$

The source term can be written in simplified form as follows [174].

$$\begin{aligned} \Rightarrow \frac{\partial^2 P^{(NL)}(z,t)}{\partial t^2} =& -2\chi\omega_1^2 A_2(z,t) * A_3(z,t) * exp^{j(w_1 t - (k_3 - k_2)z)} + \\ & -2\chi\omega_2^2 A_1(z,t) * A_3(z,t) * exp^{j(w_2 t - (k_3 - k_1)z)} + \\ & -2\chi\omega_3^2 A_1(z,t) * A_2(z,t) * exp^{j(w_3 t - (k_1 + k_2)z)} \end{aligned} \tag{7}$$

Hence, the coupled non-linear equations can be written as:

$$\begin{aligned} \mu_0[-2\chi\omega_1^2 A_2(z,t) * A_3(z,t) * exp^{j(w_1 t - (k_3 - k_2)z)}] &= -2jk[\frac{\partial A_1}{\partial z} + \frac{1}{2j} D_1 \frac{\partial^2 A_1}{\partial t^2} + \frac{1}{v_{g1}} \frac{\partial A_1}{\partial t}] \\ \mu_0[-2\chi\omega_2^2 A_1(z,t) * A_3(z,t) * exp^{j(w_2 t - (k_3 - k_1)z)}] &= -2jk[\frac{\partial A_2}{\partial z} + \frac{1}{2j} D_2 \frac{\partial^2 A_2}{\partial t^2} + \frac{1}{v_{g2}} \frac{\partial A_2}{\partial t}] \\ \mu_0[-2\chi\omega_1^2 A_1(z,t) * A_2(z,t) * exp^{j(w_3 t - (k_1 + k_2)z)}] &= -2jk[\frac{\partial A_3}{\partial z} + \frac{1}{2j} D_3 \frac{\partial^2 A_3}{\partial t^2} + \frac{1}{v_{g3}} \frac{\partial A_3}{\partial t}] \end{aligned} \tag{8}$$

Optical parametric amplification is the technique involving transfer of energy from an

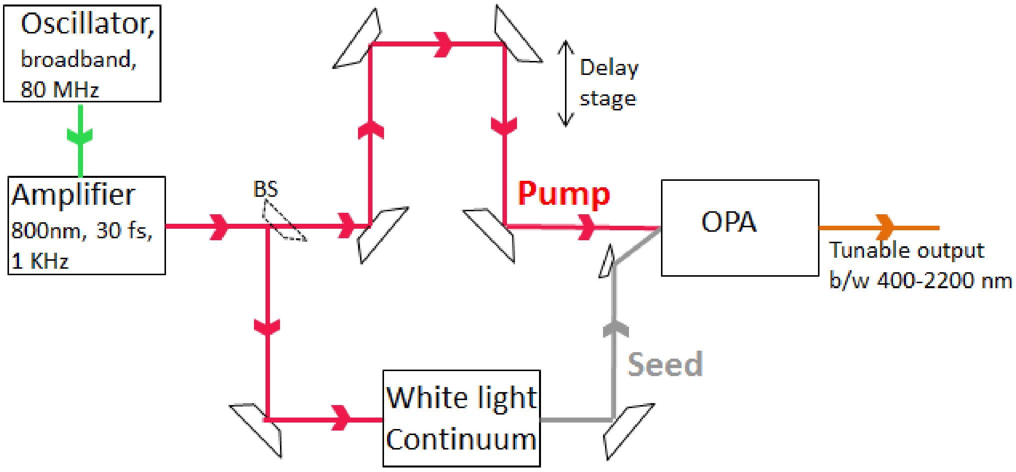

Figure 2: Schematic diagram for generation of ultrashort laser pulses using optical parametric amplification involving high intensity pump pulse and broadband white light seed pulse.

intense pump pulse to a white-light seed pulse in a non-linear crystal. Figure 2 shows a schematic of a typical setup for ultrashort pulses employing an amplification process. The mixing is possible under the condition that pump and seed overlap in space and time inside the crystal. For that purpose, a delay stage is necessary. The other condition is 'phase matching' discussed later in the section. Parametric amplification is a special case of DFG where the interacting fields differ in intensities by an order of magnitude or more. As shown in figure 3 (b), the high intensity pump beam at frequency ω_p puts the second order material to a virtual level $<1>$. The weak signal beam at ω_s dissociates the pump beam into another coherent pulse at ω_s, and the rest of the pump energy goes into the idler ω_i. Mixing of nearly same intensity beams is termed as DFG, which is commonly used for mid-IR generation as mentioned in section 6.3.

For the case of optical parametric amplification, assuming $\partial A \ / \ \partial t$ = 0 and $\partial^2 A \ / \ \partial t^2$ = 0 and using $\Delta k = k_3 - k_2 - k_1$, $\chi = \epsilon_0 \ d_{eff}$ and $n^2 = \epsilon_0 \ \mu_0$ and considering negligible depletion of pump at ω_3 (implementing A_3 can be treated constant) , the above coupled equations can be simplied to the following set.

$$\frac{\partial A_1}{\partial z} = -j\frac{d_{eff}\omega_1}{c_0 n_1} A_2(z) * A_3 * exp^{-j\Delta kz} \tag{9}$$

$$\frac{\partial A_2}{\partial z} = -j\frac{d_{eff}\omega_2}{c_0 n_2} A_1(z) * A_3 * exp^{-j\Delta kz} \tag{10}$$

$$\frac{\partial A_3}{\partial z} = 0 \tag{11}$$

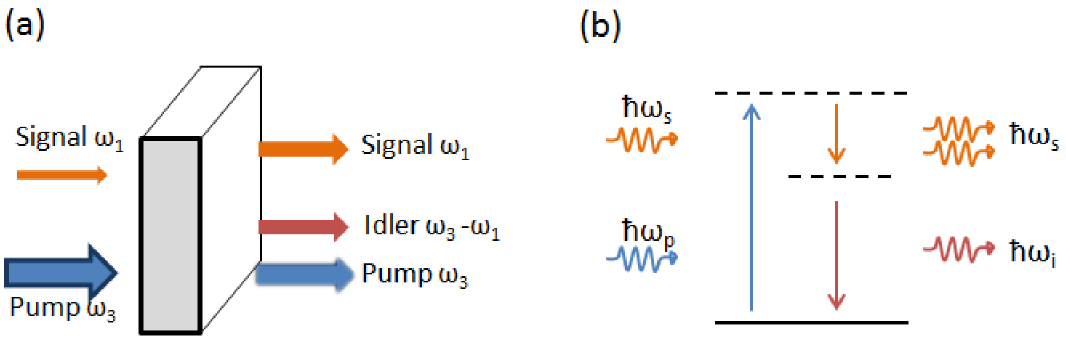

Figure 3: (a) Sketch of difference frequency mixing (b) and corresponding energy level diagram involved in optical parametric amplification

The intensity of signal and idler beam can be calculated using I = $n\epsilon_0 c_0 A^2$.

$$I_s(L) = I_{s0} * (1 + (\frac{\tau}{g} sinh gL)^2) \tag{12}$$

$$I_i(L) = \frac{2\omega_2 d_{eff}^2}{n_1 n_2 n_3 \epsilon_0 c_0^3} I_{s0} I_3 (\frac{sinh(gL)}{g})^2 \tag{13}$$

where L=length of the crystal,

$$g = (\tau^2 - \Delta k^2/4)^{1/2}$$
$$\tau^2 = \frac{2d_{eff}^2 \omega_1 \omega_2}{n_1 n_2 n_3 \epsilon_0 c_0^3} I_3$$

The parametric gain of the signal is

$$G(L) = \frac{I_s(L)}{I_{s0}} = 1 + [\frac{\tau}{g} sinh(gL)]^2 \tag{14}$$

Clearly, the parametric gain G(L) of the signal beam is directly proportional to the length of material L, the intensity of the pump beam but is inversely proportional to g. The value of 'g' is maximum for Δk = 0, the so called *phase-matching condition*. The physical meaning of the phase matching is that the phase velocity of the induced beam should be equal to the velocity of the inducing force so that the induced beam generated at different positions inside the crystal interfere constructively.

The condition for parametric amplification boils down to two conservation laws of energy and momemtum in the whole process.

$$\hbar\omega_3 = \hbar\omega_1 + \hbar\omega_2 \tag{15}$$

$$\hbar k_3 = \hbar k_1 + \hbar k_2 \tag{16}$$

Eq. 16 is referred to as phase matching condition in the following form. Since $\omega_3 n_3 = \omega_1 n_1 + \omega_2 n_2$ and using $\omega_3 = \omega_1 + \omega_2$, we get

$$\Rightarrow \omega_3(n_3 - n_2) = \omega_1(n_1 - n_2) \tag{17}$$

This equation cannot be satisfied by an isotropic crystal, where the refractive index is a monotonic function of frequency. In general, for the case of $\omega_3 > \omega_2 > \omega_1$, the positive dispersive isotropic material will have $n_3 > n_2 > n_1$, which implies that the right hand side of eq. 17 will be positive and the left hand side will be negative, never satisfying it. In order to satify eq.17, we would need a birefringent crystal where refractive index depends on the polarization direction of the beam. Typically in an optical parametric amplification, we use a negative uniaxial crystal, β-Barium Borate (BBO), where the refractive index along ordinary direction of crystal is higher than in the extraordinary direction *i.e.* $n_o > n_e$. If both signal and idler have the same polarization, then that is termed as *Type I* configuration. If signal and idler have different polarization, then that is referred as *Type II* configuration. Table 4 shows the possible phase matching configurations for a negative uniaxial crystal ($n_e > n_o$). Other combinations like ooo, eee etc. do not satisfy equation 17. *Type I* and *Type II* configurations have their own advantages. While *Type I* phase matching is used to obtain large amplification bandwidth of the signal at the cost of limited tunability of the broadband spectrum, *Type II* phase matching gives a hightly tunable narrow spectrum. In the next section, we explain how *Type I* phase matching favours broadband amplification.

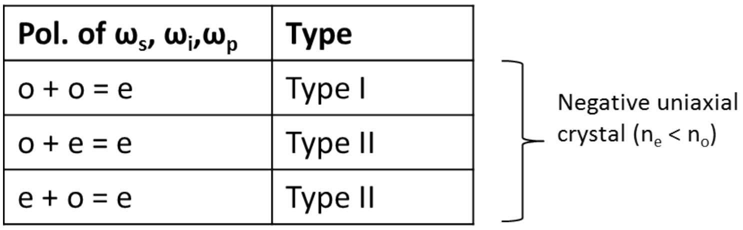

Pol. of ω_s, ω_i,ω_p	Type
o + o = e	Type I
o + e = e	Type II
e + o = e	Type II

Negative uniaxial crystal ($n_e < n_o$)

Figure 4: Table of various polarization mixing possible between signal, idler and pump in case of negative uniaxial crystal. o and e represents ordinary and extraordinary polarization direction respectively. n_o and n_e are their corresponding refractive indices.

A.1.3 Condition for broadband parametric amplification

In order to achieve broadband amplication, specific conditions need to be satisfied. If ω_s changes to ω_s + $\Delta\omega$ where $\Delta\omega$ is the amplification bandwidth, by energy conservation, the frequency of the idler changes from ω_i to ω_i - $\Delta\omega$. The phase mismatch for fixed pump frequency (ω_p) boils down to

$$\Delta k = k(\omega_p) - [k(\omega_s) + \Delta k_s] - [k(\omega_i) + \Delta k_i] = -\Delta k_i - \Delta k_s \tag{18}$$

To the first order of approximation, the above equation can be written as

$$\Delta k = \frac{\partial k_s}{\partial \omega_s}\Delta\omega = \frac{1}{v_{gi}} - \frac{1}{v_{gs}}\Delta\omega = \delta_{si}\Delta\omega \tag{19}$$

where v_{gs} and v_{gi} are group velocity of the signal and idler respectively.

The full width half maximum of the parametric gain can be derived under the approximation of large gain and negligible pump depletion and is written as

$$\boxed{\Delta\nu = \frac{2(ln2)^{1/2}}{pi}(\frac{\tau}{L})^{1/2}\frac{1}{\delta_{si}}} \tag{20}$$

Where δ_{si} = $1/v_{gi}$ - $1/v_{gs}$ is the group velocity mismatch (GVM) between the signal and the idler.

Clearly, in order to attain gain over broad spectrum of signal, one has to achieve δ_{si} = 0, which means v_{gs} = v_{gi}. There can be two ways to achieve this condition.

(1) To have degenerate signal and idler pulses (ω_s = ω_i), with *type I* phase matching. This is used for our broadband near-infrared setup (See section 6.2)

(2) Away from degeneracy, the above condition can be attained by accessing non-linear configuration. As shown in figure 5, in case of different frequencies of signal and idler, the collinear configuration will lead to spatially separated beams in contrast to the non-linear geometry where they overlap for more time and effectively have similar velocities in direction Ω.

A.2 Self-phase modulation and white light generation

This section brings forward the consequences of third order process described by $\chi^{(3)}$ of eq. 2. Self-phase modulation (SPM) is one of them and is widely exploited in white

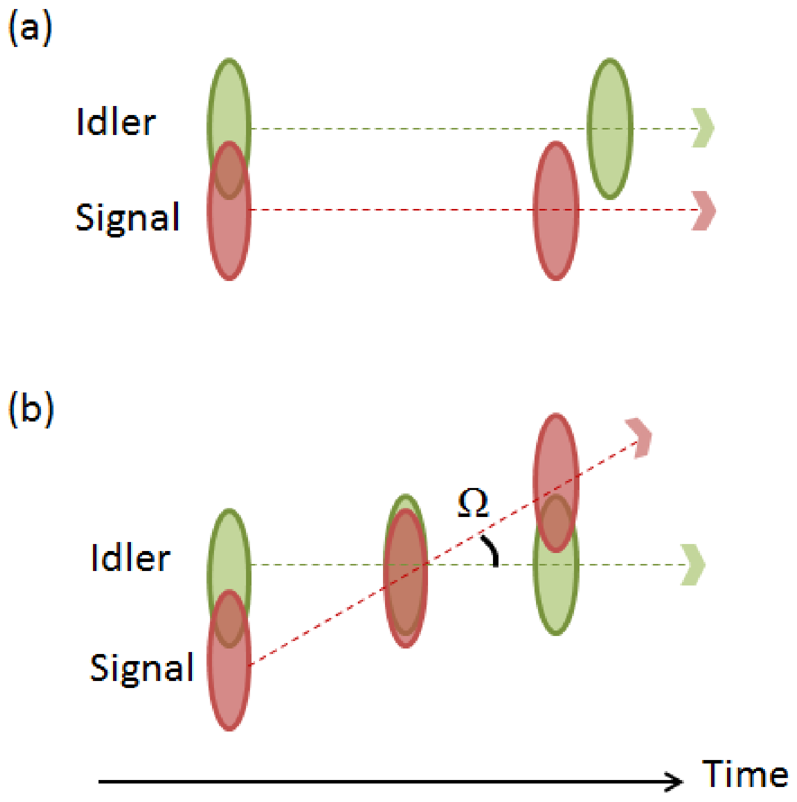

Figure 5: GVM between signal and idler in case of (a) Collinear (b) Non-collinear configuration

light generation. SPM is based on the Kerr-effect, which facilitates the change in refractive index of the medium as a function of intensity of light. The time dependent change in refractive index for a centrosymmetric material can be written as [174, 175]:

$$n(t) = n_0 + n_2 I(r,t) \tag{21}$$

where n_0 is linear refractive index of the medium, n_2 is second order nonlinear refractive index and I(r,t) is the intensity of light pulse.

The electric field of the incoming light is E = $E_0\ e^{i\phi}$. And the phase of the pulse, which is function of the refractive index can be written as follow.

$$\phi = w_0 t - kz = w_0 t - n(t)\frac{w_0}{c}z \tag{22}$$

This implies, any change in *n(t)* will result in change of phase, hence the effect is termed as self-phase modulation.

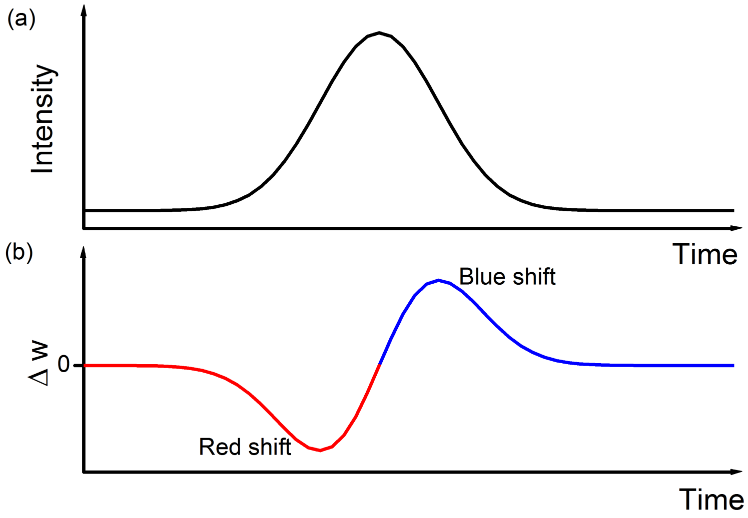

Figure 6: (a)Time dependent intensity profile of incoming light field (b) Corresponding change in frequency of the beam over time.

Clearly, the instantaneous frequency given by

$$w(t) = \frac{\delta \phi}{\delta t} = w_0 - n_2 \frac{w_0}{c} z \frac{dI}{dt} \tag{23}$$

implies that pulsed laser light can lead to creation of time dependent frequencies as shown in figure 6. In accordance with equation 23, for the rising edge of the intensity profile $dI/dt > 0$, hence red shift of the frequency occurs. Similarly, for the falling edge, $dI/dt < 0$, inducing blue shift. This technique is in general adopted to acheive large spectral broadening. Depending on the second order non-linear refractive index of the material and the time profile of the light, the broadening can cover a huge spectral range and be very strong. The concept of SPM is exploited in the generation of while light continuum as discussed in the following and also in some photonic crystal fibres, as in hollow core fibres (discussed in section 4.3).

White light supercontinuum Based on the concept of SPM, the while light continuum serves as a good candidate for the seed pulse in an OPA. With the standard pulsed laser at 800 nm and 30 fs pulse length, the non-linear medium sapphire can generate colors starting from visible (~400 nm) down to near infra-red (~1600 nm) region [176]. Though self-phase modulation is the main element towards the generation of white light supercontinuum [177], its mechanism is not fully understood till date [178]. Large spectral broadening obtained via strong SPM has been possible because of availabilty of short laser pulses.The intensity of the laser beam must exceed a certain threshold power, peculiar of the active medium.The pulse duration of all generated frequency components is not very different from the pulse duration of the input beam [179]. The white light has white center with few rings around it. These rings are due to self diffraction of the beam caused by the modulation of the wave front [180]. The wave front distortion is the consequence of spatial SPM of the beam, since the beam would have some transverse intensity profile.

A.3 Pump-probe spectroscopy

Equilibrium optical spectroscopy is a primary tool to measure emergent phenomena in condensed matter. Optical reflectivity measurements for opaque systems (or transmission measurements for transparent systems) over broad energy scales (1 meV to 10 eV) allow to measure the optical constants of the materials. The real and imaginary part of the dielectric function ($\epsilon\ (\omega) = \epsilon_1\ (\omega) + \epsilon_2\ (\omega)$) are related to the imaginary and real part of the optical conductivity respectively as $\sigma_1(\omega) = (\omega/4\pi)\ \epsilon_2\ (\omega)$ and $\sigma_2(\omega)$ = -($\omega/4\pi$) [$\epsilon_1(\omega)$ - 1]. The whole complex optical response can be extracted from R(ω) via Kramers-Kronig transformations provided that the measured spectral range is broad enough.

Pump-probe spectroscopy provides indeed the unique opportunity for time resolved studies of electronic and lattice dynamics at their fundamental time scales. As discussed in chapter 1, the concept of equilibrium optical spectroscopy can be extended out-of-equilibrium bringing microscopic insight into the emergent phases and even creating transient hidden phases, thermally inaccessible. In a pump-probe experiment, a laser pulse hits the sample first and induce a transient dynamics which is probed by a weak second pulse, suitably delayed with respect to the pump pulse. Importantly, the probe spot size should be smaller than the pump so as to probe a homogeneously excited region. The probe can be monitored in reflection ΔR/R or transmission ΔT/T geometry and measures the changes in the sample induced by the pump.

$$\frac{\Delta R}{R}(t) = \frac{\partial log(R)}{\partial \epsilon_1}\Delta\epsilon_1(t) + \frac{\partial log(R)}{\partial \epsilon_2}\Delta\epsilon_2(t) \tag{24}$$

$\Delta\epsilon_1$ and $\Delta\epsilon_1$ are the pump induced changes in the real and imaginary parts of dielectric function. Knowledge of the static value of $\epsilon_{1,2}$ serves as a good starting point to unravel the dynamics described by $\Delta\epsilon_{1,2}$ [181]. Depending on the pump and probe wavelength and the parameters, they are perturbing and probing, $\Delta\epsilon_{1,2}$ brings information on the changes in electronic, magnetic, orbital and lattice degree of freedom.

In degenerate pump-probe experiments, the probe pulse is a weak replica of the pump pulse. Pump and probe beams are extracted from a single beam coming from a laser source by either using a beam splitter or by spatially cutting the single beam into two using a D-shaped mirror. The latter method is used for the degenerate pump-probe experiment described in chapter 4. Such measuremens are key to understand a certain degree of freedom which is being perturbed and/or after the perturbation. The relaxation dynamics of photo-excited quasi-particles is one such example. In case of non-degenerate pump-probe experiments, the pump and the probe originates from different setups as reported in chapter 6. Such measurements can be used for example to understand the influence of the excited state on the electronic bands in near-infrared or phonon in the mid-infrared or the signatures of d.c. conductivity in the THz region.

B: Alternate pathway to modulation of Mott gap in a 1D half-filled Mott insulator

It is worthy to mention that the discussed 1/2 filled Mott gap can be altered in two different ways:
(1) Altering U/t.
(2) Altering the band filling away from half-filling condition.

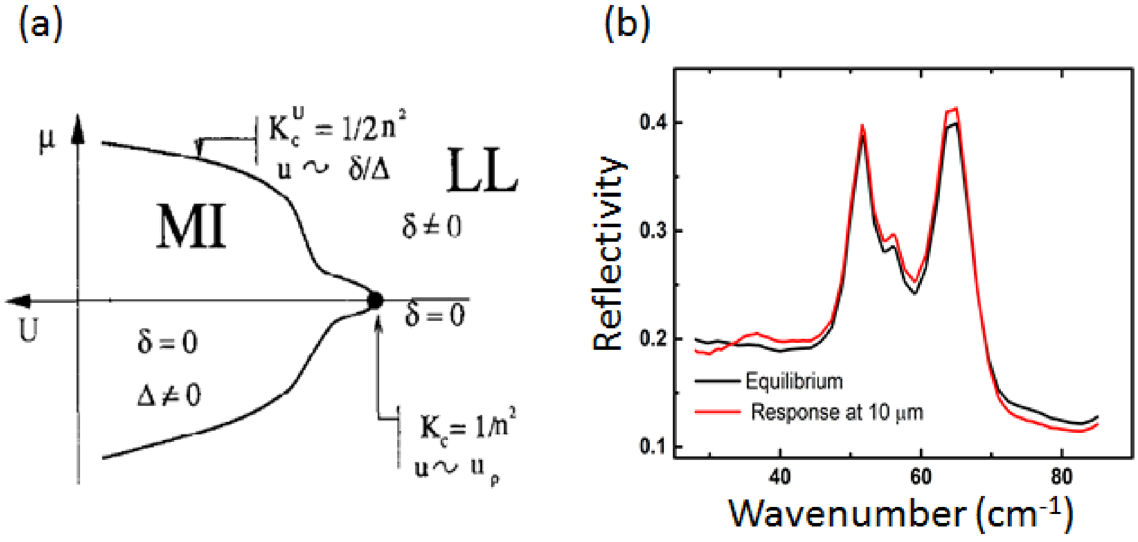

Figure 7: (a) Phase diagram in the vicinity of commensurate filling (n). U is on-site interaction energy, μ is chemical potential, MI is Mott insulator, LL is Lutinger liquid, δ is deviation from commensurate filling n and n=1 for half filling [Adapted from [182]] (b) Low frequency spectrum at room temperature of ET-F_2TCNQ in equilibrium (black) and under vibrational modulation at 10 μm laser pulses (red) [Adapted from [18]].

We can evidently discard the second scenario as follows. At equilibrium, any deviation from the commensurate filling either by chemical doping or by photodoping, results in metallic state [183–185]. Also, from the theory on 1D systems, any deviation

(δ) from half-filling will bring the system into the metallic state (as shown in figure 7 (a)) [182]. And experimental evidence shows no change in the Drude and hence the metallicity in the vibrationally driven system (see figure 7 (b)), thereby, confirming the first scenario to be the reason for observed CT dynamics.

C: Perturbed free induction decay

Perturbed free induction decay (PFID) are oscillations in both the time and frequency observed at negative pump-probe delays. PFID signals can be easily observed in ultrafast infrared spectroscopy experiments. Below follows a simple explanation for this phenomenon.

Let us consider a scenario where there is only a probe pulse impinging on the sample. The probe pulse may create coherent polarization in the material with some intrinsic decay time or dephasing time T_2. As shown in figure 8(a), the probe pulse induces a polarization which may cause emission of light E_p(t) known as free induction decay (FID).

Now, if the probe pulse is followed by a pump pulse, *i.e.* for negative time delay τ, the pump pulse will modify the FID signal to $E_{p,\tau}$(t) as shown in figure 8(b). The detector for the probe will capture the changes in FID due to the pump pulse. This is termed as PFID. Obviously, FID will be modified the most for small τ. Hence, the PFID signal diminishes with increasing negative time delays [111].

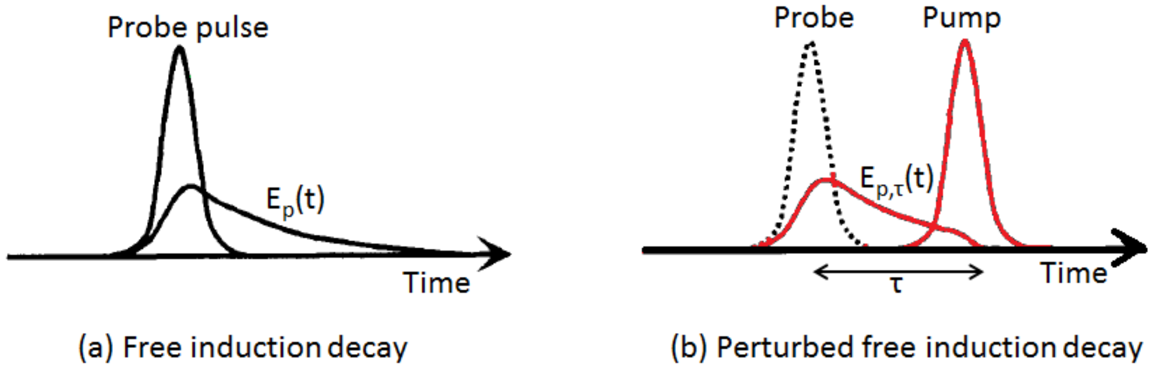

Figure 8: (a) The probe pulse and polarization induced field E_p(t) called free induction decay. (b) The pump pulse (in red) following probe pulse creating perturbed free induction decay (also in red). τ is the time delay between pump and probe and is negative in this case [Adapted from [111]].

Most importantly, the PFID signal vanishes for $\tau \geq 0$ (Causality principle). The reflectance of probe stays constant with time after the arrival of the pump pulse (see figure 9). This 'artifact' has been studied in detail theoretically and experimentally [113, 186]. When the probe light is resonant to some transition in the sample, the decay is exponential (see red line in figure 9) and underscores itself as oscillations as probe field goes away from resonance frequency (see orange line). Polack et al. and Nuernberger et al. have demonstrated ways to filter analytically such artifacts [187, 188]. But, this was beyond our purposes and needs for the thesis.

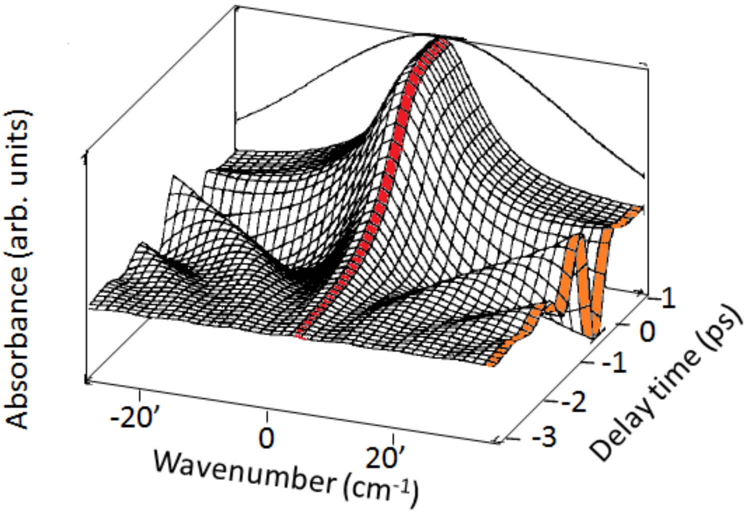

Figure 9: Absorbance as function of probe wavelength and pump-probe delay time. 0 on wavenumber axis represents the situation when probe is in resonance to certain transition of the sample and 20′ & -20′ represent the deviation in wavenumber from the resonance frequency [Adapted from [111]].

Bibliography

[1] N F Mott and R Peierls. Discussion of the paper by de boer and verwey. *Proceedings of the Physical Society*, 49(4S):72, 1937.

[2] Philip W Anderson. More is different. *Science*, 177(4047):393–396, 1972.

[3] Hidenori Takagi and Harold Y Hwang. An emergent change of phase for electronics. *Science*, 327(5973):1601–1602, 2010.

[4] Yoshinori Tokura. *Colossal magnetoresistive oxides*. CRC Press, 2000.

[5] Hitoshi Seo and Hidetoshi Fukuyama. Antiferromagnetic phases of one-dimensional quarter-filled organic conductors. *Journal of the Physical Society of Japan*, 66(5):1249–1252, 1997.

[6] Keiichirō Nasu. *Photoinduced phase transitions*. World Scientific, 2004.

[7] J Zhang and RD Averitt. Dynamics and control in complex transition metal oxides. *Annual Review of Materials Research*, 44:19–43, 2014.

[8] K Miyano, T Tanaka, Y Tomioka, and Y Tokura. Photoinduced insulator-to-metal transition in a perovskite manganite. *Physical review letters*, 78(22):4257, 1997.

[9] G Yu, CH Lee, AJ Heeger, N Herron, and EM McCarron. Transient photoinduced conductivity in single crystals of $YBa_2Cu_3O_{6.3}$:“photodoping”to the metallic state. *Physical review letters*, 67(18):2581, 1991.

[10] Hirohiko Ichikawa, Shunsuke Nozawa, Tokushi Sato, Ayana Tomita, Kouhei Ichiyanagi, Matthieu Chollet, Laurent Guerin, Nicky Dean, Andrea Cavalleri, Shin-ichi Adachi, et al. Transient photoinduced ‘hidden’phase in a manganite. *Nature materials*, 10(2):101–105, 2011.

[11] P Huai and Keiichiro Nasu. Difference between photoinduced phase and thermally excited phase. *Journal of the Physical Society of Japan*, 71(4):1182–1188, 2002.

[12] Matteo Rini, Nicky Dean, Jiro Itatani, Yasuhide Tomioka, Yoshinori Tokura, Robert W Schoenlein, Andrea Cavalleri, et al. Control of the electronic phase of a manganite by mode-selective vibrational excitation. *Nature*, 449(7158):72–74, 2007.

[13] RI Tobey, D Prabhakaran, AT Boothroyd, and A Cavalleri. Ultrafast electronic phase transition in $La_{0.5}Sr_{1.5}MnO_4$ by coherent vibrational excitation:evidence for nonthermal melting of orbital order. *Physical review letters*, 101(19):197404, 2008.

[14] A. D. Caviglia, R. Scherwitzl, P. Popovich, W. Hu, H. Bromberger, R. Singla, M. Mitrano, M. C. Hoffmann, S. Kaiser, P. Zubko, S. Gariglio, J.-M. Triscone, M. Först, and A. Cavalleri. Ultrafast strain engineering in complex oxide heterostructures. *Phys. Rev. Lett.*, 108:136801, Mar 2012.

[15] R Mankowsky, A Subedi, M Först, SO Mariager, M Chollet, HT Lemke, JS Robinson, JM Glownia, MP Minitti, A Frano, et al. Nonlinear lattice dynamics as a basis for enhanced superconductivity in $YBa_2Cu_3O_{6.5}$. *Nature*, 516(7529):71–73, 2014.

[16] Kunihiko Yamaji and Gunzi Saitō. *Organic superconductors*, volume 88. Springer Verlag, 1998.

[17] D Jerome and HJ Schulz. Organic conductors and superconductors. *Advances in Physics*, 51(1):293–479, 2002.

[18] S Kaiser, SR Clark, D Nicoletti, G Cotugno, RI Tobey, N Dean, S Lupi, H Okamoto, T Hasegawa, D Jaksch, et al. Optical properties of a vibrationally modulated solid state mott insulator. *Scientific reports*, 4, 2014.

[19] M Mitrano, G Cotugno, SR Clark, R Singla, S Kaiser, Julia Stahler, R Beyer, M Dressel, L Baldassarre, D Nicoletti, et al. Pressure-dependent relaxation in the photoexcited mott insulator ET-F_2TCNQ: Influence of hopping and correlations on quasiparticle recombination rates. *Physical review letters*, 112(11):117801, 2014.

[20] R Singla, G Cotugno, S Kaiser, M Först, M Mitrano, HY Liu, A Cartella, C Manzoni, H Okamoto, T Hasegawa, et al. Correlation-gap oscillations in an organic Mott-insulator induced by phase locked excitation of local molecular vibrations. *arXiv preprint arXiv:1409.1088*, 2014.

[21] Y Moritomo, Y Tomioka, A Asamitsu, Y Tokura, and Y Matsui. Magnetic and electronic properties in hole-doped manganese oxides with layered structures: $La_{1-x}Sr_{1+x}MnO_4$. *Physical Review B*, 51(5):3297, 1995.

[22] Direct observation of charge and orbital ordering in $La_{0.5}Sr_{1.5}MnO_4$, author = Murakami, Y. and Kawada, H. and Kawata, H. and Tanaka, M. and Arima, T. and Moritomo, Y. and Tokura, Y., journal = Phys. Rev. Lett., volume = 80, issue = 9, pages = 1932–1935, numpages = 0, year = 1998, month = Mar, publisher = American Physical Society, http://link.aps.org/doi/10.1103/PhysRevLett.80.1932.

[23] Charles Kittel and Paul McEuen. *Introduction to solid state physics*, volume 8. Wiley New York, 1976.

[24] Philip W Anderson. Absence of diffusion in certain random lattices. *Physical review*, 109(5):1492, 1958.

[25] Neil W Ashcroft and D Mermin. Introduction to solid state physics. *Saunders, Philadelphia*, 1976.

[26] Joerg Heber. Nobel prize 2014: Akasaki, amano & nakamura. *Nature Physics*, 10 (11):791–791, 2014.

[27] William Lawrence Bragg. The diffraction of short electromagnetic waves by a crystal. In *Proceedings of the Cambridge Philosophical Society*, volume 17, page 4, 1913.

[28] Max von Laue. Nobelprize. 1914.

[29] Philip B. Allen. Theory of thermal relaxation of electrons in metals. *Phys. Rev. Lett.*, 59:1460–1463, Sep 1987. doi: 10.1103/PhysRevLett.59.1460.

[30] SI Anisimov, BL Kapeliovich, and TL Perel'Man. Electron emission from metal surfaces exposed to ultrashort laser pulses. *Zh. Eksp. Teor. Fiz*, 66(776):375–7, 1974.

[31] M Borna and JR Oppenheimerb. On the quantum theory of molecules. 1954.

[32] Robert R Alfano. *Semiconductors probed by ultrafast laser spectroscopy*. Elsevier, 1985.

[33] Andreas Othonos. Probing ultrafast carrier and phonon dynamics in semiconductors. *Journal of applied physics*, 83(4):1789–1830, 1998.

[34] Peter Y Yu and Manuel Cardona. *Fundamentals of semiconductors*. Springer, 2005.

[35] Orazio Svelto and David C Hanna. Principles of lasers. 1998.

[36] Ronald Ulbricht, Euan Hendry, Jie Shan, Tony F Heinz, and Mischa Bonn. Carrier dynamics in semiconductors studied with time-resolved terahertz spectroscopy. *Reviews of Modern Physics*, 83(2):543, 2011.

[37] Eugene Wigner. On the interaction of electrons in metals. *Physical Review*, 46(11): 1002, 1934.

[38] J H de Boer and E J W Verwey. Semi-conductors with partially and with completely filled 3 d -lattice bands. *Proceedings of the Physical Society*, 49(4S):59, 1937.

[39] N F Mott. The basis of the electron theory of metals, with special reference to the transition metals. *Proceedings of the Physical Society. Section A*, 62(7):416, 1949.

[40] E. Saitoh, Y. Tomioka, T. Kimura, and Y. Tokura. Role of orbital correlation in colossal magnetoresistance. *Journal of Magnetism and Magnetic Materials*, 239(1–3): 170 – 172, 2002. ISSN 0304-8853.

[41] S. Jin, T. H. Tiefel, M. McCormack, R. A. Fastnacht, R. Ramesh, and L. H. Chen. Thousandfold change in resistivity in magnetoresistive la-ca-mn-o films. *Science*, 264(5157):413–415, 1994.

[42] SSP Parkin. Giant magnetoresistance in magnetic nanostructures. *Annual Review of Materials Science*, 25(1):357–388, 1995.

[43] Masatoshi Imada, Atsushi Fujimori, and Yoshinori Tokura. Metal-insulator transitions. *Rev. Mod. Phys.*, 70:1039–1263, Oct 1998.

[44] A. Zylbersztejn and N. F. Mott. Metal-insulator transition in vanadium dioxide. *Phys. Rev. B*, 11:4383–4395, Jun 1975.

[45] Dimitri N Basov, Richard D Averitt, Dirk Van Der Marel, Martin Dressel, and Kristjan Haule. Electrodynamics of correlated electron materials. *Reviews of Modern Physics*, 83(2):471, 2011.

[46] AV Boris, Y Matiks, E Benckiser, A Frano, P Popovich, V Hinkov, P Wochner, M Castro-Colin, E Detemple, Vivek Kumar Malik, et al. Dimensionality control of electronic phase transitions in nickel-oxide superlattices. *Science*, 332(6032): 937–940, 2011.

[47] J. Hubbard. Electron correlations in narrow energy bands. *Proceedings of the Royal Society of London A: Mathematical, Physical and Engineering Sciences*, 276(1365):238–257, 1963.

[48] Gabriel Kotliar and Dieter Vollhardt. Strongly correlated materials: Insights from dynamical mean-field theory. *Physics Today*, 57(3):53–60, 2004.

[49] Martin Dressel. *Electrodynamics of solids: optical properties of electrons in matter*. Cambridge University Press, 2002.

[50] S-K Mo, JD Denlinger, H-D Kim, J-H Park, JW Allen, A Sekiyama, A Yamasaki, K Kadono, S Suga, Y Saitoh, et al. Prominent quasiparticle peak in the photoemission spectrum of the metallic phase of V_2O_3. *Physical review letters*, 90(18): 186403, 2003.

[51] J Zaanen, GA Sawatzky, and JW Allen. Band gaps and electronic structure of transition-metal compounds. *Physical Review Letters*, 55(4):418, 1985.

[52] Ross H. McKenzie, J. Merino, J. B. Marston, and O. P. Sushkov. Charge ordering and antiferromagnetic exchange in layered molecular crystals of the theta type. *Phys. Rev. B*, 64:085109, Aug 2001.

[53] S Wall, D Brida, SR Clark, HP Ehrke, D Jaksch, A Ardavan, S Bonora, H Uemura, Y Takahashi, T Hasegawa, et al. Quantum interference between charge excitation paths in a solid-state Mott insulator. *Nature Physics*, 7(2):114–118, 2011.

[54] Hiroki Gomi, Akira Takahashi, Toshihiro Ueda, Hisashi Itoh, and Masaki Aihara. Photogenerated holon-doublon cluster states in strongly correlated low-dimensional electron systems. *Phys. Rev. B*, 71:045129, Jan 2005.

[55] Karl A Gschneidner, LeRoy Eyring, and Gerry H Lander. *Handbook on the physics and chemistry of rare earths*, volume 32. Elsevier, 2002.

[56] John Clarke Slater, John Clarke Slater, John Clarke Slater, Chemist Physicist, and John Clarke Slater. *Quantum theory of atomic structure*, volume 1. McGraw-Hill New York, 1960.

[57] JE Hirsch. Dynamic hubbard model. *Physical review letters*, 87(20):206402, 2001.

[58] J. E. Hirsch. Charge expulsion, charge inhomogeneity, and phase separation in dynamic hubbard models. *Phys. Rev. B*, 87:184506, May 2013.

[59] GH Bach and F Marsiglio. Electron-hole asymmetry in the dynamic hubbard model. *Journal of superconductivity and novel magnetism*, 24(5):1571–1575, 2011.

[60] Studies of polaron motion: Part i. the molecular-crystal model. *Annals of Physics*, 8(3):325 – 342, 1959.

[61] JE Hirsch. Superconductivity from undressing. *Physical Review B*, 62(21):14487, 2000.

[62] Elbio Dagotto. Complexity in strongly correlated electronic systems. *Science*, 309 (5732):257–262, 2005.

[63] Giacomo Coslovich, Bernhard Huber, W-S Lee, Y-D Chuang, Y Zhu, T Sasagawa, Z Hussain, HA Bechtel, MC Martin, Z-X Shen, et al. Ultrafast charge localization in a stripe-phase nickelate. *Nature communications*, 4, 2013.

[64] Yong Q An, Antoinette J Taylor, Steven D Conradson, Stuart A Trugman, Tomasz Durakiewicz, and George Rodriguez. Ultrafast hopping dynamics of 5 f electrons in the Mott insulator UO_2 studied by femtosecond pump-probe spectroscopy. *Physical review letters*, 106(20):207402, 2011.

[65] Y Iwasa, K Mizuhashi, T Koda, Y Tokura, and G Saito. Metal-insulator transition and antiferromagnetic order in bis (ethylenedithio) tetrathiafulvalene tetracyanoquinodimethane (BEDT-TTF)(TCNQ). *Physical Review B*, 49(5):3580, 1994.

[66] T. Ogasawara, T. Kimura, T. Ishikawa, M. Kuwata-Gonokami, and Y. Tokura. Dynamics of photoinduced melting of charge/orbital order in a layered manganite $La_{0.5}Sr_{1.5}MnO_4$. *Phys. Rev. B*, 63:113105, Mar 2001.

[67] Yoshinori Tokura. Photoinduced phase transition: A tool for generating a hidden state of matter. *Journal of the Physical Society of Japan*, 75(1), 2006.

[68] M Matsubara, Y Okimoto, T Ogasawara, Y Tomioka, H Okamoto, and Y Tokura. Ultrafast photoinduced insulator-ferromagnet transition in the perovskite manganite $Gd_{0.55}Sr_{0.45}MnO_3$. *Physical review letters*, 99(20):207401, 2007.

[69] Yoichi Okimoto, Hiroyuki Matsuzaki, Yasuhide Tomioka, Istvan Kezsmarki, Takeshi Ogasawara, Masakazu Matsubara, Hiroshi Okamoto, and Yoshinori Tokura. Ultrafast photoinduced formation of metallic state in a perovskite-type manganite with short range charge and orbital order. *Journal of the Physical Society of Japan*, 76(4), 2007.

[70] M Först, RI Tobey, S Wall, H Bromberger, V Khanna, AL Cavalieri, Y-D Chuang, WS Lee, R Moore, WF Schlotter, et al. Driving magnetic order in a manganite by ultrafast lattice excitation. *Physical Review B*, 84(24):241104, 2011.

[71] M Först, R Mankowsky, H Bromberger, DM Fritz, H Lemke, D Zhu, M Chollet, Y Tomioka, Y Tokura, R Merlin, et al. Displacive lattice excitation through

nonlinear phononics viewed by femtosecond x-ray diffraction. *Solid State Communications*, 169:24–27, 2013.

[72] Alaska Subedi, Andrea Cavalleri, and Antoine Georges. Theory of nonlinear phononics for coherent light control of solids. *Physical Review B*, 89(22):220301, 2014.

[73] Stefan Kaiser, CR Hunt, D Nicoletti, W Hu, I Gierz, HY Liu, M Le Tacon, T Loew, D Haug, B Keimer, et al. Optically induced coherent transport far above t c in underdoped $YBa_2Cu_3O_{6+\delta}$. *Physical Review B*, 89(18):184516, 2014.

[74] D Fausti, RI Tobey, N Dean, S Kaiser, A Dienst, MC Hoffmann, S Pyon, T Takayama, H Takagi, and A Cavalleri. Light-induced superconductivity in a stripe-ordered cuprate. *science*, 331(6014):189–191, 2011.

[75] W Hu, S Kaiser, D Nicoletti, CR Hunt, I Gierz, MC Hoffmann, M Le Tacon, T Loew, B Keimer, and A Cavalleri. Optically enhanced coherent transport in $YBa_2Cu_3O_{6.5}$ by ultrafast redistribution of interlayer coupling. *Nature materials*, 13(7):705–711, 2014.

[76] Luuk JP Ament, Michel van Veenendaal, Thomas P Devereaux, John P Hill, and Jeroen van den Brink. Resonant inelastic X-ray scattering studies of elementary excitations. *Reviews of Modern Physics*, 83(2):705, 2011.

[77] A. Cavalleri, Cs. Tóth, C. W. Siders, J. A. Squier, F. Ráksi, P. Forget, and J. C. Kieffer. Femtosecond structural dynamics in VO_2 during an ultrafast solid-solid phase transition. *Phys. Rev. Lett.*, 87:237401, Nov 2001.

[78] Michael F Becker, A Bruce Buckman, Rodger M Walser, Thierry Lépine, Patrick Georges, and Alain Brun. Femtosecond laser excitation of the semiconductor-metal phase transition in VO_2. *Applied Physics Letters*, 65(12):1507–1509, 1994.

[79] A. Cavalleri, Th. Dekorsy, H. H. W. Chong, J. C. Kieffer, and R. W. Schoenlein. Evidence for a structurally-driven insulator-to-metal transition in VO_2: A view from the ultrafast timescale. *Phys. Rev. B*, 70:161102, Oct 2004.

[80] JC Petersen, S Kaiser, N Dean, A Simoncig, HY Liu, AL Cavalieri, C Cacho, ICE Turcu, E Springate, F Frassetto, et al. Clocking the melting transition of charge and lattice order in 1T-TaS_2 with ultrafast extreme-ultraviolet angle-resolved photoemission spectroscopy. *Physical review letters*, 107(17):177402, 2011.

[81] M Först, RI Tobey, H Bromberger, SB Wilkins, V Khanna, AD Caviglia, Y-D Chuang, WS Lee, WF Schlotter, JJ Turner, et al. Melting of charge stripes in vibrationally driven $La_{1.875}Ba_{0.125}CuO_4$: Assessing the respective roles of electronic and lattice order in frustrated superconductors. *Physical review letters*, 112 (15):157002, 2014.

[82] Ferromagnetic compounds of manganese with perovskite structure. *Physica*, 16 (3):337 – 349, 1950.

[83] P Schiffer, AP Ramirez, W Bao, and SW Cheong. Low temperature magnetoresistance and the magnetic phase diagram of $La_{1-x}Ca_xMnO_3$. *Physical Review Letters*, 75(18):3336, 1995.

[84] T Okuda, T Kimura, H Kuwahara, Y Tomioka, A Asamitsu, Y Okimoto, E Saitoh, and Y Tokura. Roles of orbital in magnetoelectronic properties of colossal magnetoresistive manganites. *Materials Science and Engineering: B*, 63(1):163–170, 1999.

[85] Y Moritomo, A Asamitsu, H Kuwahara, and Y Tokura. Giant magnetoresistance of manganese oxides with a layered perovskite structure. 1996.

[86] Clarence Zener. Interaction between the *d*-shells in the transition metals. ii. ferromagnetic compounds of manganese with perovskite structure. *Phys. Rev.*, 82: 403–405, May 1951.

[87] John B. Goodenough. Theory of the role of covalence in the perovskite-type manganites [La,M(II)]MnO_3. *Phys. Rev.*, 100:564–573, Oct 1955.

[88] SS Dhesi, A Mirone, C De Nadai, P Ohresser, P Bencok, NB Brookes, P Reutler, A Revcolevschi, A Tagliaferri, O Toulemonde, et al. Unraveling orbital ordering in $La_{0.5}Sr_{1.5}MnO_4$. *Physical review letters*, 92(5):056403, 2004.

[89] K Nakamura, T Arima, A Nakazawa, Y Wakabayashi, and Y Murakami. Polarization-dependent resonant-x-ray diffraction in charge-and orbital-ordering phase of $Nd_{1/2}Sr_{1/2}MnO_3$. *Physical Review B*, 60(4):2425, 1999.

[90] M v Zimmermann, JP Hill, Doon Gibbs, M Blume, D Casa, B Keimer, Y Murakami, Y Tomioka, and Y Tokura. Interplay of charge, orbital and magnetic order in $Pr_{1-x}Ca_xMnO_3$. In *MRS Proceedings*, volume 590, page 103. Cambridge Univ Press, 1999.

[91] Y Tokura and N Nagaosa. Orbital physics in transition-metal oxides. *science*, 288 (5465):462–468, 2000.

[92] BJ Sternlieb, JP Hill, UC Wildgruber, GM Luke, B Nachumi, Y Moritomo, and Y Tokura. Charge and magnetic order in $La_{0.5}Sr_{1.5}MnO_4$. *Physical review letters*, 76(12):2169, 1996.

[93] Wei Bao, CH Chen, SA Carter, and SW Cheong. Electronic phase separation and charge ordering in $(Sr,La)_2MnO_4$: Indication of triplet bipolarons. *Solid state communications*, 98(1):55–59, 1996.

[94] Javier Herrero-Martín, Joaquín García, Gloria Subías, Javier Blasco, and Maria Concepción Sánchez. Structural origin of dipole x-ray resonant scattering in the low-temperature phase of $Nd_{0.5}Sr_{0.5}MnO_3$. *Physical Review B*, 70(2): 024408, 2004.

[95] V Ferrari, M Towler, and PB Littlewood. Oxygen stripes in $La_{0.5}Ca_{0.5}MnO_3$ from ab initio calculations. *Physical review letters*, 91(22):227202, 2003.

[96] Y. Murakami, J. P. Hill, D. Gibbs, M. Blume, I. Koyama, M. Tanaka, H. Kawata, T. Arima, Y. Tokura, K. Hirota, and Y. Endoh. Resonant X-ray scattering from orbital ordering in $LaMnO_3$. *Phys. Rev. Lett.*, 81:582–585, Jul 1998.

[97] Kliment Il'ich Kugel' and Khomskiĭ. The jahn-teller effect and magnetism: transition metal compounds.

[98] DI Khomskii and KI Kugel. Elastic interactions and superstructures in manganites and other Jahn-Teller systems. *Physical Review B*, 67(13):134401, 2003.

[99] U Staub, V Scagnoli, AM Mulders, M Janousch, Z Honda, and JM Tonnerre. Charge/orbital ordering vs. jahn-teller distortion in $La_{0.5}Sr_{1.5}MnO_4$. *EPL (Europhysics Letters)*, 76(5):926, 2006.

[100] SB Wilkins, PD Spencer, PD Hatton, SP Collins, MD Roper, D Prabhakaran, and AT Boothroyd. Direct observation of orbital ordering in $La_{0.5}Sr_{1.5}MnO_4$ using soft x-ray diffraction. *Physical review letters*, 91(16):167205, 2003.

[101] T. Ishikawa, K. Ookura, and Y. Tokura. Optical response to orbital and charge ordering in a layered manganite: $La_{1/2}Sr_{3/2}MnO_4$. *Phys. Rev. B*, 59:8367–8370, Apr 1999.

[102] Y Okimoto, Y Tomioka, Y Onose, Y Otsuka, and Y Tokura. Optical study of $Pr_{1-x}Ca_xMnO_3$ (x= 0.4) in a magnetic field: Variation of electronic structure with charge ordering and disordering phase transitions. *Physical Review B*, 59(11): 7401, 1999.

[103] H. Ehrke, R. I. Tobey, S. Wall, S. A. Cavill, M. Först, V. Khanna, Th. Garl, N. Stojanovic, D. Prabhakaran, A. T. Boothroyd, M. Gensch, A. Mirone, P. Reutler, A. Revcolevschi, S. S. Dhesi, and A. Cavalleri. Photoinduced melting of antiferromagnetic order in $La_{0.5}Sr_{1.5}MnO_4$ measured using ultrafast resonant soft x-ray diffraction. *Phys. Rev. Lett.*, 106:217401, May 2011.

[104] Jagdeep Shah. *Ultrafast spectroscopy of semiconductors and semiconductor nanostructures*, volume 115. Springer Science & Business Media, 1999.

[105] Adrian L Cavalieri, Eleftherios Goulielmakis, Balint Horvath, Wolfram Helml, Martin Schultze, Markus Fieß, Volodymyr Pervak, Laszlo Veisz, VS Yakovlev, Matthias Uiberacker, et al. Intense 1.5-cycle near infrared laser waveforms and their use for the generation of ultra-broadband soft-X-ray harmonic continua. *New Journal of Physics*, 9(7):242, 2007.

[106] Z Cheng, A Fürbach, S Sartania, Matthias Lenzner, Ch Spielmann, and Ferenc Krausz. Amplitude and chirp characterization of high-power laser pulses in the 5-fs regime. *Optics letters*, 24(4):247–249, 1999.

[107] Mauro Nisoli, S De Silvestri, O Svelto, R Szipöcs, K Ferencz, Ch Spielmann, S Sartania, and Ferenc Krausz. Compression of high-energy laser pulses below 5 fs. *Optics letters*, 22(8):522–524, 1997.

[108] Markus Fieß. *Advancing attosecond metrology*. PhD thesis, lmu, 2010.

[109] Martin Schultze. *Attosecond real time observation of ionization and electron-electron interactions*. PhD thesis, lmu, 2008.

[110] Ming Li, John P Nibarger, Chunlei Guo, and George N Gibson. Dispersion-free transient-grating frequency-resolved optical gating. *Applied optics*, 38(24):5250–5253, 1999.

[111] P Hamm. Coherent effects in femtosecond infrared spectroscopy. *Chemical physics*, 200(3):415–429, 1995.

[112] CH Brito Cruz, JP Gordon, PC Becker, RL Fork, and Charles V Shank. Dynamics of spectral hole burning. *Quantum Electronics, IEEE Journal of*, 24(2):261–269, 1988.

[113] Perturbed free induction decay in ultrafast mid-IR pump–probe spectroscopy. *Chemical Physics Letters*, 517(1–3):36 – 40, 2011. ISSN 0009-2614.

[114] K Yamamoto, T Kimura, T Ishikawa, T Katsufuji, and Y Tokura. Raman spectroscopy of the charge-orbital ordering in layered manganites. *Physical Review B*, 61(21):14706, 2000.

[115] P Beaud, A Caviezel, SO Mariager, L Rettig, G Ingold, C Dornes, SW Huang, JA Johnson, M Radovic, T Huber, et al. A time-dependent order parameter for ultrafast photoinduced phase transitions. *Nature materials*, 2014.

[116] A. Pashkin, C. Kübler, H. Ehrke, R. Lopez, A. Halabica, R. F. Haglund, R. Huber, and A. Leitenstorfer. Ultrafast insulator-metal phase transition in VO_2 studied by multiterahertz spectroscopy. *Phys. Rev. B*, 83:195120, May 2011.

[117] Lisa Dhar, John A. Rogers, and Keith A. Nelson. Time-resolved vibrational spectroscopy in the impulsive limit. *Chemical Reviews*, 94(1):157–193, 1994.

[118] H. J. Zeiger, J. Vidal, T. K. Cheng, E. P. Ippen, G. Dresselhaus, and M. S. Dresselhaus. Theory for displacive excitation of coherent phonons. *Phys. Rev. B*, 45: 768–778, Jan 1992.

[119] F D M Haldane. 'luttinger liquid theory' of one-dimensional quantum fluids. i. properties of the luttinger model and their extension to the general 1d interacting spinless fermi gas. *Journal of Physics C: Solid State Physics*, 14(19):2585, 1981.

[120] J Voit. One-dimensional fermi liquids. *Reports on Progress in Physics*, 58(9):977, 1995.

[121] T Giamarchi. Theoretical framework for quasi-one dimensional systems. *Chemical reviews*, 104(11):5037–5056, 2004.

[122] Elliott H Lieb and FY Wu. Absence of mott transition in an exact solution of the short-range, one-band model in one dimension. *Physical Review Letters*, 20(25): 1445, 1968.

[123] R Claessen, M Sing, U Schwingenschlögl, P Blaha, M Dressel, and Claus Schelde Jacobsen. Spectroscopic signatures of spin-charge separation in the quasi-one-dimensional organic conductor TTF-TCNQ. *Physical review letters*, 88(9):096402, 2002.

[124] BJ Kim, H Koh, E Rotenberg, S-J Oh, H Eisaki, N Motoyama, S Uchida, T Tohyama, S Maekawa, Z-X Shen, et al. Distinct spinon and holon dispersions in photoemission spectral functions from one-dimensional $SrCuO_2$. *Nature Physics*, 2(6):397–401, 2006.

[125] H Kishida, H Matsuzaki, H Okamoto, T Manabe, M Yamashita, Y Taguchi, and Y Tokura. Gigantic optical nonlinearity in one-dimensional Mott-Hubbard insulators. *Nature*, 405(6789):929–932, 2000.

[126] Martin Dressel. Ordering phenomena in quasi-one-dimensional organic conductors. *Naturwissenschaften*, 94(7):527–541, 2007.

[127] D Jérome. The physics of organic superconductors. *Science*, 252(5012):1509–1514, 1991.

[128] T. Hasegawa, T. Mochida, R. Kondo, S. Kagoshima, Y. Iwasa, T. Akutagawa, T. Nakamura, and G. Saito. Mixed-stack organic charge-transfer complexes with intercolumnar networks. *Phys. Rev. B*, 62:10059–10066, Oct 2000.

[129] P Guionneau, CJ Kepert, G Bravic, D Chasseau, MR Truter, M Kurmoo, and P Day. Determining the charge distribution in BEDT-TTF salts. *Synthetic metals*, 86(1):1973–1974, 1997.

[130] T Hasegawa, S Kagoshima, T Mochida, S Sugiura, and Y Iwasa. Electronic states and anti-ferromagnetic order in mixed-stack charge-transfer compound (BEDT-TTF)(F_2TCNQ). *Solid state communications*, 103(8):489–493, 1997.

[131] Rudolf Ernst Peierls. *More surprises in theoretical physics*, volume 19. Princeton University Press, 1991.

[132] ME Kozlov, KI Pokhodnia, and AA Yurchenko. The assignment of fundamental vibrations of BEDT-TTF and BEDT-TTF-d8. *Spectrochimica Acta Part A: Molecular Spectroscopy*, 43(3):323–329, 1987.

[133] John David Jackson and Ronald F Fox. Classical electrodynamics. *American Journal of Physics*, 67(9):841–842, 1999.

[134] F Gebhard, K Born, M Scheidler, P Thomas, and SW Koch. Optical absorption of strongly correlated half-filled mott-hubbard chains. *Philosophical Magazine B*, 75 (1):47–65, 1997.

[135] FHL Essler, F Gebhard, and E Jeckelmann. Excitons in one-dimensional mott insulators. *Physical Review B*, 64(12):125119, 2001.

[136] Eric Jeckelmann. Ground-state phase diagram of a half-filled one-dimensional extended Hubbard model. *Physical review letters*, 89(23):236401, 2002.

[137] E Jeckelmann, F Gebhard, and FHL Essler. Optical conductivity of the half-filled Hubbard chain. *Physical review letters*, 85(18):3910, 2000.

[138] Eric Jeckelmann. Optical excitations in a one-dimensional mott insulator. *Physical Review B*, 67(7):075106, 2003.

[139] S. Iwai, M. Ono, A. Maeda, H. Matsuzaki, H. Kishida, H. Okamoto, and Y. Tokura. Ultrafast optical switching to a metallic state by photoinduced Mott transition in a halogen-bridged nickel-chain compound. *Phys. Rev. Lett.*, 91: 057401, Jul 2003.

[140] Shinichiro Iwai and Hiroshi Okamoto. Ultrafast phase control in one-dimensional correlated electron systems. *Journal of the Physical Society of Japan*, 75(1):011007, 2006.

[141] Akira Takahashi, Hisashi Itoh, and Masaki Aihara. Photoinduced insulator-metal transition in one-dimensional Mott insulators. *Physical Review B*, 77(20): 205105, 2008.

[142] H Okamoto, K Ikegami, T Wakabayashi, Y Ishige, J Togo, H Kishida, and H Matsuzaki. Ultrafast photoinduced melting of a spin-peierls phase in an organic charge-transfer compound, K-tetracyanoquinodimethane. *Physical review letters*, 96(3):037405, 2006.

[143] H Okamoto, H Matsuzaki, T Wakabayashi, Y Takahashi, and T Hasegawa. Photoinduced metallic state mediated by spin-charge separation in a one-dimensional organic mott insulator. *Physical review letters*, 98(3):037401, 2007.

[144] C. Kim, A. Y. Matsuura, Z.-X. Shen, N. Motoyama, H. Eisaki, S. Uchida, T. Tohyama, and S. Maekawa. Observation of spin-charge separation in one-dimensional $SrCuO_2$. *Phys. Rev. Lett.*, 77:4054–4057, Nov 1996.

[145] Henk Eskes and Andrzej M Oleś. Two hubbard bands: Weight transfer in optical and one-particle spectra. *Physical review letters*, 73(9):1279, 1994.

[146] Markus Greiner, Olaf Mandel, Tilman Esslinger, Theodor W Hänsch, and Immanuel Bloch. Quantum phase transition from a superfluid to a mott insulator in a gas of ultracold atoms. *nature*, 415(6867):39–44, 2002.

[147] BJ Powell and Ross H McKenzie. Strong electronic correlations in superconducting organic charge transfer salts. *Journal of Physics: Condensed Matter*, 18(45):R827, 2006.

[148] J Wosnitza. Quasi-two-dimensional organic superconductors. *Journal of Low Temperature Physics*, 146(5-6):641–667, 2007.

[149] Thomas Uehlinger, Gregor Jotzu, Michael Messer, Daniel Greif, Walter Hofstetter, Ulf Bissbort, and Tilman Esslinger. Artificial graphene with tunable interactions. *Physical review letters*, 111(18):185307, 2013.

[150] S Inouye, MR Andrews, J Stenger, H-J Miesner, DM Stamper-Kurn, and W Ketterle. Observation of feshbach resonances in a bose–einstein condensate. *Nature*, 392(6672):151–154, 1998.

[151] Immanuel Bloch, Jean Dalibard, and Wilhelm Zwerger. Many-body physics with ultracold gases. *Reviews of Modern Physics*, 80(3):885, 2008.

[152] Jens Philipp Ronzheimer. *Non-equilibrium dynamics of ultracold atoms in optical lattices*. PhD thesis, lmu, 2014.

[153] Niels Strohmaier, Daniel Greif, Robert Jördens, Leticia Tarruell, Henning Moritz, Tilman Esslinger, Rajdeep Sensarma, David Pekker, Ehud Altman, and Eugene Demler. Observation of elastic doublon decay in the fermi-hubbard model. *Physical review letters*, 104(8):080401, 2010.

[154] Leslie E Ballentine. *Quantum mechanics*, volume 280. Prentice Hall Englewood Cliffs, 1990.

[155] RD McDonald, AK Klehe, J Singleton, and W Hayes. The pressure dependence of many-body interactions in the organic superconductor κ-(BEDT-TTF)$_2$Cu(SCN)$_2$(BEDT-TTF$\equiv$ bis (ethylene-dithio) tetrathiafulvalene): a comparison of high-pressure infrared reflectivity and raman scattering experiments. *Journal of Physics: Condensed Matter*, 15(30):5315, 2003.

[156] HK Mao, J-A Xu, and PM Bell. Calibration of the ruby pressure gauge to 800 kbar under quasi-hydrostatic conditions. *Journal of Geophysical Research: Solid Earth (1978–2012)*, 91(B5):4673–4676, 1986.

[157] Dara PS McCutcheon and Ahsan Nazir. Coherent and incoherent dynamics in excitonic energy transfer: Correlated fluctuations and off-resonance effects. *Physical Review B*, 83(16):165101, 2011.

[158] Anthony J Leggett, SDAFMGA Chakravarty, AT Dorsey, Matthew PA Fisher, Anupam Garg, and W Zwerger. Dynamics of the dissipative two-state system. *Reviews of Modern Physics*, 59(1):1, 1987.

[159] Takashi Yamamoto, Mikio Uruichi, Kaoru Yamamoto, Kyuya Yakushi, Atushi Kawamoto, and Hiromi Taniguchi. Examination of the charge-sensitive vibra-

tional modes in bis (ethylenedithio) tetrathiafulvalene. *The Journal of Physical Chemistry B*, 109(32):15226–15235, 2005.

[160] Alberto Girlando. Charge sensitive vibrations and electron-molecular vibration coupling in bis (ethylenedithio)-tetrathiafulvalene (BEDT-TTF). *The Journal of Physical Chemistry C*, 115(39):19371–19378, 2011.

[161] Erik Zeek, Kira Maginnis, Sterling Backus, Ulrich Russek, Margaret Murnane, Gérard Mourou, Henry Kapteyn, and Gleb Vdovin. Pulse compression by use of deformable mirrors. *Opt. Lett.*, 24(7):493–495, Apr 1999.

[162] T Binhammer, E Rittweger, U Morgner, R Ell, and FX Kärtner. Spectral phase control and temporal superresolution toward the single-cycle pulse. *Optics letters*, 31(10):1552–1554, 2006.

[163] Alexander Sell, Alfred Leitenstorfer, and Rupert Huber. Phase-locked generation and field-resolved detection of widely tunable terahertz pulses with amplitudes exceeding 100 mv/cm. *Optics letters*, 33(23):2767–2769, 2008.

[164] Cristian Manzoni, Michael Först, Henri Ehrke, and Andrea Cavalleri. Single-shot detection and direct control of carrier phase drift of midinfrared pulses. *Optics letters*, 35(5):757–759, 2010.

[165] M Uno, K Seto, M Masuda, W Ueda, and S Takahashi. A new route to phenylenedimalononitrile and the analogues using palladium-catalyzed carbon-carbon bond formation. *Tetrahedron letters*, 26(12):1553–1556, 1985.

[166] AB Kuzmenko. Kramers-kronig constrained variational analysis of optical spectra. *Review of scientific instruments*, 76(8):083108, 2005.

[167] GA Garrett, AG Rojo, AK Sood, JF Whitaker, and R Merlin. Vacuum squeezing of solids: Macroscopic quantum states driven by light pulses. *Science*, 275(5306): 1638–1640, 1997.

[168] SL Johnson, P Beaud, E Vorobeva, CJ Milne, ED Murray, S Fahy, and G Ingold. Directly observing squeezed phonon states with femtosecond x-ray diffraction. *Physical review letters*, 102(17):175503, 2009.

[169] F Gebhard, K Born, M Scheidler, P Thomas, and SW Koch. Exact results for the optical absorption of strongly correlated electrons in a half-filled peierls-distorted chain. *Philosophical Magazine B*, 75(1):13–46, 1997.

[170] Giovanni Cotugno. Tuning and vibrational modulation of strongly correlated organic salts. 2014.

[171] Andrea Cartella, Stefano Bonora, Michael Först, Giulio Cerullo, Andrea Cavalleri, and Cristian Manzoni. Pulse shaping in the mid-infrared by a deformable mirror. *Optics letters*, 39(6):1485–1488, 2014.

[172] Carlo Vicario, Clemens Ruchert, Fernando Ardana-Lamas, Peter M Derlet, B Tudu, Jan Luning, and Christoph P Hauri. Off-resonant magnetization dynamics phase-locked to an intense phase-stable terahertz transient. *Nature Photonics*, 7(9):720–723, 2013.

[173] D. E. Spence, P. N. Kean, and W. Sibbett. 60-fsec pulse generation from a self-mode-locked Ti:sapphire laser. *Opt. Lett.*, 16(1):42–44, Jan 1991.

[174] Robert W Boyd. *Nonlinear optics*. Academic press, 2003.

[175] Robert R Alfano et al. The supercontinuum laser source. 1989.

[176] Giulio Cerullo and Sandro De Silvestri. Ultrafast optical parametric amplifiers. *Review of scientific instruments*, 74(1):1–18, 2003.

[177] RL Fork, WJ Tomlinson, CV Shank, C Hirlimann, and R Yen. Femtosecond white-light continuum pulses. *Optics Letters*, 8(1):1–3, 1983.

[178] Alexander L Gaeta. Catastrophic collapse of ultrashort pulses. *Physical Review Letters*, 84(16):3582, 2000.

[179] Time resolved picosecond emission spectroscopy of organic dye lasers. *Chemical Physics Letters*, 9(1):1 – 5, 1971. ISSN 0009-2614. doi: http://dx.doi.org/10.1016/0009-2614(71)80165-3.

[180] SD Durbin, SM Arakelian, and YR Shen. Laser-induced diffraction rings from a nematic-liquid-crystal film. *Optics letters*, 6(9):411–413, 1981.

[181] Guglielmo Lanzani, Giulio Cerullo, and Sandro De Silvestri. *Coherent Vibrational Dynamics*. CRC Press, 2007.

[182] T Giamarchi. Mott transition in one dimension. *Physica B: Condensed Matter*, 230: 975–980, 1997.

[183] N Drichko, K Petukhov, M Dressel, O Bogdanova, E Zhilyaeva, R Lyubovskaya, A Greco, and J Merino. Indications of electronic correlations in the 1/ 5-filled

two-dimensional conductor β-(BEDO-TTF)$_5$[CsHg(SCN)$_4$]$_2$. *Physical Review B*, 72(2):024524, 2005.

[184] T Sasaki, N Yoneyama, Y Nakamura, N Kobayashi, Y Ikemoto, T Moriwaki, and H Kimura. Optical probe of carrier doping by x-ray irradiation in the organic dimer mott insulator κ-(BEDT-TTF)$_2$Cu[N(CN)$_2$] Cl. *Physical review letters*, 101 (20):206403, 2008.

[185] Matthieu Chollet, Laurent Guerin, Naoki Uchida, Souichi Fukaya, Hiroaki Shimoda, Tadahiko Ishikawa, Kazunari Matsuda, Takumi Hasegawa, Akira Ota, Hideki Yamochi, et al. Gigantic photoresponse in 1/4-filled-band organic salt (EDO-TTF)$_2$PF$_6$. *Science*, 307(5706):86–89, 2005.

[186] B. Fluegel, N. Peyghambarian, G. Olbright, M. Lindberg, S. W. Koch, M. Joffre, D. Hulin, A. Migus, and A. Antonetti. Femtosecond studies of coherent transients in semiconductors. *Phys. Rev. Lett.*, 59:2588–2591, Nov 1987.

[187] Thomas Polack. A filtering procedure for systematic removal of pump-perturbed polarization artifacts. *Optics express*, 14(12):5823–5828, 2006.

[188] Patrick Nuernberger, Kevin F Lee, Adeline Bonvalet, Thomas Polack, Marten H Vos, Antigoni Alexandrou, and Manuel Joffre. Suppression of perturbed free-induction decay and noise in experimental ultrafast pump-probe data. *Optics letters*, 34(20):3226–3228, 2009.

Acknowledgement

I would like to thank my supervisor, Prof. Dr. Andrea Cavalleri for providing me the opportunity to do Ph.D. degree in his lab. I got several chances to learn from him not just on research but about life as well. I leaned the great positive outlook towards research and that everything here is to be understood and not to be feared. I am fully indebted for all his patience, encouragement, enthusiam and pushing me farther than I thought I could go.

I thoroughly cherished my work in our laser lab 49b. I am grateful to Michael Foerst who introduced me to the field of optics. The great suggestions by him helped to solve numerous experimental problems. I greatly appreciate his willingness to help and the time he had put for correcting this thesis.

I have to thank Cristian Manzoni for many reasons. I had very short overlap of three months with Cristian in the lab and the optics lessons taught by him in that limited time helped me throughout my Ph.D years. He is a great teacher a student can have. I am also grateful to him for all his quick replies to my emails, full of questions. The ET project would not had been possible without his expertise.

A lot on my understanding on solid materials came from Stefan Kaiser. I am grateful to Stefan for his constant supply of knowledge, his clear understanding of the subject sand his willingness to teach. I am completely indebted for all your help and the time he put in for teaching. His vigrous thesis correction helped it to be in the present form and helped me to be a better writer and thinker.

Having Matteo Mitrano as my officemate allowed me to ask physics questions all around the day. I am very thankful to him who patiently answered to those curosities. Also, thanks for all the fun time spend in the lab during the pressure project and otherwise too. I would also like to thank Alberto Simoncig without whom the manganite experiment would not have been possible. Every morning, he would stand next to the laser trying to run that tricky machine like a soldier and finally we could successfully finish the project. I would also like to thank Ivanka Grguras for providing us with the characterization of ultrashort laser pulses which are also used in this thesis . I also thank my colleagues from Oxford University, Giovanni Cotugno, Stephan Clark and Dieter Jakschen for providing us the theoretical support that greatly assisted the ET research. I would also like to thank my other coworker, Andrea Cartella, Haiyun Liu

and Luca Piovani for all the help in the ET project. I am grateful to Joerg who provided all the beautiful figures for papers. Also, thanks to Michaela Petrick and Frederick for constant technical support in all my experiments. I would also like to thank Adrian Cavalieri who equipped me with his lab tricks during the short period we worked together in lab.

I would specialy like to thank Stefan Kaiser, Michael Foerst, Daniele Nicolleti, Stephan Clark and Matteo Mitrano for reading the thesis from a naive writer and making all the useful comments and suggestions which greatly improved the thesis.

I would like to thank all my colleagues for their smiling faces keeping the work place motivational, lively and pleasant.

Outside the lab, I have many people to thank. To start with, I would like to thank Vivek Sir who showed me the direction of research in the first place. Surely, I would not have been doing this Ph.D. without his encouragement and motivation. I am grateful to my friends from IIT Roorkee, Anita, Moumita, Sandeep, Soham, Somu, Subhash, Vishvas for their precious friendship and all those memorable moments since IIT days.

My stay in Hamburg would not have been complete without Moon and Uday. They both have been my family, friend, tuitor and almost everything. Hamburg has been beautiful with their presence. I would also like to thank Karthick and Raj for the great happy company during the trips around the europe. Also, thanks Karthick for making corrections to this thesis.

Lastly, I would like to thank my parents, my little brother Deepak and my grandparents. All my good deeds belong to them. This thesis would have been impossible without their unconditional love and support.